PETROGENESIS AND AGES OF THE AMPHIBOLITES WITHIN THE SÖĞÜT METAMORPHICS, CENTRAL SAKARYA TERRANE (NW ESKİŞEHİR, TURKEY)

A THESIS SUBMITTED TO
THE GRADUATE SCHOOL OF NATURAL AND APPLIED SCIENCES
OF
MIDDLE EAST TECHNICAL UNIVERSITY

BY

İSMAİL DOĞANCAN YAŞAR

IN PARTIAL FULFILLMENT OF THE REQUIREMENTS
FOR
THE DEGREE OF MASTER OF SCIENCE
IN
GEOLOGICAL ENGINEERING

JULY 2020

Approval of the thesis:

PETROGENESIS AND AGES OF THE AMPHIBOLITES WITHIN THE SÖĞÜT METAMORPHICS, CENTRAL SAKARYA TERRANE (NW ESKİŞEHİR, TURKEY)

submitted by **İSMAİL DOĞANCAN YAŞAR** in partial fulfillment of the requirements for the degree of **Master of Science in Geological Engineering Department, Middle East Technical University** by,

Prof. Dr. Halil Kalıpçılar
Dean, Graduate School of **Natural and Applied Sciences** _____

Prof. Dr. Erdin Bozkurt
Head of the Department, **Geological Engineering** _____

Assoc. Prof. Dr. Kaan Sayıt
Supervisor, **Geological Engineering, METU** _____

Examining Committee Members:

Prof. Dr. Nilgün Güleç
Geological Engineering, METU _____

Assoc. Prof. Dr. Kaan Sayıt
Geological Engineering, METU _____

Assoc. Prof. Dr. Ersin Koralay
Geological Engineering, Dokuz Eylül Uni. _____

Assoc. Prof. Dr. H. Evren Çubukçu
Geological Engineering, Hacettepe Uni. _____

Assoc. Prof. Dr. Biltan Kürkçüoğlu
Geological Engineering, Hacettepe Uni. _____

Date: 08.07.2020

I hereby declare that all information in this document has been obtained and presented in accordance with academic rules and ethical conduct. I also declare that, as required by these rules and conduct, I have fully cited and referenced all material and results that are not original to this work.

Name, Last name : İsmail Doğancan Yaşar

Signature :

ABSTRACT

PETROGENESIS AND AGES OF THE AMPHIBOLITES WITHIN THE SÖĞÜT METAMORPHICS, CENTRAL SAKARYA TERRANE (NW ESKİŞEHİR, TURKEY)

Yaşar, İsmail Doğancan
Master of Science, Geological Engineering
Supervisor: Assoc. Prof. Dr. Kaan Sayıt

July 2020, 138 pages

The Sakarya Composite Terrane (SCT) in northern Turkey consists of a pre-Jurassic basement composed of several tectonic units. The Söğüt Metamorphics, preserved within the Central Sakarya Terrane (a part of the SCT), is one of these tectonic units, consisting of para- and ortho-gneisses associated with bands, lenses, boudins, and tectonic slices of amphibolites.

Considering their field relations and petrographic features, amphibolites have fine- and coarse-grained varieties. The metamorphic conditions of amphibolites are defined by hornblende+plagioclase+biotite±sphene and epidote+chlorite+muscovite paragenesis for pro- and retro-grade phases, respectively. However, the peak metamorphic conditions (low-to-medium P/high T amphibolite facies) is defined by the sillimanite+biotite±cordierite paragenesis of the paragneisses.

Geochemically, the trace element systematics of the amphibolites reveals two different chemical types for their protoliths: Type 1 amphibolites have somewhat E-MORB characteristics, with negative Zr-Hf anomalies and variable enrichment in highly incompatible elements, whereas Type 2 amphibolites have subduction-modified signatures with negative Nb anomalies. A continental within-plate rift

setting with a metasomatized subcontinental lithospheric mantle (SCLM) source, and an intra-oceanic subduction zone setting with a mantle source metasomatized by slab-derived fluids/melts are proposed for the original crystallization setting of Type 1 and Type 2 amphibolites protoliths', respectively.

U-Pb zircon dating revealed Middle Ordovician, and Middle Carboniferous crystallization ages for the protoliths of Type 1 and 2 amphibolites, respectively. Altogether, the new data obtained confirms the opening of an oceanic basin due to within-plate rifting during the Middle Ordovician. The Middle Carboniferous magmatism, on the other hand, suggests the presence of an intra-oceanic subduction zone within this ocean.

Keywords: Central Sakarya Terrane, Söğüt Metamorphics, Amphibolite, Geochemistry, U-Pb Geochronology

ÖZ

SÖĞÜT METAMORFİKLERİ, ORTA SAKARYA BİRLİĞİ (KB ESKİŞEHİR, TÜRKİYE) İÇERİSİNDEKİ AMFİBOLİTLERİN PETROJENEZİ VE YAŞLARI

Yaşar, İsmail Doğancan
Yüksek Lisans, Jeoloji Mühendisliği
Tez Yöneticisi: Doç. Dr. Kaan Sayıt

Temmuz 2020, 138 sayfa

Türkiye'nin kuzeyinde yer alan Sakarya Kompozit Tektonik Birliği, Jura öncesi yaşlı, çeşitli temel birimlerinden oluşur. Bu temel birimlerinden biri olan Orta Sakarya Birliği içinde yer alan Söğüt Metamorfikleri, orto- ve para-gnayslar ile ilişkili, bantlar, uzamış mercekler ve tektonik dilimler halinde gözlemlenen amfibolitler içerir.

Arazi ilişkileri ve petrografik özellikleri göz önüne alındığında, amfibolitlerin ince ve kaba taneli çeşitleri olduğu gözlemlenmiştir. Amfibolitlerde ilerleyen ve gerileyen metamorfizma koşulları sırasıyla hornblend+plajiyoklaz+biyotit±sfen ve epidot+klorit+muskovit parajenezleri ile temsil edilir. Bununla birlikte, pik metamorfik koşullar (düşük ila orta P/yüksek T amfibolit fasiyesi) paragnaysların sillimanit+biyotit±kordierit parajenezi ile tanımlanır.

Jeokimyasal olarak, amfibolitlerin eser element sistematiği, protolitleri için iki farklı kimyasal gruba işaret eder: Tip 1 amfibolitler, genel olarak E-MORB özelliklerine sahiptir, negatif Zr-Hf anomalileri ve uyumsuz elementlerde değişken derecelerde zenginleşmeye sahiptir. Tip 2 amfibolitler, negatif Nb anomalileri ile tanımlanır. Tip

1 amfibolitlerin protolitleri metasomatize edilmiş bir alt kıtasal litosfer mantosu kaynağına sahiptir ve kıtasal plaka içi açılma ortamında oluşmuştur. Tip 2 amfibolitlerin protolitleri için ise okyanus içi bir dalma batma ortamında, dalan levhadan türetilmiş sıvılar/eriyikler tarafından metasomatize edilmiş bir manto kaynağından türemişlerdir.

Zirkon U-Pb yaşlandırma yöntemi, Tip 1 ve Tip 2 amfibolitlerin protolitleri için sırasıyla Orta Ordovisyen ve Orta Karbonifer kristalleşme yaşlarına işaret etmektedir. Bu çalışmayla sağlanan yeni veriler bölgede Orta Ordoviziyen'den başlayarak plaka içi açılma sonucunda bir okyanusun gelişmeye başladığını destekler. Saptanan Orta Karbonifer magmatizması ise bu okyanusun içinde bir okyanusal dalma batma zonunun gelişmiş olduğunu gösterir.

Anahtar Kelimeler: Orta Sakarya Birliği, Söğüt Metamorfikleri, Amfibolit, Jeokimya, U-Pb Jeokronolojisi

To my late beloved uncle Arkun Orhan Yaşar, for he is kind, loving and brilliant.

“The supreme guide in life is science.” - Mustafa Kemal Atatürk

ACKNOWLEDGMENTS

There is not enough synonym of gratitude that can express mine to Assoc. Prof. Dr. Kaan Sayıt and Prof. Dr. Cemal Göncüoğlu for their commitment to my education with their unconditional share of immense experience, knowledge and wisdom; expanding, inspiring and insuring both my academic endeavors and personal development.

It was truly a blessing to be able to work with Assoc. Prof. Dr. Ersin Koralay and have the opportunity to learn from Prof. Dr. Nilgün Güleç, for both have educated me potently and thoroughly.

I would like to express my endless gratitude to Dr. Mesut Soylu for his invaluable mentorship and support on so many levels throughout my METU years.

I want to thank Prof. Dr. Erdin Bozkurt, Assist. Prof. Dr. Fatma Köksal and Dr. Serhat Köksal for granting me access to various laboratories in METU, and Orhan Karaman for guiding me through thin-section preparation.

I want to extend my thanks to ESAN, ALS Global and Demir Export for their comprehensive sponsorship at various parts of this study, made possible with the support and care of Ali Can Akpınar, Tuna Kaskatı, Ali Atlı, İsmail Cihan, Sare Yaylalı, Burak Aktoy, Serdar Çalgın, Sercan Bozan, Hüseyin Galan and Mustafa Tavaslıoğlu.

I want to acknowledge my dear friends; Alican Aktağ, Görkem Atasoy, Timur Ersöz, Meryem Dilan İnce, Akın Çil, Erkan İstanbulluoğlu, Furkan Oğuz, Emre Barış Erdem, Ahmet Cilbir, Gizem Naz Görmez, Mert Kılıç, Alperen Durudoğan, Göktuğ Harmancı, Tarık Bilgiç, Tolga Açılmış, Alperen Yıldızalp, Emir Gökbayrak, Kıvanç Uluca, Umut Vicdan, Ali Eren Şevran, Melike Filiz and Deniz Yalçın, for their support in the field, laboratory and several occasions when it was challenging to keep going.

I want to share my praise to my dear parents and sisters, for their bestowment of undying love, thrust, support, and countless sacrifices that have made my education possible.

TABLE OF CONTENTS

ABSTRACT v

ÖZ vii

ACKNOWLEDGMENTS x

TABLE OF CONTENTS xii

LIST OF TABLES xv

LIST OF FIGURES xvi

LIST OF ABBREVIATIONS xxi

CHAPTERS

1 INTRODUCTION 1

1.1 Purpose and Scope 1

1.2 Previous Studies 3

1.2.1 Rheic-Tethyside Evolution within Turkish Terranes 3

1.2.2 Söğüt Metamorphics 6

1.3 Geographic Setting 9

1.4 Methods of Study 10

1.4.1 Fieldwork 10

1.4.2 Laboratory Work 10

1.4.2.1 Petrographic Analysis 10

1.4.2.2 Whole-Rock Geochemistry Analysis 12

1.4.2.3 U-Pb Geochronology Analysis 13

2 GEOLOGY 17

2.1 Regional Geology 17

2.2 Local Geology 19
2.2.1 Söğüt Metamorphics 24
2.2.1.1 Para- and Ortho-Gneisses 24
2.2.1.2 Amphibolites 25
2.2.2 Sarıcakaya Granitoid 28
2.2.3 Tozman Metaophiolite 29
3 PETROGRAHY 33
3.1 Söğüt Metamorphics 33
3.1.1 Para- and Ortho-Gneisses 33
3.1.2 Amphibolites 36
3.2 Sarıcakaya Granitoid 42
3.3 Tozman Metaophiolite 42
4 GEOCHRONOLOGY AND GEOCHEMISTRY 47
4.1 U-Pb Geochronology 47
4.2 Whole-Rock Geochemistry 53
4.2.1 Assessment of Post-Crystallization Events 53
4.2.2 Classification 57
4.2.3 Elemental Variations 59
4.2.3.1 Major Oxides 59
4.2.3.2 Trace Elements 59
4.2.4 Petrogenesis 64
4.2.4.1 Fractional Crystallization 64
4.2.4.2 Source Characteristics 66
4.2.4.3 Tectonic Discrimination 74

5 DISCUSSION 83
5.1 Field Characteristics of Amphibolites 83
5.2 Metamorphic Conditions 84
5.3 Petrogenesis 85
5.4 Tozman Metaophiolite 87
5.5 Formation and Metamorphism Age 88
5.6 Regional Geodynamic Implications 91
6 CONCLUSION 95
REFERENCES 99
APPENDICES
A. ZIRCON PLATES 114
B. U-Pb LA-MC-ICP-MS RESULTS OF AMPHIBOLITES 127
C. U-Pb LA-MC-ICP-MS RESULTS OF ZIRCON STANDARDS 135

LIST OF TABLES

TABLES

Table 1.1. Detection limits of ME-ICP06 (values are in wt. %) and ME-ICP81 (values are in ppm) analysis. 13
Table 4.1. Whole-rock geochemical analysis results of amphibolites within Söğüt Metamorphics, including the major oxides (wt. %), trace elements (ppm) and REEs (ppm). 54
Table 5.1. Geochronological data from the Söğüt Metamorphics (SM) and Bayırköy Formation (BF). 89

LIST OF FIGURES

FIGURES

Figure 1.1. Distribution of the main Alpine tectonic units of Turkey (from Göncüoğlu, 2019). 2
Figure 1.2 Location map of the study area, located within İnhisar, Mihalgazi, and Sarıcakaya provinces. 9
Figure 2.1. Distribution of the Sakarya Composite Terrane (SCT) in Turkey (Modified from Göncüoğlu, 2019). Inset border shows the study area. 18
Figure 2.2. Regional map and generalized tectonostratigraphic section of the Paleozoic and Mesozoic units of the region (Modified from the 1/500.000 geological map of Turkey, MTA, 2004; Duru et al., 2002; Gedik and Aksay, 2002; Göncüoğlu et al., 1996; Şentürk and Karaköse, 1979). Inset border shows the study area. 20
Figure 2.3. Contact relationships between the Central Sakarya Terrane units: (A) The contacts between SM, KF, and BV. SM is thrusted onto the tertiary rock assemblages. (B) The unconformity between the SM, and Jurassic BF and BL succession. SM: Söğüt Metamorphics; KF: Kızılçay Formation; BV: Bozaniç Volcanics; BF: Bayırköy Formation; BL: Bilecik Limestone. 22
Figure 2.4. Geological map and generalized tectonostratigraphic relationships between the Central Sakarya Terrane units (Modified from Göncüoğlu et al., 1996; Duru et al., 2002; Gedik and Aksay, 2002). Sample locations of the analyzed amphibolite samples are marked on the map. 23
Figure 2.5. Para- and ortho-gneisses within Söğüt Metamorphics: (A-B) Paragneiss, partially melted and deformed, (C) Paragneiss with well-developed E-W foliation with a quartz porphyroclast, (D) Paragneiss with cross-cutting oblique quartzo-feldspathic vein, (E) Orthogneiss showing augen texture with abundant feldspar porphyroclasts, (F) Orthogneiss without any augen texture. 26
Figure 2.6. Amphibolites within the Söğüt Metamorphics: (A) Coarse-grained amphibolite barely showing foliation with cross-cutting quartzo-feldspacthic veins, (B) Coarse-grained amphibolite with no foliation, (C) Fine-grained amphibolite

boudins in a paragneiss host, (D) Sigma-shaped, deformed amphibolite lens within a paragneiss host, (E) Partial melting fabric on coarse-grained amphibolite, (F) Quartz vein cross-cutting amphibolite with well-developed foliation..... 28
Figure 2.7. Lithologies and field relationships of the Sarıcakaya Granitoid: (A) The deformed nature of SG, the dioritic rocks are cross-cut by a later stage quartzo-feldspathic veins with thicknesses varying from cm to m lengths, (B) Close-up view of quartzo-feldspathic vein cross-cutting diorite, (C) Enclave within the diorite... 30
Figure 2.8. Lithologies and field relationships of the Tozman Metaophibolite: (A) Leucogabbro, (B) Leuco- and melano-gabbro transition, (C) The faulted contact between the leucogabbro of TM and the orthogneisses of SM; leucogabbro is structurally at a higher position, compared to orthogneisses, (D) Serpentinized peridotite. 32
Figure 3.1. Photomicrographs of paragneisses within the Söğüt Metamorphics showing some mineralogical and textural features: (A-XPL, B-PPL) sil-bt-crd of deformed paragneiss, foliation is defined by the orientation of bt and sil, (C-XPL, D-PPL) qtz-bt-ms-zrn of paragneiss; note the decay halo of zircon inside the biotite, (E-XPL, F-PPL) sil-qtz-bt-ms of paragneiss. 35
Figure 3.2. Photomicrographs of orthogneisses within the Söğüt Metamorphics showing some mineralogical and textural features: (A-XPL, B-PPL) qtz-pl-bt of orthogneiss, note the polysynthetic twinning of pl, (C-XPL, D-PPL) qtz-bt-ms of orthogneiss, foliation is defined by the orientation of bt and ms, (E-XPL, F-PPL) qtz-pl-bt-euhedral zrn of orthogneiss. 37
Figure 3.3. Photomicrographs of amphibolites within the Söğüt Metamorphics showing some mineralogical and textural features: (A-XPL, B-PPL; SM20) hbl-pl-spn-qtz-chl-ser of amphibolite, note the pl grain at the center displaying pericline twinning, (C-XPL, D-PPL; SM19) bt-hbl-pl-qtz of fine-grained amphibolite, (E-XPL, F-PPL; SM12) hbl-pl-spn-chl-ser-ep with cross cutting qtz-vein, micro faults can be observed cutting through the qtz-vein. 40
Figure 3.4. Photomicrographs of amphibolites within the Söğüt Metamorphics showing some mineralogical and textural features: (A-XPL, B-PPL; SM10) hbl-pl-

spn-chl of amphibolite with cross-cutting quartz vein, note the cross-cutting oxide vein at the lower part, as well as the oxidization at the cracks of the horblende grains, (C-XPL, D-PPL; SM6) ep and pl replaced partly by sericite, note the cross-cutting cal vein, (E-PPL; SM20) Euhedral hbl, showing the metamorphic growth with brown core and green rim, as well as pl-qtz, zrn is present at the crack of the hornlende grain, (F-PPL, SM5) hbl-pl-ep-chl with spn of coarse-grained amphibolite. 41
Figure 3.5. Photomicrographs of diorite of Sarıcakaya Granitoid showing some mineralogical and textural features: (A-XPL, B-PPL) hbl-bt-qtz-pl of diorite, simple twinning on hbl, polysynthetic twinning on pl, (C-XPL, D-PPL) qtz-pl-hbl-bt-ms of diorite, note the undulose extinction and kinking on the qtz grain in the center.....43
Figure 3.6. Photomicrographs of cumulate-gabbros of Tozman Metaophiolite showing some mineralogical and textural features: (A-XPL, B-PPL) altered pl, partially serpentinized ol, opx (cumulate phase), cpx (intercumulus phase), note the polysynthetic and simple twinning of pl, (C-XPL, D-PPL) Partially serpentinized ol (cumulate phase), cpx (intercumulus phase), (E-XPL, F-PPL) pl-cpx-opx-ol with cross-cutting ctl vein.....45
Figure 4.1. Selected zircon grains from analyzed samples. Each scale bar indicates 50 μm, whereas the spot marks of the analysis locations are 12 μm in diameter. Presented ages are $^{206}Pb/^{238}U$ ages of each spot.....49
Figure 4.2. $^{207}Pb/^{235}U$ vs. $^{206}Pb/^{238}U$ diagram and weighted mean ages of SM6 (Type 2) and SM12 (Type 1) samples. 50
Figure 4.3. $^{207}Pb/^{235}U$ vs. $^{206}Pb/^{238}U$ diagram and weighted mean ages of SM19 and SM20 (Both are Type 2) samples.....51
Figure 4.4. $^{207}Pb/^{235}U$ vs. $^{206}Pb/^{238}U$ diagram and weighted mean ages of SM21 and SM29 (Both are Type 1) samples.....52
Figure 4.5. Multi-element spider diagram schematics of amphibolites from Söğüt Metamorphics, normalized with respect to N-MORB, values from Sun and McDonough, 1989.....56
Figure 4.6. Distribution of selected trace elements against Nb, values are in ppm. 57

Figure 4.7. Nb/Y vs. Zr/Ti classification diagram (Winchester and Floyd, 1977 modified by Pearce, 1996) for the amphibolites of the Söğüt Metamorphics. 58
Figure 4.8. Distribution of major-oxides against MgO, values are in wt. %. 60
Figure 4.9. Distribution of selected trace elements against MgO. Trace element values are in ppm, MgO values are in wt. %. 62
Figure 4.10. Multi-element spider diagram schematics of amphibolites from Söğüt Metamorphics, normalized with respect to N-MORB and Chondrite values from Sun and McDonough, 1989. 63
Figure 4.11. Nb/Yb vs. TiO_2/Yb ratio diagram after Pearce (2008). 67
Figure 4.12. Comparison of selected element ratios of amphibolites within Söğüt Metamorphics and basalts from modern tectonic settings: (A) Nb/Yb vs. Th/Yb; (B) Nb/Yb vs. Th/Nb; (C) La/Nb vs. Th/Nb; (D) Nb_N vs. Th/Nb. Data sources: Mariana Back-Arc (Pearce et al., 2005); South-Sandwich Arc (Pearce et al., 1995); Aeolian Arc (Calanchi et al., 2002); Greater Antilles Arc (Jolly et al., 2007); Mid-Atlantic Ridge (Niu et al., 2001); Walvis Ridge (Salters and Salci-Kocher, 2010); East-African Rift (Furman et al., 2006); Rio-Grande Rift (Gibson et al., 1993); West Greenland (Larsen et al., 2003); East Greenland (Hanghøj et al., 2003); St. Helena (Kawabata et al., 2011); Samoa (Jackson et al., 2010). E-MORB, N-MORB, and OIB values are taken from Sun and McDonough (1989). Fields of Mariana Back-Arc, South-Sandwich Arc, Aeolian Arc, Greater Antilles Arc, East African Rift and Rio-Grande Rift for (A) and (B), and Mariana Back-arc, Greater Antilles Arc, East-African Rift and Rio Grande Rift for (C-D), and South-Sandwich Arc, Aeolian Arc (D) are taken from Sayit et al. (2015). Field of Mid-Atlantic Ridge for (A) is taken from Sayit et al. (2016). 71
Figure 4.13. Comparison of selected element ratios (Nb/Yb vs. Nd/Zr) of amphibolites within Söğüt Metamorphics and basalts from modern tectonic settings. Data sources are the same as in Figure 4.12. 72
Figure 4.14. Multi-element spider diagram schematics of amphibolites from Söğüt Metamorphics, normalized with respect to Primitive Mantle. Primitive Mantle values from Sun and McDonough, 1989. 73

Figure 4.15. Binary tectonic discrimination diagrams: (A) Ti/Y vs. Zr/Y diagram of Pearce and Gale (1977); (B) Ti/1000 vs. V diagram of Shervais (1982). OFB: Ocean Floor Basalts. 75
Figure 4.16. Terniary tectonic discrimination diagrams: (A) 2*Nb-Zr/4-Y diagram of Meschede (1986); (B) Ti/100-Zr-3*Y diagram of Pearce and Cann (1973); (C-D) Hf/3-Th-Nb/16 and Zr/117-Th-Nb/16 diagrams of Wood (1980). WPA: Within-Plate Alkali; WPT: Within-Plate Tholeiites; WPB: Within-Plate Basalts; VAB: Volcanic Arc Basalts; CAB: Continental Arc Basalts; IAT: Island Arc Tholeiites; MORB: Mid Oceanic Ridge Basalt; P-MORB: Primitive-MORB; N-MORB: Normal-MORB; E-MORB: Enriched-MORB; OIB: Ocean Island Basalts. 76
Figure 4.17. Comparison of selected samples from various MORB-OIB related tectonic settings with amphibolites from Söğüt Metamorphics with respect to multi-element spider diagrams: (A) Mid-Atlantic Ridge (Sample ID: OT18-04); (B) Walvis Ridge (Sample ID: 74-528-46R-1, 78-86); (C) St. Helena (Sample ID: SH-15); (D) Samoa (Sample ID: ALIA-DR118-23). Normalized with respect to N-MORB, values from Sun and McDonough (1989). Data sources are same with Figure 4.12. 79
Figure 4.18. Comparison of selected samples from various continental within-plate tectonic settings with amphibolites from Söğüt Metamorphics with respect to multi-element spider diagrams: (A) Rio-Grande Rift (Sample ID: 89LT192); (B) East-African Rift (Sample ID: KL 18); (C) East Greenland (Sample ID: 417377); (D) West Greenland (Sample ID: 326787). Normalized with respect to N-MORB, values from Sun and McDonough (1989). Data sources are same with Figure 4.12. 80
Figure 4.19. Comparison of selected samples from various arc and arc related tectonic settings with amphibolites from Söğüt Metamorphics with respect to multi-element spider diagrams: (A) Mariana Back-Arc (Sample ID: D7-1-1); (B) South-Sandwich Arc (Sample ID: SST 7(1)); (C) Aeolian Arc (Sample ID: PN255); (D) Greater Antilles Arc (Sample ID: RBL135/51). Normalized with respect to N-MORB, values from Sun and McDonough (1989). Data sources are same with Figure 4.12. 81

LIST OF ABBREVIATIONS

ABBREVIATIONS

hbl: Hornblende

pl: Plagioclase

ep: Epidote

chl: Chlorite

ser: Sericite

bt: Biotite

spn: Sphene

qtz: Quartz

sil: Sillimanite

crd: Cordierite

ms: Muscovite

zrn: Zircon

grt: Garnet

ap: Apatite

ol: Olivine

opx: Orthopyroxene

cpx: Clinopyroxene

ctl: Chrysotile

CHAPTER 1

INTRODUCTION

1.1 Purpose and Scope

Turkey, as a part of the Eastern Mediterranean region, reflects the traces of the Tethyside orogeny, including multiple cycles of subduction/accretion processes, which ultimately led to the amalgamation of several micro-plates/terranes of diverse origins. The respective positions and geological relationships of these terranes were finalized with the Alpine orogeny. Göncüoğlu (1997) introduced the classifications of these terranes, with respect to their differential basement properties and affinities as (from north to south); the Istranca Terrane; a terrane of suspected Laurasian affinity, the İstanbul-Zonguldak Composite Terrane, the Intra-Pontide Ophiolite Belt, representing the remnants of a Neotethyan ocean domain, the Sakarya Composite Terrane (SCT), the İzmir-Ankara-Erzincan Ophiolite Belt, allochthonous remnants of oceanic assemblages and subduction/accretion complexes of the İzmir-Ankara-Erzincan ocean, the Tauride-Anatolide Composite Terrane, and the SE Anatolian Ophiolite Belt, preserving the relics of the southern branch of Neotethys (Figure 1.1).

The study of accreted terranes stands as a key point for the understanding of the evolution of the paleo-oceans, tectonic plate motions, and the respective position of a given terrane with respect to paleo-oceans throughout the geological time. Specifically, the remnants of the Tethyan oceans widely outcrops within these terranes. Yet, the understanding of the evolution of the pre-Tethyan oceans and configuration of associated terranes are scarcely documented due to the overprint of Variscan, Cimmerian and Alpine orogenies that took place as a result of the closure

of Rheic, Paleo- and Neo-tethys oceans respectively. Recently, especially by application of detailed geochemical and geochronological methods, it has been made possible to decipher the very complex geological evolution of the oceanic and/or continental plates in the NW Anatolian realm.

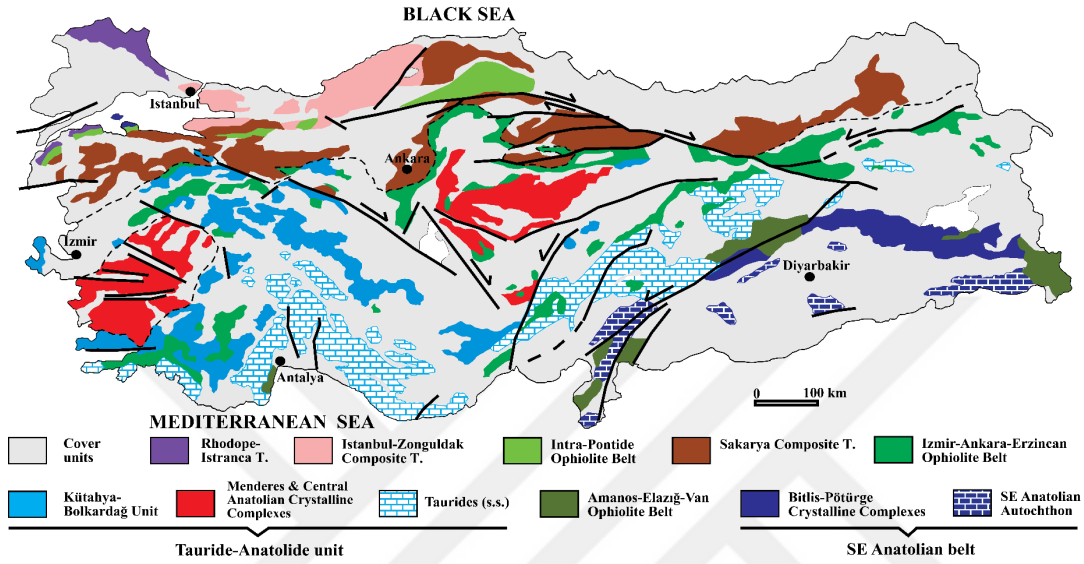


Figure 1.1. Distribution of the main Alpine tectonic units of Turkey (from Göncüoğlu, 2019).

The Söğüt Metamorphics is a pre-Variscan basement rock assemblage of the Central Sakarya Terrane within the Sakarya Composite Terrane (Göncüoğlu et al., 2000). The origin and evolution of the Söğüt Metamorphics are highly debated (Göncüoğlu et al., 2000; Topuz et al., 2020), and the area remains as an unsolved piece of the geology of Turkey. Previously, very limited research has been conducted on the metamorphic basement, which is limited by sample scarcity with respect to field distribution and application of analytical methods. The resultant works, however similar, provided information that failed to encompass the complete understanding of the whole geochemical and geochronological frame. To overcome this shortcoming, a few recent studies were performed on the petrology and age of the para- and ortho-gneisses that host a number of pre-Jurassic magmatic intrusions in the Central Sakarya Terrane (Ustaömer et al., 2012; Uğurcan et al., 2019; Mueller et

al., 2019; Topuz et al., 2020). However, these attempts are still quite incomplete for evaluating the geological features, geochemical characteristics, and ages of the different geological units and understanding the tectonic evolution of the Söğüt Metamorphics.

This study is focused on the determination of the tectono-magmatic evolution of the basic igneous rocks, now observed as amphibolites, within the Söğüt Metamorphics by field geology, petrography, whole-rock geochemistry, and U-Pb geochronology. It is aimed to produce a more complete geodynamic model of the region, in which the petrogenetic characteristics and tectonomagmatic setting of the protoliths of the amphibolites and their tectonic evolution within the geological time will be integrated. This study aims to provide understanding mainly in three aspects;

i) What is the tectonic setting(s) in which the protoliths of the amphibolites within the Söğüt Metamorphics were formed?

ii) What is the crystallization age(s) of the protoliths of the amphibolites within the Söğüt Metamorphics?

iii) Does the Söğüt Metamorphics represent a piece of continental lithosphere intruded by the Carboniferous arc magmatism, or an accretionary prism that involves products of an oceanic arc/back-arc magmatism?

1.2 Previous Studies

The previous studies will be introduced in two sub-sections, encompassing the i) Rheic-Tethyside evolution within Turkish Terranes, and ii) Söğüt Metamorphics.

1.2.1 Rheic-Tethyside Evolution within Turkish Terranes

Consecutive opening and closure of Rheic, Paleo- and Neo-tethys oceans resulted in the amalgamation of the terranes within Turkey. Originally the Rheic Ocean is defined as the separating seaway between the peri-Gondwanan (Gondwana-derived)

terranes such as Iberia, Avalonia, and Cadomia and the main body of Gondwana during Middle Paleozoic for the western Mediterranean realm. For the eastern Mediterranean area Göncüoğlu (1997), Göncüoğlu and Kozur (1999), Göncüoğlu and Kozlu (2000), and Gürsu and Göncüoğlu (2005) suggested a similar position of the Rheic Ocean between the peri-Gondwanan Moesia-Istanbul-Zonguldak terranes in the north and the precursor of the Sakarya Composite Terrane in the south. It is generally accepted that the Rheic Ocean opened in the Early Ordovician following the closure of the still northerly located Iapetus Ocean (Nance and Linnemann, 2008) and partially closed during the Permian-Carboniferous assembly of Pangea (Murphy et al., 2006). Furthermore, it has been alternatively suggested that the southward subduction of the Rheic Ocean under the peri-Gondwanan blocks caused the magmatism, and back-arc spreading which resulted in the opening of Paleo-tethys Ocean during the Middle Ordovician to Silurian (Stampfli, 2000; Stampfli et al., 2002). On the other hand, recently, Topuz et al. (2020) have suggested a Silurian anorogenic rift-related magmatism to be the cause of separation of Armonica from the northern margin of Gondwana. They abandoned the name Rheic Ocean for this branch but used the name "Paleo-Tethys" instead. In the conventional models, it was interpreted that during the Ordovian to Carboniferous, the northern terranes of Anatolia should have migrated towards Laurasia during the closure of the Rheic Ocean (Göncüoğlu, 2010). According to the alternative model (Stampfli Group; Topuz et al., 2020), following the closure of Rheic with the accretion of Armonica (including the northern terranes of Anatolia) to Laurassia, the Paleo-tethys, located to the south, started to subduct northward, creating an active margin to the south of Laurassia. Finally, the closure of the Paleo-tethys led to the Carboniferous Variscan orogeny.

The Paleotethyan Ocean sensu Şengör and Yılmaz (1981) and Göncüoğlu (1997), however, was located in a completely different position then the Paleo-tethys of Stampfli Group (i.e. to the north of the SCT) and has not closed prior to the Latest Triassic to Liassic. Instead, it produced the Late Paleozoic-Triassic Karakaya Complex that was attached to the Variscan Central Sakarya Terrane during its

closure resulting in the Cimmerian Orogeny (Okay and Göncüoğlu, 2004; Sayit and Göncüoğlu, 2013).

Overall, SCT consists of remnants of both pre-Variscan and Cimmerian continental and oceanic assemblages. The pre-Variscan terranes are also observed as tectonic inlayers in several north Anatolian metamorphic massifs, namely, Kazdağ, Uludağ, Söğüt, Devrekani, Pulur, and Harsdere massifs (Göncüoğlu, 2010). The pre-Variscan basement of the SCT and its Permian cover is interpreted to be separated (rifted) from the Gondwanan Tauride-Anatolide block due to the southward subduction of the Paleozoic Tethys during the Early Carboniferous (Göncüoğlu et al., 2007; 2000). The metamorphism of this basement assemblage of SCT is attributed to the Variscan orogeny with Carboniferous (330-310 Ma) ages from Pulur, Kazdağ and Gümüşhane massifs (Topuz et al., 2004, 2007; Okay et al., 2006).

On the other hand, the Cimmerian terranes are defined by the Karakaya Complex and Küre-Yusufeli ophiolites (Göncüoğlu; 2010). The Karakaya Complex mainly displays a mélange character, where metabasaltic and metaclastic rocks form the bulk lithology. Within the complex, carbonate and chert blocks are common, whose ages can be as old as Devonian (Okay et al., 2011). The Karakaya Complex represents a subduction/accretion prism formed due to the subduction of Paleotethys Ocean, which amalgamates to the SCT during the Late Triassic (Okay and Göncüoğlu, 2004; Sayit et al., 2010; Sayit and Göncüoğlu, 2013). Both basement assemblages are covered with a continuous succession of Jurassic-Cretaceous platform sediments. Starting from the Late Cretaceous, slope-type sediments covered by flysch-type deposits with ophiolitic blocks dominates, which were derived from the Intra-Pontide Ocean to the north (Göncüoğlu, 2010; Göncüoğlu et al., 2000).

The final oceanic member of this mosaic is the representatives of the Neotethyan oceanic units: The İzmir-Ankara Ocean to the south and the Intra-Pontide Ocean to the north of the SCT (Şengör and Yılmaz, 1981). The Intra-Pontide Ocean is located between the Istanbul-Zonguldak Terrane and SCT (Yılmaz, 1990; Göncüoğlu et al.,

1997, 2008; Marroni et al., 2020) the İzmir-Ankara Ocean is located between the SCT and Tauride-Anatolide Platform (Göncüoğlu, 2010).

The complete consumption of both Paleo- and Neo- tethyan oceanic lithospheres can be traced along a geotraverse across the SCT (Göncüoğlu et al., 2000). Therefore, considering the paleo-geographic location and the assemblages of the SCT, its geodynamic understanding stands as a key to understand the geology of Northwest Turkey, as well as its geodynamic evolution.

1.2.2 Söğüt Metamorphics

Central Sakarya Terrane (CST) is one of the basements assemblages of SCT. It is composed of two distinctive pre-Jurassic basement units of its own; namely the Permo-Triassic Karakaya Complex and the Paleozoic Söğüt Metamorphics (Göncüoğlu et al., 1997; 2000).

The examination of the CST starts off by Altınlı (1975), who prepared the first 1/25.000 map of the area. In this study, the metamorphic rocks, the granitic body intruding the metamorphics, and the Jurassic cover sequence were mapped, and their geological relationships were discussed. Following this study, the E-W elongated metamorphic assemblages encompassed within Söğüt, İnhisar, Mihalgazi, and Sarıcakaya provinces, and the cross-cutting granitic rocks were examined in detail by Yılmaz (1976; 1977; 1979; 1981; 1985), Ayaroğlu (1978), and Şentürk and Karaköse (1979). These studies interpreted all the metamorphic assemblages within this area to be the regional basement rocks and treated them as a single unit.

On the other hand, the first detailed mapping and study of the Paleozoic metamorphic assemblage were conducted by Göncüoğlu et al. (1996). Although the term “Söğüt Metamorphics” was previously used by Şentürk and Karaköse (1979), the Karakaya Complex units and the cross-cutting granitoids were also classified as members of the Söğüt Metamorphics in their study. However, Göncüoğlu et al. (1996) interpreted the Söğüt Metamorphics as a distinctive assemblage which stands as the structurally

higher unit relative to the Karakaya Complex within the area. According to this classification, the Söğüt Metamorphics consists of migmatite, amphibolite, para- and ortho-gneisses, staurolite-bearing schists, mica schists, and seldomly occurring lenses of quartzite and marble. Furthermore, a medium- to high-grade amphibolite facies metamorphism is determined by paragenesis within the metapelites (Göncüoğlu et al., 1996; 2000). In addition, Göncüoğlu et al. (1997) further classified the Tozman Metaophiolite as a body of melano- and leuco-gabbro and serpentinite with well-developed cumulate texture which is tectonically emplaced and occurs a discontinuous lens (Yaşar et al., 2019). Ustaömer et al. (2012) and Othman (2016) also mentioned these cumulate gabbroic and ultramafic rocks, yet there is no consensus on their petrological and geodynamic evolution.

The Söğüt Metamorphics were intruded by several plutonic bodies of Carboniferous age (319-327 Ma) during the Variscan Orogeny, known as the Sarıcakaya Granitoid, consisting of blasto-mylonitic granodiorite, quartz-diorite, and granite cross-cut by grey-pink aplitic and pegmatitic quartz-feldspar dykes (Yılmaz, 1979; Yılmaz, 1990; Göncüoğlu et al., 1996; 2000; Ustaömer et al., 2012; Othman, 2016; Othman and Hassan, 2018; Uğurcan et al., 2019; Topuz et al., 2020). The Sarıcakaya Granitoid displays calc-alkaline, I- to S-type geochemical features, and interpreted to have formed in a magmatic arc (Kibici et al., 2010; İlbeyli et al., 2015) or syn-collisional setting (Ustaömer et al., 2012; Othman and Hassan, 2018).

Several researchers (Altıner et al., 1991; Koçyiğit et al., 1991; Ocakoğlu et al., 2019; Şengün and Koralay, 2019; Şengün et al., 2020) studied in detail the Liassic clastics of Bayırköy Formation (Granit ve Tintant, 1960) and Jurassic platform carbonates of Bilecik Limestone (Granit ve Tintant, 1960) that unconformably covers the Söğüt Metamorphics, the cross-cutting Sarıcakaya Granitoid, and the Karakaya Complex. Demirkol (1997) conducted detailed mapping of the Tuzaklı-Gümele Fault (extended towards east by Göncüoğlu et al., 1996), indicating that the CST basement thrusted towards south on to the Tertiary lithologies. In recent studies, the Tuzaklı-Gümele Fault is referred to as the Söğüt Thrust (Mueller et al., 2019) and Nallıhan-Sarıcakaya Thrust (Okay et al., 2020). The Tertiary rock assemblage in the studied

area is made up of the Paleocene clastics of Kızılçay Formation (Eroskay, 1965), the Pliocene clastics of Örencik Formation, and the Eocene Bozaniç Volcanics, which cross-cuts the clastic assemblages (Göncüoğlu et al., 1996; 2000). Büyükkahraman (2013) and Yıldız et al. (2015) revealed that the calc-alkaline andesitic pyroclastics and lavas of Bozaniç Volcanics were formed due to post-collisional continental arc magmatism as a result of collision of the Sakarya Composite Terrane and Tauride-Anatolide Composite Terrane.

Previously, the age of the Söğüt Metamorphics was designated as pre-Carboniferous by correlating the zircon ages retrieved from the intruding Sarıcakaya Granitoid (Göncüoğlu et al., 1987; Yılmaz, 1990; Delaloye and Bingol, 2000; Göncüoğlu et al., 2000; Ustaömer et al., 2012; Okay and Nikishin, 2015; Okay and Topuz; 2017). On the other hand, recent geochronological studies expanded the age constraints for the Söğüt Metamorphics. Ustaömer et al. (2012) presented detrital zircon U-Pb ages from the sillimanite-bearing schists within a range of 2738-551 Ma. In addition, Mueller et al. (2019) provided detrital zircon U-Pb ages from a paragneiss sample with a prominent Ordovician peak. Uğurcan et al. (2019) provided crystallization ages of igneous protoliths of orthogneisses (473-503 Ma, Cambrian-Early Ordovician) and amphibolites (472 Ma, Early Ordovician) by zircon U-Pb geochronology. Furthermore, Topuz et al. (2020), also provided zircon U-Pb ages for the same rocks and presented Silurian igneous crystallization ages (430-435 Ma for orthogneiss; 419-434 Ma for amphibolite). In addition, Uğurcan et al. (2019) introduced Ar-Ar ages of biotites and muscovites from paragneisses as 335 and 331 Ma (Early Carboniferous), respectively and associated these ages with metamorphism and exhumation of the area. Finally, Şengün et al. (2020) published U-Pb lower intercept ages of detrital rutiles as 346 Ma and 319 Ma (Carboniferous) from sandstone samples of Bayırköy Formation and interpreted these results to constrain the metamorphism age of the Söğüt Metamorphics.

Göncüoğlu et al. (1996; 2000) suggested an island-arc tectonic setting for the protoliths of the Söğüt Metamorphics, considering the presence of ophiolitic assemblages and the geochemical characteristics of the intruding granitoids. On the

other hand, combined with geochemical analysis, Topuz et al. (2020) proposed a continental-rift setting to produce the acidic (protoliths of orthogneisses) and basic (protoliths of amphibolites) magmatism. Furthermore, for the protoliths of the schists, the provenance study conducted by Ustaömer et al. (2012) indicates a derivation from the Arabian-Nubian Shield located to the north of Gondwana.

1.3 Geographic Setting

The study area is to NW of Eskişehir, located to the North of Sarıcakaya, Mihalgazi, and İnhisar towns covering an area of ~200 km^2 (Figure 1.2). The geographic coordinates are approximately 40º 01'-40º 06' N and 30º 25'-30º 39' E, which falls in the H24-c3, H25-d4, and H25-d3 quadrangles of the 1:25.000 scaled topographic maps of Turkey. The high peak of the area is the Tozman Plateau, located to the north of Tozman village. The study area is located on a rough terrain, a mountain range including a large forest, which makes both mapping and sampling quite challenging.

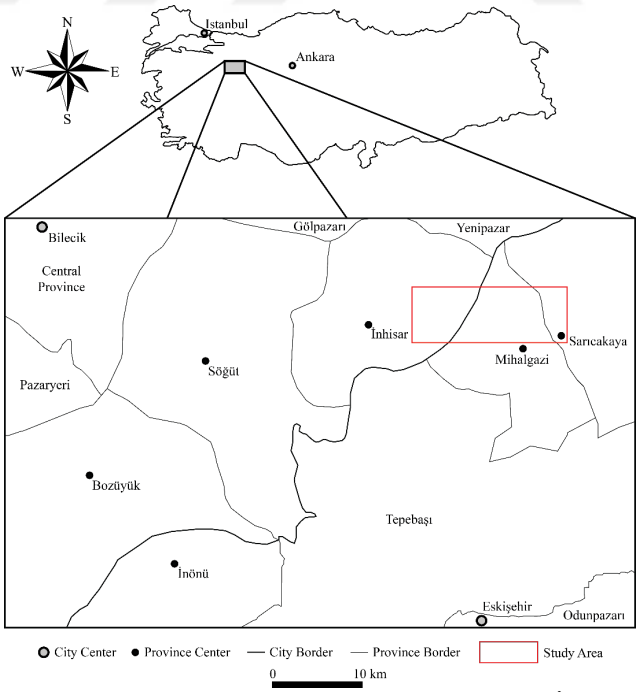


Figure 1.2 Location map of the study area, located within İnhisar, Mihalgazi, and Sarıcakaya provinces.

1.4 Methods of Study

The thesis study was conducted under two major divisions; fieldwork and laboratory work. Detailed information is provided under each sub-section below.

1.4.1 Fieldwork

Fieldwork was conducted during Spring 2019 and included the revision of the geological map from Göncüoğlu et al. (1996; 2000), Duru et al. (2002), and Gedik and Aksay (2002). Furthermore, 48 samples (14 amphibolite and 17 para- and ortho-gneisses of Söğüt Metamorphics, 11 melano- and leuco-gabbros of Tozman Metaophibolite and 6 quartz-diorite of Sarıcakaya Granitoid) was collected for thin section, whole-rock geochemistry, U-Pb geochronology analysis. As zircon separation would be conducted on amphibolites, in which the zircon occurs in low amounts, the sampling was conducted in large quantities (~ 50 kg/sample). The area was divided into four sections, cross-cutting the basement perpendicular (N-S) to oblique, and sampling was conducted accordingly.

1.4.2 Laboratory Work

Laboratory analysis was conducted in three parts; (1) petrography, (2) whole-rock geochemistry, and (3) U-Pb geochronology.

1.4.2.1 Petrographic Analysis

Petrographic analysis was conducted for 44 samples in total; 14 amphibolites, 17 para- and ortho-gneisses, 11 melano- and leuco-gabbros, and 2 diorites. Thin sections were prepared from the collected samples in Middle East Technical University thin-section preparation laboratory.

The weathered parts are removed from the collected samples with a diamond-edged saw to a rectangular prism. The prepared slab is then abraded on a diamond-embedded disc to smoothen the slab surfaces. Further polishing is proceeded with using 320-400-600 μm Carborundum powder respectively on a glass disc until the surface that is chosen for thin section preparation is completely polished and smooth. Then a glass with 26*76 mm side length and 1.2 mm thickness is glued on to the polished surface and left for 24 hours to dry. The side without the glued thin-section glass is then trimmed with a diamond-saw, and the sample thickness is reduced to 0.03 mm, and again polished using the 320-400-600 μm Carborundum powder respectively. During the polishing stage, the thin section is checked constantly to ensure that the mineral properties are observable, and the thickness is precise. The side with the sample is covered with Canada Balsam and covered with a cover glass and left to dry out. After the sections are completely dry, they are put into pure alcohol, to remove any access glue or Canada Balsam for 30 mins. Finally, the thin sections are wiped with a cotton cloth which completes the process.

The thin sections of the metamorphic samples are prepared from surfaces that are perpendicular to the foliation (for samples on which foliation is observable) so that the textural properties can be observed clearly. The petrographic analysis revealed the mineral paragenesis of each lithology as well as associated textures. These properties provided the prograde and retrograde metamorphic assemblages. The properties that may or may not be present in the outcrop scale were determined for the complete understanding of a sample. The whole-rock analysis of the samples is then interpreted considering these properties. Finally, the occurrence and/or dis-occurrence of minerals that are suitable for geochronological applications are also determined via petrographic examinations. Samples, including such minerals or conditions, are chosen for zircon separation that underwent geochronological analysis.

1.4.2.2 Whole-Rock Geochemistry Analysis

Whole-rock geochemistry analysis was conducted for 14 amphibolite samples. Samples were chosen considering their field relationship, outcrop and petrographic textural properties, mineral assemblages, and field distribution. The pre-preparation of the samples was concluded in the Department of Geological Engineering, Middle East Technical University (METU) sample preparation laboratory, and crustal research laboratory. Final preparation was conducted in ALS Global Sample Preparation Laboratories in İzmir, Turkey. The analysis was conducted with the ME-MS81d analytical package of ALS Global. The lithium borate-fusion, nitric acid digestion, Inductively Coupled Plasma Atomic Emission Spectroscopy (ICP-AES), and Inductively Coupled Plasma Mass Spectrometry (ICP-MS) analysis was concluded in ALS Global Laboratories in Dublin, Ireland.

The sample preparation for the geochemical analysis starts at the sampling stage in the field. Using tools such as a sledgehammer, geological hammer, and split wedge, samples were collected from relatively less altered, if possible un-altered, and/or un-weathered parts. In the laboratory, samples from the chosen outcrops were trimmed with diamond-edge saw into slabs of ~ 4x4 cm rectangular prisms, by removing the weathered and intensively altered parts as well as any possible inclusions, enclave or xenolith-if there are any. The surfaces and corners of the prepared slabs are then abraded using a diamond embedded disk to remove any saw tracks left, which can result in elemental contamination that is originally non-existent. Finally, polishing is concluded using a glass-disc with 900 μm Carborundum powder, removing any possible contamination from all the surfaces of each sample. Samples are then brushed under tap water, then washed with pure water, and left to dry out naturally in a dust-free environment.

Samples are then crushed to 70% less than 2 mm, and riffle split off 250 g. The material is then pulverized further to 85% passing 75 μm. The crushers and pulverizes are cleaned with barren material and air cleaned with compressed air between each sample. The solution from the sample powder of each sample is

prepared with first lithium-borate fusion and then nitric acid dissolution. The major oxide ratios are measured for weight percent with ICP-AES finish and the Loss on Ignition (LOI) is measured at 1000 ℃ by furnace within the detection limits provided in Table 1.1 (ME-ICP06, ALS Global). Although the solution preparation for trace elements, including REEs, is conducted following the same procedure, the analysis is concluded with ICP-MS within the detection limits provided in Table 1.1 (ME-MS81, ALS Global). Blank, duplicate, and standard samples were used during the analysis to ensure quality assurance (QA)/quality check (QC).

Table 1.1. Detection limits of ME-ICP06 (values are in wt. %) and ME-ICP81 (values are in ppm) analysis.

ME-ICP06		ME-ICP81			
Al_2O_3	0.01-100	**Ba**	0.5-10,000	**Pr**	0.03-1,000
BaO	0.01-100	**Ce**	0.1-10,000	**Rb**	0.2-10,000
CaO	0.002-100	**Cr**	10-10,000	**Sm**	0.03-1,000
TiO_2	0.01-100	**Cs**	0.01-10,000	**Sn**	1-10,000
Fe_2O_3	0.01-100	**Dy**	0.05-1,000	**Sr**	0.1-10,000
K_2O	0.01-100	**Er**	0.03-1,000	**Ta**	0.1-2,500
Na_2O	0.01-100	**Eu**	0.03-1,000	**Tb**	0.01-1,000
P_2O_5	0.01-100	**Ga**	0.1-1,000	**Th**	0.05-1,000
SiO_2	0.01-100	**Gd**	0.05-1,000	**Tm**	0.01-1,000
SrO	0.01-100	**Hf**	0.2-10,000	**U**	0.05-1,000
MnO	0.01-100	**Ho**	0.01-1,000	**V**	5-10,000
MgO	0.01-100	**La**	0.1-10,000	**W**	1-10,000
LOI	0.01-100	**Lu**	0.01-1,000	**Y**	0.1-10,000
		Nb	0.2-2,500	**Yb**	0.03-1,000
		Nd	0.1-10,000	**Zr**	2-10,000

1.4.2.3 U-Pb Geochronology Analysis

Zircons from 6 amphibolite samples (~50 kg/sample) were separated for U-Pb geochronology. The separation was proceeded in two parts; crushing, pulverizing and sieving stages are conducted in Geological Engineering Department, METU and METU Central Laboratory; separation with wilfley table, magnetic separation, heavy liquid separation, hand-picking under binocular microscope, epoxy-mount preparation, and grinding and polishing of the epoxy mounts were completed in the

Mineral Separation Laboratory of Geological Engineering Department, Dokuz Eylül University (DEU).

Samples are first crushed using a jaw crusher, and then pulverized using disk and/or cylindrical mill. The pulverized material is then sieved to separate the fractions <63 μm, 63-500 μm, and >500 μm. The fraction of >500 μm is pulverized again, and 63-500 μm fraction is sieved out again to increase the fraction, which will be further processed in the wilfley table. Using a wilfley shaker table, minerals are separated with respect to their density. The heaviest fraction is then oven heated for 24 hours to dry out. Afterwards, magnetic minerals (e.g. hornblende, biotite) were separated with respect to their magnetic properties, whereas the remaining non-magnetic portion included the zircon grains. The non-magnetic portion is then separated using two different heavy liquids of Merck; (1) bromoform (2.89 g/cm^3) and (2) diiodmethane (3.3 g/cm^3). The separation with bromoform separated the zircon- (4.65 g/cm^3), apatite- (3.19 g/cm^3) and sphene- (3.48 g/cm^3) rich fractions from the relatively light minerals, such as plagioclase (2.69 g/cm^3). Both fractions are then oven-dried for 24 hours to remove the chemical from the minerals, as it is toxic. Heavy liquid separation is concluded with diiodmethane which separates the apatite grains from sphene and zircon grains. Fractions are again oven-dried for 24 hours. The final separation is proceeded under binocular microscope, by which zircons grains with euhedral shape (tetragonal), high reflection, and free of inclusions were hand-picked.

Out of 6 samples, ~525 zircon grains were hand-picked and lined up on four adhesive double-sided carbon bands considering their relative grain sizes, in an area of 19 mm diameter. The mount ring with 25 mm is then placed covering the zircon grains, and resin is poured on top very carefully, without leaving any air bubble in between the grains. The prepared mounts are then left to dry out on their own for 24 hours. The carbon bands are then removed, and the mount sides with the zircon grains are ground and polished with 320 μm carborundum powder, as to abrade approximately 1/3rd of the grains and reveal their internal structure.

The cathodoluminescence (CL) and back-scatter (BS) images of zircon grains are then taken in Korea Basic Science Institute (KBSI), revealing the fractures, inclusions, and zonation of zircon grains. Out of 231 zircons, 245 spots were selected. Spots were selected from surfaces that are free of fractures and inclusions and preferably, showing well-developed zonation. These selected spots are measured for U-Th-Pb ratios with Laser Ablation Multi-Collector Inductively Coupled Plasma Mass Spectrometry (LA-MC-ICP-MS) in KBSI using NWA193^{UC}, ESI laser system coupled with Nu Plasma II MC-ICP-MS system. Spots of 12 μm diameter were ablated for 30 seconds with a fluence of 0.3 J/cm^2 and a repetition rate of 5 Hz. U, Th, and Pb ion signals were measured by respective faraday cups. The retrieved signals were processed with Iolite 2.5 within the Igor Pro 6.3.5.5 software (Paton et al., 2011), which are further analyzed using IsoPlot (Ludwig, 2008) macro on excel for the generation of concordia diagrams (Tera and Wasserburg, 1972) and the calculation of $^{206}Pb/^{238}U$ weighted-mean ages.

Two well-established zircon standard samples, 91500 and Plešovice, were used during the measurements to ensure QA/QC standards. 91500 standard zircon is retrieved from a syenite outcrop in Renfrew Country, Ontario, Canada (Jackson et al. 2004), and its age is published by Wiedenbeck et al. (1995) as 1065.4 ± 0.6 Ma. The retrieved age during the analysis of this study yielded a concordia age of 1062.8 ± 1.8 Ma, consistent with the published age. Plešovice standard zircon is retrieved from a granulite in the Bohemian Massif, Czech Republic, and its age is published as 342.1 ± 5.9 Ma (Slama et al., 2008). The retrieved age during the analysis of this study yielded an intercept age of 337.31 ± 0.47 Ma, again consistent with the published age (Appendix C). The use of standard samples during the analysis ensured the accuracy of measurements and dismissed any possibility of analytical error.

CHAPTER 2

GEOLOGY

2.1 Regional Geology

Sakarya Composite Terrane (SCT) (equivalent to the part of the Pontides of Ketin, 1966, Sakarya Continent and Rhodope-Pontide Fragment of Şengör et al., 1984, and Sakarya Zone of Okay et al., 1996), is bounded by the Intra-Pontide Suture to the north with the İstanbul-Zonguldak Terrane and by the İzmir-Ankara-Erzincan Suture (İAES) to the south with the Tauride-Anatolide assemblages. SCT extends as a 100-200 km wide, 1500 km long, E-W trending belt (Figure 2.1), and comprises several Variscan and Cimmerian oceanic and continental tectonic assemblages in its Pre-Jurassic basement (Göncüoğlu et al., 1997; 2000).

The Central Sakarya Terrane (CST) consists of two major basement units; i) a Variscan basement including the Söğüt Metamorphics, and ii) the Cimmerian Karakaya Complex comprising the Tepeköy Metamorphics (equivalent to the Söğüt Metabasites of Yılmaz, 1979; Greenschist-Marble Association of Şentürk and Karaköse, 1979; Nilüfer Unit of Okay et al., 1991; and redefined Nilüfer Unit of Sayit et al., 2010) and Soğukkuyu Metamorphics (equivalent to the Karakaya Formation of Bingöl et al., 1975; and Hodul and Çal Units of Okay et al., 1991). Karakaya Complex, made up of metabasalts intercalated with recrystallized limestone blocks, is observed in the study area as the structurally lower tectonic slice, whereas the Söğüt Metamorphics, the focus of this study, stands as the structurally higher tectonic slice and is interpreted as the basement of SCT.

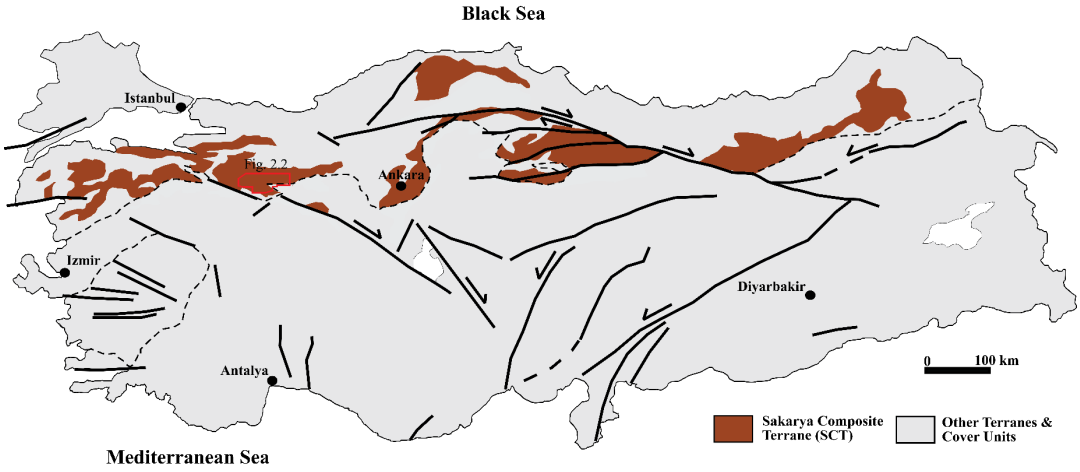


Figure 2.1. Distribution of the Sakarya Composite Terrane (SCT) in Turkey (Modified from Göncüoğlu, 2019). Inset border shows the study area.

The closure of northern branch of the Neotethys ocean amalgamated the Central Sakarya Terrane basement assemblage with the ophiolitic mélange of İzmir-Ankara-Erzincan Ocean, via the İzmir-Ankara-Erzincan Suture, the primary contact being in between the Permian-Triassic Karakaya Complex and Late Cretaceous Dağküplü Ophiolitic Melange (Figure 2.2). The Karakaya Complex is composed of several sedimentary/tectonic mélange units including metabasaltic blocks (generally metamorphosed under greenschists-facies) intercalated with recrystallized neritic and pelagic limestones, mudstone and minor chert as well as low-grade metaclastic rocks and greywacke (Sayit and Göncüoğlu, 2013). As introduced before, the Karakaya Complex is divided/defined into several sub-units considering their assemblages, chemical affinities, metamorphic grades and relative positions with respect to each other (For more information on this unit, see Tetiker et al., 2015, Sayit et al., 2010, and Okay and Göncüoğlu, 2004). The Karakaya Complex represents the remnants of a subduction/accretion prism of the Paleotetyhan ocean during its closure. On the other hand, the Dağküplü Ophiolitic Mélange, representing the remnants after subduction/accretion of Neotethyhan ocean, is composed of blocks of spilitic metabasalts, serpentinites, glaucophane-lawsone schists, radiolarian cherts, pelagic limestones and recrystallized neritic limestones with minor blocks of amphibolites, gabbros, pyroclastics, and andesites-dacites of Sarıyer

Complex, and tectonic slivers of block-in-matrix-type allolistostromes of Emremsultan Olistostrome (Göncüoğlu et al., 2000; 1996).

Finally, within the Central Sakarya Terrane, E-W elongated, south-verging compressional tectonics caused the thrusting of the Paleozoic basement assemblages on to the Karakaya Complex, before the unconformable deposition of the Liassic-Cretaceous cover of clastics and carbonates. Together with their cover, the CST basement thrusted onto Tertiary rocks to the south via the Tuzaklı-Gümele Thrust. The study area is located to the north of the İzmir-Ankara-Erzincan Suture and envelopes a major portion of the Paleozoic Basement of CST (Figure 2.2).

2.2 Local Geology

In the Central Sakarya Terrane, the Söğüt Metamorphics stands as the structurally higher unit and is one of the basement rock assemblages of the Sakarya Composite Terrane. Although the evolution of the Söğüt Metamorphics in terms of its tectonomagmatic setting and metamorphic history is debated, its post-metamorphic evolution with respect to its contact units is fairly well understood and well observed during the field study.

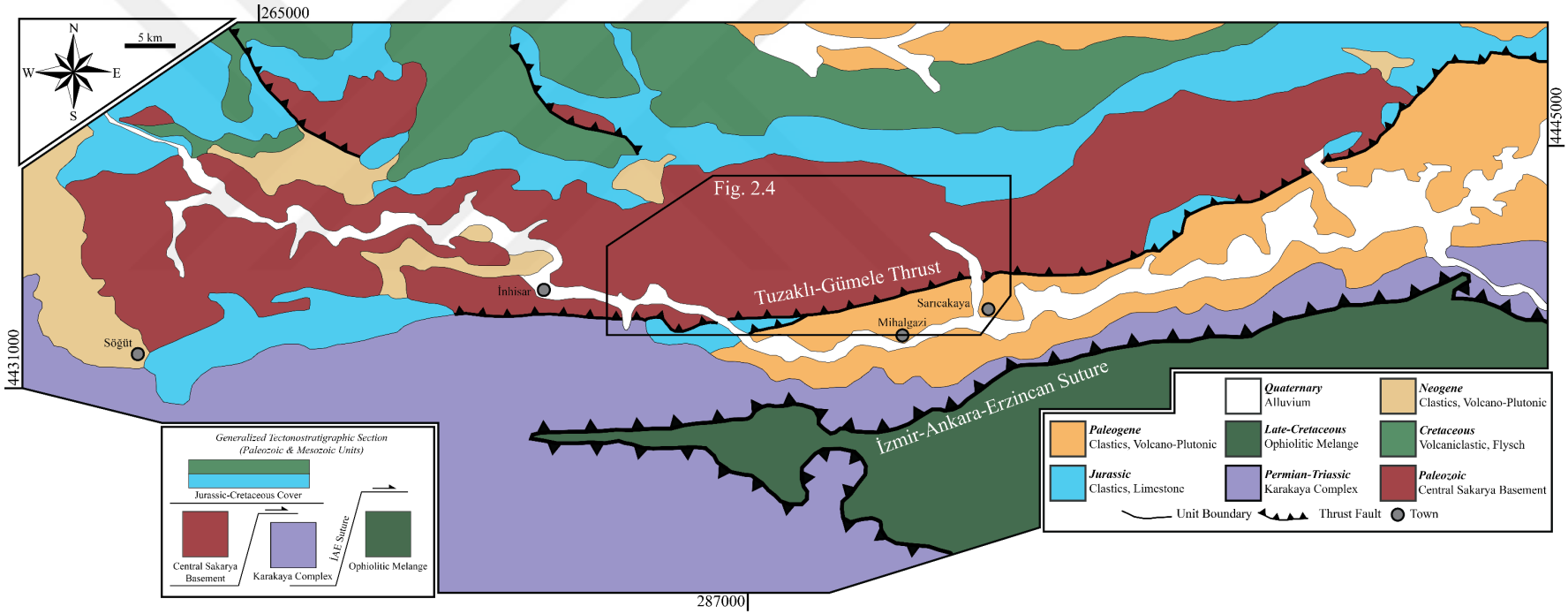


Figure 2.2. Regional map and generalized tectonostratigraphic section of the Paleozoic and Mesozoic units of the region (Modified from the 1/500.000 geological map of Turkey, MTA, 2004; Duru et al., 2002; Gedik and Aksay, 2002; Göncüoğlu et al., 1996; Şentürk and Karaköse, 1979). Inset border shows the study area.

The Söğüt Metamorphics is dominantly made up of para- and ortho-gneisses, intercalated with amphibolites, which will be explained in detail in further sub-sections. Yet, there is also documented schists, and a minor amount of marble. In addition, there is a tectonic slice of mafic-ultramafic rocks of Tozman Metaophiolite with unknown age emplaced within the Söğüt Metamorphics. In addition to these metamorphic units, the granite-granodiorite-diorite of Sarıcakaya Granitoid, metabasic rocks of Karakaya Complex, clastic successions of Bayırköy Formation, carbonates of Bilecik Limestone, clastic successions of Kızılçay Formation and andesitic Bozaniç Volcanics outcrop in the study area. Yet, this study is focused mainly on the Söğüt Metamorphics with minor complementary observations on the Tozman Metaophibolite and Sarıcakaya Granitoid.

The Sarıcakaya Granitoid crosscut the basement assemblage during the Late Carboniferous magmatism in the Variscan Orogeny. The metamorphic assemblage together with the cross-cutting granitoid was thrusted onto the Karakaya Complex (metabasic schists with marble blocks) prior to the deposition of the unconformable Jurassic sequences of clastic rocks (red-colored conglomerate, sandstone, and claystone intercalations of the Bayırköy Formation) that grades into carbonates (white-pinkish-colored Bilecik Limestone). This relationship is well observed to the north of the study area, to the North of Sarıcakaya Town (Figure 2.3-B), and to the north of Tozman Village, in the Tozman plateau (not shown on the map). The Central Sakarya Basement (CSB) and Karakaya complex, covered with the Jurassic sequences are then thrusted onto the Paleocene Kızılçay Formation (red-colored conglomerate, sandstone, and claystone), crosscut by the Eocene Bozaniç Volcanics (black andesitic basalts with grey-colored pyroclastic rocks) (Figure 2.3-A). The primary faulted contact is the 80 km-long Tuzaklı-Gümele thrust between the CSB and the Kızılçay Formation (Figure 2.3-A, 2.4).



Figure 2.3. Contact relationships between the Central Sakarya Terrane units: (A) The contacts between SM, KF, and BV. SM is thrusted onto the tertiary rock assemblages. (B) The unconformity between the SM, and Jurassic BF and BL succession. SM: Söğüt Metamorphics; KF: Kızılçay Formation; BV: Bozaniç Volcanics; BF: Bayırköy Formation; BL: Bilecik Limestone.

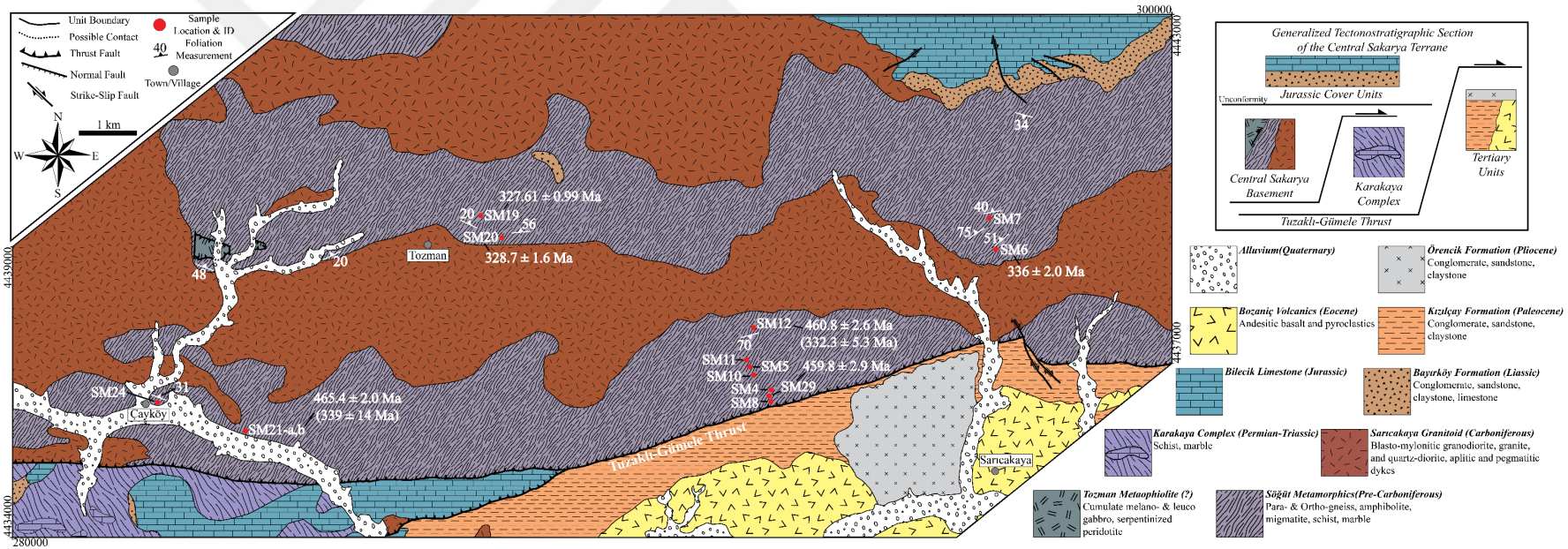


Figure 2.4. Geological map and generalized tectonostratigraphic relationships between the Central Sakarya Terrane units (Modified from Göncüoğlu et al., 1996; Duru et al., 2002; Gedik and Aksay, 2002). Sample locations of the analyzed amphibolite samples are marked on the map.

2.2.1 Söğüt Metamorphics

2.2.1.1 Para- and Ortho-Gneisses

Gneiss bodies are the dominating lithologies of the Söğüt Metamorphics and observed as pelitic sillimanite-cordierite-bearing paragneisses, and ortho-gneisses with a quartzo-feldspathic granitic protolith, with and without augen texture. They were observed as the host rock of amphibolites.

The paragneisses making up to 50% of the Söğüt Metamorphics are especially dominant to the north of Sarıcakaya and show well-developed leuco- and melano-somes with E-W foliation trough out the metamorphic belt. The leucosomes with thicknesses varying between 2 mm to 2-3 cm, were dominated with muscovite (pearly), quartz (smoky-white), and feldspar (pale-pink) minerals with grain sizes varying between 1 mm to 1 cm. On the other hand, the melanosomes were dominated by biotite and a minor amount of hornblende (both are black-colored) with grain sizes varying between 0.5 to 1 mm. Quartz porphyroclasts (ϕ-type) with up to 3-5 cm core diameters (Figure 2.5-C) were observed in the paragneisses orientated parallel to the foliation surfaces, indicating no sense of shear. Furthermore, migmatitic fabrics with deformation textures were observed, similar to those found in the amphibolites (Figure 2.5-A, B). Paragneisses appear to be deformed in a ductile manner, as indicated by the folded leuco- and melano-somes and existence of porphyroclasts. Outcrops of paragneisses are generally weathered, yet alteration was not apparent.

Orthogneisses were observed dominantly to the east and west of Tozman Village. They make up ~ 20-25% of the Söğüt Metamorphics. The mineralogy consists of quartz-feldspar-plagioclase with grain sizes of 1-2 mm, and the augen texture was identified by pink feldspar porphyroclasts with grain sizes of 1-2 cm. The existence of orthogneisses indicates a granitic protolith, which in turn may imply a felsic magmatism during their pre-metamorphic evolution of the area. Orthogneisses show

both ductile and brittle deformation signatures; ductile deformation is defined by the presence of feldspar porphyroclasts, whereas brittle deformation is characterized by joint development. Contrary to the migmatitic fabrics observed in the paragneisses, a similar observation was not apparent for the orthogneisses. The outcrops of orthogneisses are generally both weathered and altered (Figure 2.5-F), yet one fresh outcrop was found at the entrance of Tozman Village from the south (Figure 2.5-E).

In the outcrops of both para- and ortho-gneisses, similar to the cross-cutting veins observed on the amphibolites, the quartzo-feldspathic veins were observed cross-cutting the paragneisses oblique and/or perpendicular to the foliation (Figure 2.5-D). In addition, the overall foliation measurements that were collected from both para- and ortho-gneisses indicates a conformable trend of south-verging deformation, conformable with the E-W elongated Tuzaklı-Gümele Thrust. Confirming the foliation measurements and the regional trusting, imbricated E-W elongated south-verging thrust faults/shear zones were observed, although brittle deformation was only limited to orthogneiss outcrops.

2.2.1.2 Amphibolites

The amphibolites occur as two types, considering their field relationships and petrographic features, (1) fine-grained concordant amphibolites, and (2) coarse-grained amphibolites. Within the Söğüt Metamorphics, amphibolites comprise < ~ 20% of the total mass, yet it is very hard to distinguish the exact spread. Only a relative distribution can be provided for the amphibolite types; the coarse-grained amphibolites were observed more dominantly, whereas fine-grained amphibolites were observed seldomly. Both types occur mostly weathered in the outer parts of the outcrops, and seldomly fresh, yet, it was possible to retrieve fresh samples from the weathered outcrops as well. For almost all the outcrops, joints were observed, indicative of a brittle deformation phase throughout the area.

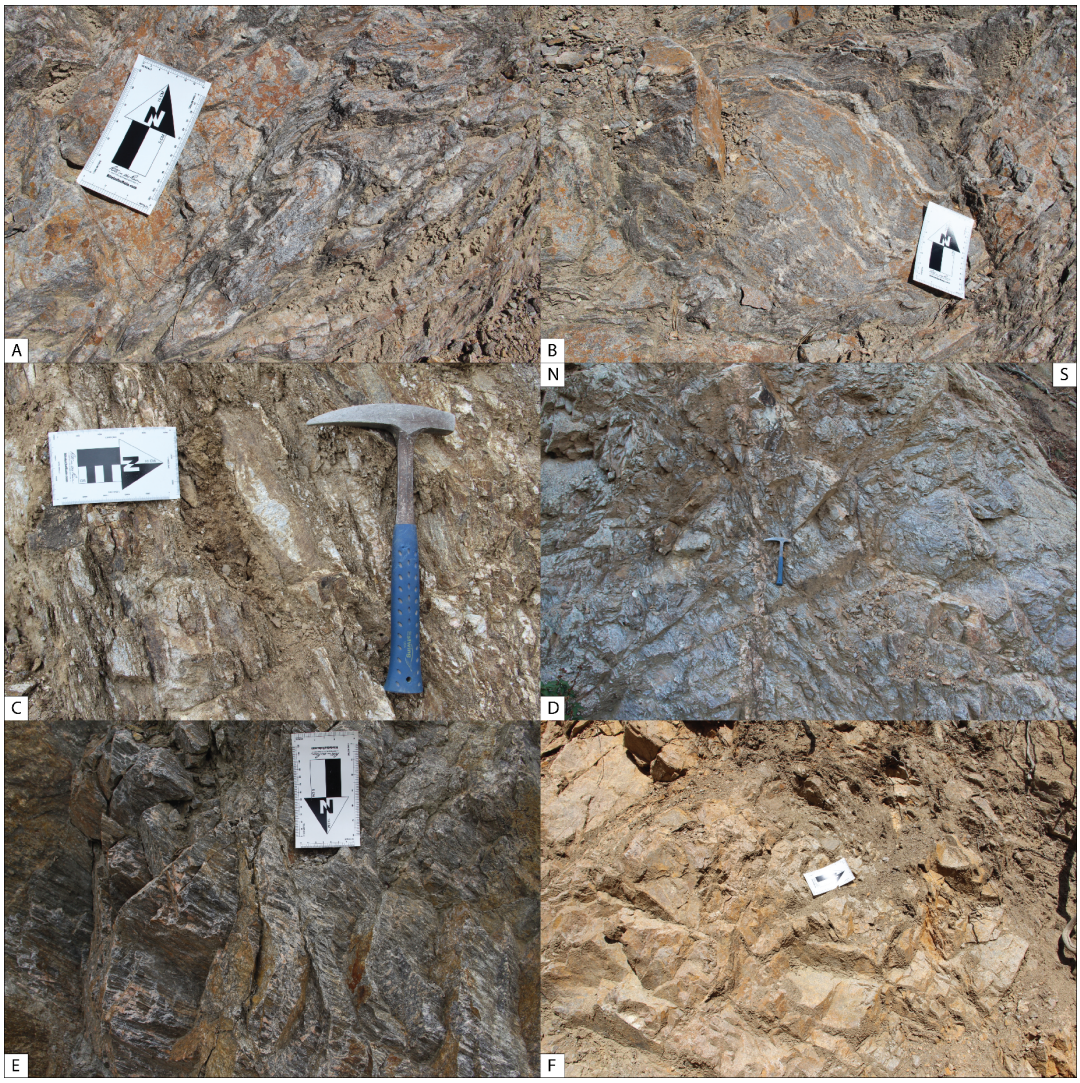


Figure 2.5. Para- and ortho-gneisses within Söğüt Metamorphics: (A-B) Paragneiss, partially melted and deformed, (C) Paragneiss with well-developed E-W foliation with a quartz porphyroclast, (D) Paragneiss with cross-cutting oblique quartzo-feldspathic vein, (E) Orthogneiss showing augen texture with abundant feldspar porphyroclasts, (F) Orthogneiss without any augen texture.

The dominantly observed coarse-grained amphibolites consist chiefly of plagioclase and hornblende, with grain sizes up to 1 mm, in the outcrop-scale with a white and black/dark green color respectively. The outcrops of fine-grained amphibolites are completely black in color, and therefore, foliation is hardly recognizable. Due to the black color, mineral identification in hand-specimen could not be maintained,

however, under thin sections of fine-grained amphibolite samples, in addition to plagioclase- and hornblende-rich mineral assemblage, biotite was also observed. The preferred orientation of biotite defines the foliation on these samples as well.

Amphibolites were observed as bands, lenses, boudins, or tectonic slices with highly sheared contacts within the host para- and ortho-gneisses having an E-W trending foliation. Although an E-W foliation was observed on several outcrops of the coarse-grained amphibolites (Figure 2.6-F), the majority of the outcrops shows no foliation (Figure 2.6-A, B). The coarse-grained amphibolite lenses were observed with thicknesses up to 50-60 m. Fine-grained amphibolites, on the other hand, occur as either boudins or sigma-shaped lenses (both with 0.5-1 m thickness) within paragneiss, having a deformation pattern coinciding with the regional deformation thrusting towards the south (Figure 2.6-C, D).

In addition, migmatitic fabrics were observed on coarse-grained amphibolites at some localities and are interpreted as indicatives of partial melting conditions. The migmatitic fabric is observed as leucosomes of plagioclase rich veins of 2-3 cm thickness with relatively minor amount of hornblende (Figure 2.6-E). This observation is further comfirmed with petrographic observations (Chapter 3) as well.

Furthermore, the intrusion of Carboniferous Sarıcakaya Granitoid was apparent with abundant quartz and quartzo-feldspathic (white to pinkish) veins of thicknesses ranging between 2 cm to 2-3 m, cross-cutting the amphibolites oblique or perpendicular to foliation (Figure 2.6-A, F).



Figure 2.6. Amphibolites within the Söğüt Metamorphics: (A) Coarse-grained amphibolite barely showing foliation with cross-cutting quartzo-feldspacthic veins, (B) Coarse-grained amphibolite with no foliation, (C) Fine-grained amphibolite boudins in a paragneiss host, (D) Sigma-shaped, deformed amphibolite lens within a paragneiss host, (E) Partial melting fabric on coarse-grained amphibolite, (F) Quartz vein cross-cutting amphibolite with well-developed foliation.

2.2.2 Sarıcakaya Granitoid

The Sarıcakaya Granitoid is well studied and documented in previous studies; therefore, the unit was examined, only to understand its relationship with the studied

amphibolites. Throughout the region, blasto-mylonitic granodiorite (mostly to the south, deformed probably due to the Tuzaklı-Gümele thrust), granite, and mainly quartz-diorite/diorite outcrops were observed (For further information, see Yılmaz, 1977; Göncüoğlu et al., 1996; Ustaömer et al., 2012; and Othman, 2016).

Most of the outcrops were variably deformed, altered, and weathered, whereas fresh outcrops of granitoids were mainly observed along the road-cuttings. Quartz-diorite intrusions are concentrated mostly to the north of Mihalgazi. The samples were dominantly made up of smoky-white quartz, black-colored biotite, and hornblende with lesser amounts of white-colored plagioclase (grain sizes vary between 0.5 to 4-5 mm); confirmed with thin section examinations. Furthermore, dark-colored, relatively fine-grained enclaves were observed seldomly in the quartz-diorite (Figure 2.7-C).

Smoky-white colored quartz and white-pinkish colored aplitic veins with varying thicknesses of 10 cm to 3 m crosscut the granitic outcrops, similar to the veins observed cross-cutting the metamorphics (Figure 2.7-A, B). To the north of Tozman village, pegmatitic muscovite (grains sizes of 2-3 cm) veins were also observed, which are interpreted to have been emplaced during the same magmatic event.

The emplacement of these veins is thought to occur at a later stage during the emplacement of the Sarıcakaya Granitoid, which was followed by the regional deformation, effects of which can be observed with local brittle faults and joints on the outcrops. In contrast, indicators of ductile deformation were not found at the outcrops that were examined.

2.2.3 Tozman Metaophiolite

The Tozman Metaophiolite outcrops as discontinuous bodies, tectonically incorporated into the the Söğüt Metamorphics. The unit it is observed to the west of Tozman Village and north of Çayköy Village on the road-cuttings. The boudins of melano- and leuco-gabbro and serpentinized peridotite show a well-developed

cumulate texture. The mafic-ultramafic assemblage is in tectonic contact with the surrounding orthogneisses as interpreted from the morphological position of the outcrops. The gabbroic rocks occur as the structurally higher unit with respect to the gneiss body in the field. The northern contact is mainly covered by soil. In addition, an intensely sheared zone was observed following the orthogneiss and gabbroic outcrops through the unit boundary (Figure 2.8-C). The E-W elongated shear zones to north and south are bounded with strike-slip faults to the east and west, distinguished by N-S elongated straight boundaries between the gabbroic and gneissic outcrops.



Figure 2.7. Lithologies and field relationships of the Sarıcakaya Granitoid: (A) The deformed nature of SG, the dioritic rocks are cross-cut by a later stage quartzo-feldspathic veins with thicknesses varying from cm to m lengths, (B) Close-up view of quartzo-feldspathic vein cross-cutting diorite, (C) Enclave within the diorite.

In their outcrops, melano- and leuco-gabbros are black and grey, respectively, and the gabbroic texture is well preserved (Figure 2.8-A, B). Leucogabbro is rich in plagioclase (grain sizes vary between 0.5-1 mm) and was distinguished with its white color, whereas other constituent minerals (i.e. clino- and ortho-pyroxene, olivine in all samples, and hornblende in one sample) were better differentiated with the petrographic examination. On the other hand, melanogabbro is rich in pyroxene and olivine minerals (both black, pyroxenes are shiny) and relatively less amount of plagioclase (white, grain sizes vary between 1-2 mm). A change in the fractionation assemblage, as indicated by the transition from plagioclase-rich leucogabbro, to olivine-pyroxene rich melanogabbro, was well observed in the outcrop scale (Figure 2.8-B). The serpentinized peridotite outcrops (Figure 2.8-D) were distinguished by the shiny surfaces, dark green/blackish color, and the mesh texture in hand specimens. White-colored chrysotile veins with well-developed fibrous habit are seldomly observed. Serpentinized peridotite, melano- and leuco-gabbros show no ductile deformation signatures, whereas, brittle deformation is apparent with several joint sets, as well as E-W elongated faults encompassed within the unit.

Even though most of the outcrops of this unit are contained within a forest, the outcrops were generally fresh, lacking alteration effects completely, and seldomly weathered. Towards east, the thin sections made from the samples revealed a semi-oriented texture of the gabbroic rocks, while preserving the cumulate texture. The rock-units of the Tozman Metaophiolite do not display any metamorphic foliation in macro- and meso-scale and are not crosscut by the Sarıcakaya Granitoid.

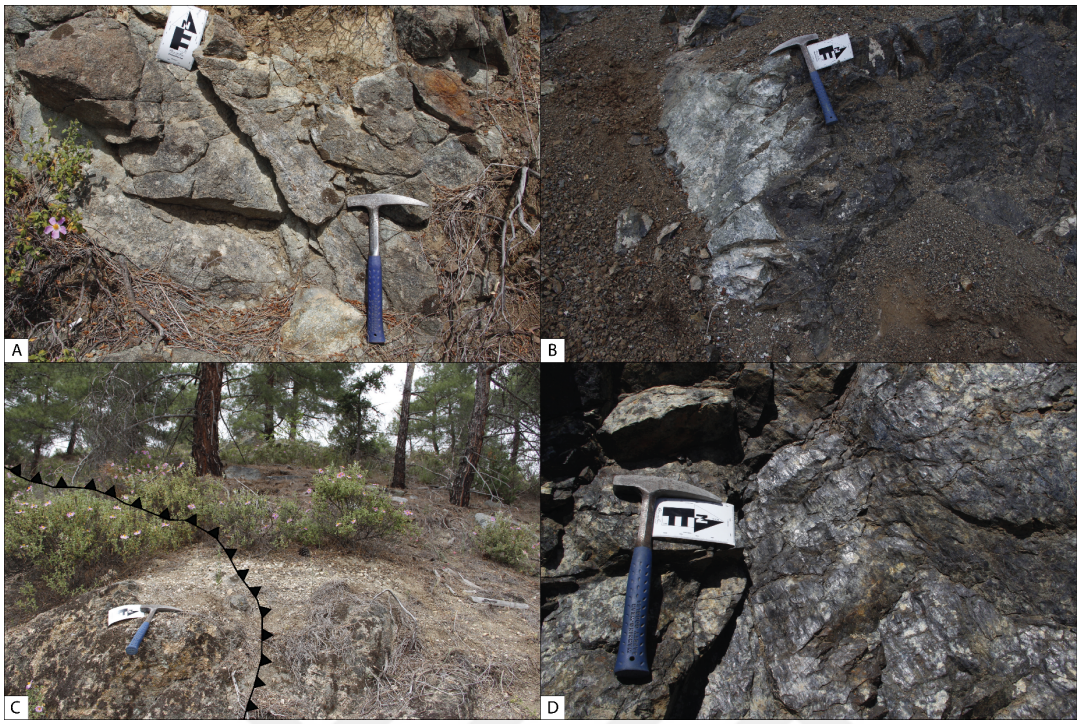


Figure 2.8. Lithologies and field relationships of the Tozman Metaophibolite: (A) Leucogabbro, (B) Leuco- and melano-gabbro transition, (C) The faulted contact between the leucogabbro of TM and the orthogneisses of SM; leucogabbro is structurally at a higher position, compared to orthogneisses, (D) Serpentinized peridotite.

CHAPTER 3

PETROGRAHY

This chapter involves a detailed description of the petrographical properties of the units within the Central Sakarya Basement; amphibolites and, para- and ortho-gneisses of the Söğüt Metamorphics, the quartz-diorites of the cross-cutting Sarıcakaya Granitoid and the gabbros and ultramafic rocks of the Tozman Metaophiolite tectonically emplaced to the Söğüt Metamorphics.

3.1 Söğüt Metamorphics

The metamorphic basement consists of para- and ortho-gneisses associated with lenses, tectonic slices, and boudins of amphibolites. Although the Söğüt Metamorphics also include minor amounts of staurolite-bearing schists, mica schists, and seldomly occurring lenses of quartzite and marble, only the amphibolites and gneisses, which are the dominating lithologies of the unit, were examined.

3.1.1 Para- and Ortho-Gneisses

Para- and ortho-gneiss are the most dominating rock type throughout the Söğüt Metamorphics and acts as the host rocks for the amphibolites. Paragneisses are observed in abundancy to the north of Sarıcakaya Town, as well as throughout the basement. On the other hand, orthogneiss outcrops were observed extensively in the western part of the study area, especially to the Çayköy and Tozman Villages. Fractures and micro-faults were not observed for either of the gneisses, removing the possibility of brittle deformation, yet the well-developed foliation and intracrystalline deformation signatures on the paragneisses confirm the existence of ductile deformation observed on the field.

Paragneisses include biotite, sillimanite, cordierite, muscovite, plagioclase, quartz, and feldspar. Biotite is pleochroic with dark red-brown color under Plane Polarized Light (PPL) and displays birefringence with 3rd order interference colors under Cross Polarized Light (XPL). Furthermore, they have moderate relief, well-developed cleavages, and display parallel extinction. Sillimanite is slightly pleochroic, grey to colorless under PPL and has a weak birefringence with 1st order interference colors under XPL. Sillimanite grains have moderate relief and display parallel extinction. Furthermore, they have a distinguishing fibrous texture. Foliation is defined with the preferred orientation of biotite and sillimanite grains. Cordierite was distinguished in relationship with biotite and sillimanite, colorless under PPL and display low birefringence with 1st order interference colors under XPL (Figure 3.1-A, B).

Colorless quartz (grey-pale yellow interference colors under XPL, with fresh surfaces) grains were observed with distinctive deformation signatures such as, sub-grain formation, undulose extinction, deformation lamella, and bulging (Figure 3.1). Furthermore, a relatively low abundance of plagioclase (slightly altered) was observed showing polysynthetic twinning as well as tapering twins, revealing the effects of deformation.

Muscovite grains were observed showing a similar preferred orientation with biotite and sillimanite. They are colorless under PPL with well-developed cleavages. Under XPL, they are strongly birefringent with 3rd order interference colors under XPL (Figure 3.1-C-F).

Zircon was observed inside the biotite grains as an accessory mineral in addition to opaque minerals. Zircon appears dark brown under XPL, while colorless under PPL, showing a characteristic decay halo and high relief (Figure 3.1-C, D).

Orthogneiss samples includes mainly mineral assemblage of quartz, biotite, plagioclase, feldspar, and muscovite. Zircon, apatite, and garnet occurs as accessory minerals. Quartz, plagioclase, feldspar, muscovite, and zircon show similar properties with those of paragneisses, as well as similar intracrystalline deformation signatures on quartz and plagioclase grains. On the other hand, for the orthogneiss

samples, biotite is pale-dark brown under PPL, instead of the distinctive dark-red colors observed for the paragneiss samples. Furthermore, birefringence was observed, masked by body color, with 1st to 2nd order interference colors under XPL.

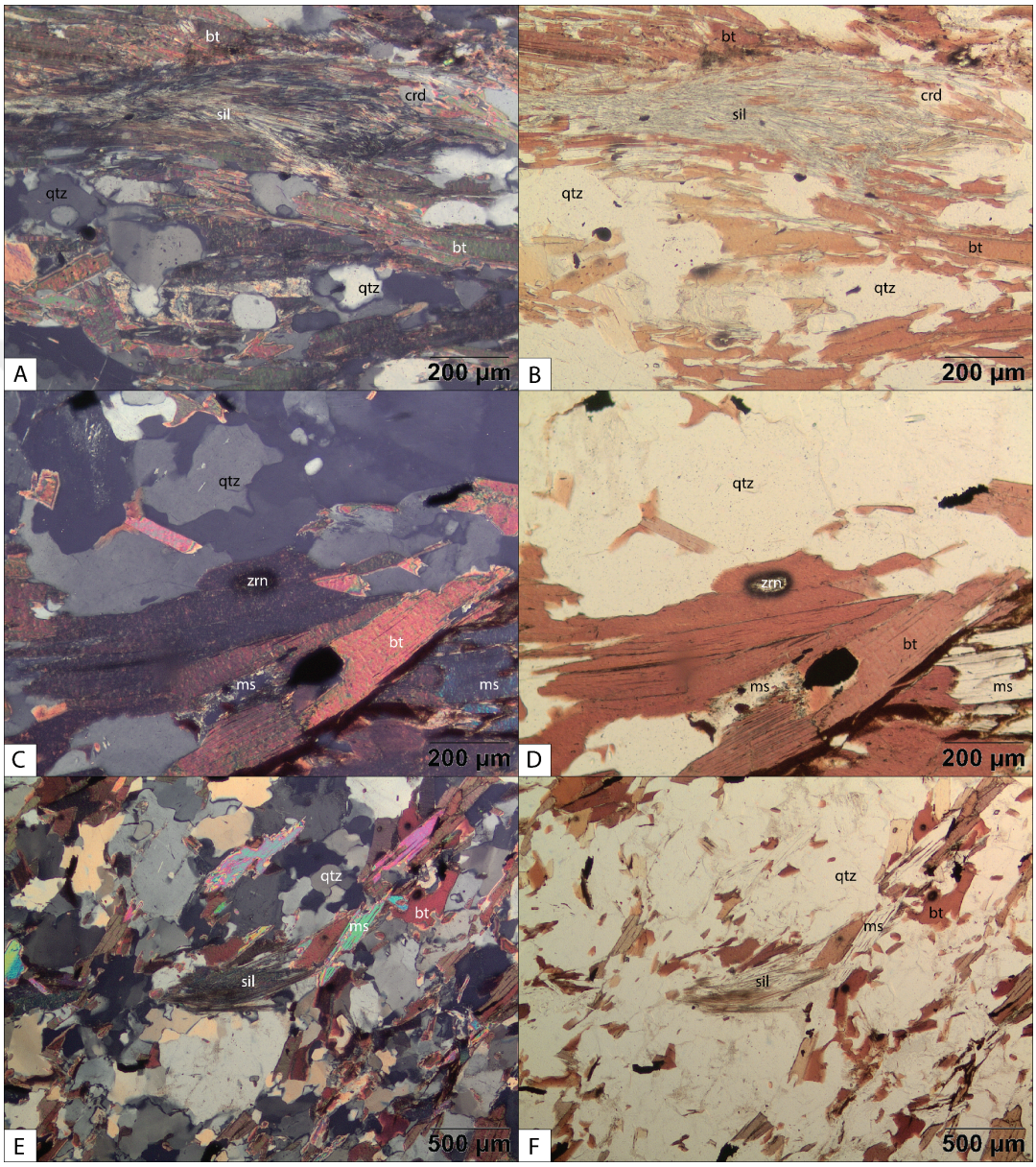


Figure 3.1. Photomicrographs of paragneisses within the Söğüt Metamorphics showing some mineralogical and textural features: (A-XPL, B-PPL) sil-bt-crd of deformed paragneiss, foliation is defined by the orientation of bt and sil, (C-XPL, D-PPL) qtz-bt-ms-zrn of paragneiss; note the decay halo of zircon inside the biotite, (E-XPL, F-PPL) sil-qtz-bt-ms of paragneiss.

Foliation is defined by the preferred orientation of biotite and muscovite in seldom samples, though in most cases, it could not be identified (Figure 3.2).

Apatite is generally observed as euhedral grains. Hexagonal basal sections are present. Apatite is colorless under PPL with high relief and displays a weak birefringence with 1st order interference colors under XPL. Parallel extinction is diagnostic. Furthermore, garnet was observed, colorless under PPL with high-relief while showing complete extinction under XPL, and the characteristic fractures are well-developed.

Finally, although porphyroclasts of feldspar minerals were observed in hand specimens of the orthogneisses, such grains were not observed under thin section, probably due to their large grain sizes.

3.1.2 Amphibolites

Amphibolites were divided into two groups with respect to their grain sizes as, i) coarse-grained amphibolite (grain sizes vary between 0.5-1.5 mm), and ii) fine-grained biotite-amphibolite (grain sizes vary between 0.15-0.25). Although there are seldom larger grains in the coarse-grained group, both groups appear to be equigranular. Apart from hornblende and plagioclase, which characterizes the dominant mineralogy in both groups (50-50%), quartz, sphene, epidote, chlorite, calcite, muscovite, and zircon were observed as well. Furthermore, in addition to the minerals listed above, biotite was found within the mineral assemblage of fine-grained amphibolites. Although foliation is defined on fine-grained amphibolite group with the preferred orientation of biotite grains, foliation could not be observed on the coarse-grained amphibolites under thin section. Foliation on coarse-grained amphibolite samples was also seldomly observable in the field. Finally, a thin section was prepared carefully, encompassing a migmatitic band. This section revealed that these bands are dominantly composed of altered plagioclase with minor amounts of hornblende, confirming the field observations.

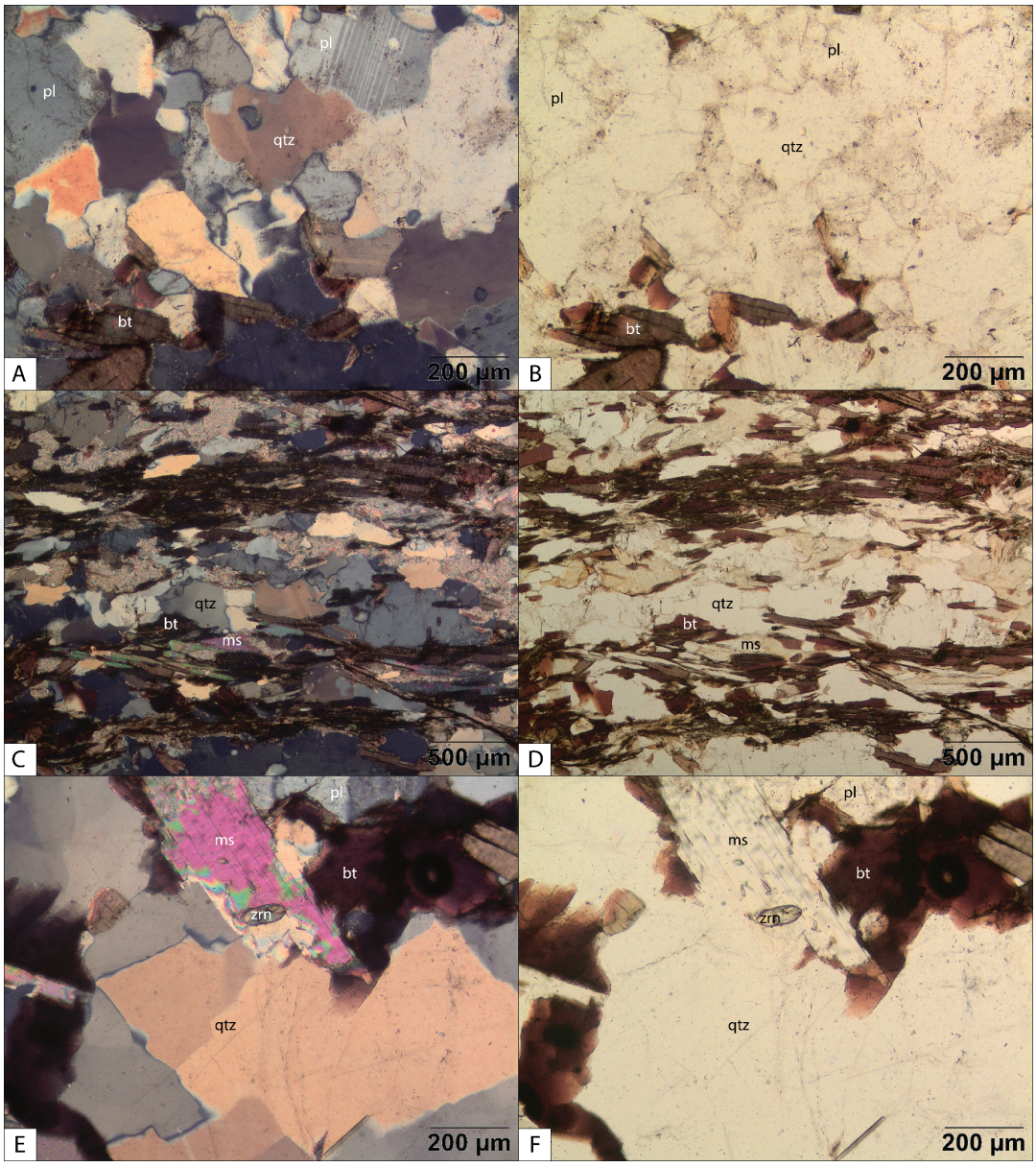


Figure 3.2. Photomicrographs of orthogneisses within the Söğüt Metamorphics showing some mineralogical and textural features: (A-XPL, B-PPL) qtz-pl-bt of orthogneiss, note the polysynthetic twinning of pl, (C-XPL, D-PPL) qtz-bt-ms of orthogneiss, foliation is defined by the orientation of bt and ms, (E-XPL, F-PPL) qtz-pl-bt-euhedral zrn of orthogneiss.

Hornblende (Figure 3.3, 3.4- A, B, E, F) has high relief, and it is pleochroic with tones of brown to dark green under PPL; brown color is observed in the cores of the grains, whereas green colors dominate in the rims, possibly linked to metamorphism.

Hornblende shows moderate birefringence with 2nd orders of interference colors under XPL. One directional cleavage is common and well-defined, though two-directional cleavage is also found in the basal sections. In longitudinal sections, hornblende displays oblique extinction, whereas on basal sections, extinction is symmetrical to cleavage traces. Rare zircons were distinguished within the cracks of hornblende, which are colorless under PPL and pale brown under XPL, coupled with a characteristic decay halo and high relief while displaying parallel extinction (Figure 3.4-E).

Plagioclase is mostly altered and partly replaced by sericite and/or calcite (Figure 3.4-C, D), yet seldom unaltered grains show tapering, pericline, and polysynthetic twinning. These differential twinning types were defined with the parallel wedge-shaped twin laminae for tapering twins, well-developed planar parallel twin laminae for polysynthetic twins, and two sets of well-developed planar parallel twin laminae with an orthogonal orientation for pericline twins (Figure 3.3-A, B). Plagioclase is colorless with low relief and displays 1st order interference colors under XPL, yet the replacement minerals, sericite and/or calcite shows distinctly higher birefringence with 4th order interference colors under XPL. Inclined extinction, which is typical for plagioclase, is well observed. Some parts of the plagioclase grains are extensively altered, and the replacing minerals for these parts are not distinguishable.

Biotite is unique to the fine-grained amphibolite group. Biotite has moderate relief, and it is pleochroic with distinctive dark brown to red colors under PPL and displays 2nd to 3rd orders of interference colors while having mottled extinction. Furthermore, biotite displays well-developed cleavages. As mentioned before, the preferred orientation of biotite grains, defines the foliation of fine-grained amphibolites (Figure 3.3-C, D).

Extensive amount of sphene (Figure 3.3-A, B, E, F; 3.4-A, B, F) was observed in varying sizes, some of which are turned to leucoxene. Sphene is slightly pleochroic with pale brown colors under PPL, whereas it looks brown under XPL, reflecting the characteristic masked nature of the sphene. A high relief is apparent, and both

diamond-shaped euhedral and anhedral shapes are present with seldom fractures. Well-developed cleavage is observed, where extinction is defined symmetrical to the cleavage traces. Euhedral and subhedral Ti- and Fe- oxide opaque minerals were observed in relation with hornblende, plagioclase, and sphene grains. Especially for sphene, dark red-black colored opaque minerals were observed at their cores.

Epidote, chlorite, and muscovite were observed in relationship with hornblende and plagioclase grains (Figure 3.3-E, F; 3.4). Epidote is colorless and brownish-green under PPL and XPL, respectively. Consequently, epidote grains have birefringence with 2nd to 3rd orders of interference colors. Although a well-developed cleavage is not apparent, all the distinguished grains are fractured. Chlorite is pale green under PPL and slightly pleochroic, while showing birefringence with anomalous blue and violet interference colors. Epidote (with high relief) and chlorite (with low relief), were observed usually as pairs. On the other hand, rare muscovite grains were observed, defined colorless under PPL while showing birefringence with 3rd order interference colors under XPL. Muscovite is further defined with well-developed cleavages and moderate relief. Epidote, chlorite and muscovite displays parallel extinction.

Quartz, calcite, Ti- and Fe-oxide veins were observed cross-cutting the hornblende-plagiocase dominated assemblages. Vein-filling quartz (Figure 3.3-E, F; 3.4-A, B) are colorless under PPL and display fresh surfaces with 1st order interference colors. They display the characteristic wavy extinction and low relief. On the other hand, calcite veins and calcite replacements observed on plagioclase grains were observed in one sample alone (Figure 3.3-C, D). Calcite is colorless under PPL with moderate relief and has very high birefringence with 4th order interference colors. Well-developed characteristic rhombohedral cleavage is present, where symmetrical extinction is apparent to the traces. Ti- and Fe-oxide veins (red to dark-red colored) and their development within the cracks of hornblende grains are interpreted to be the cause of alteration (Figure 3.3-A, B). For all of these vein types, micro-faults were observed confirming the brittle deformation observed in the outcrops of amphibolites.

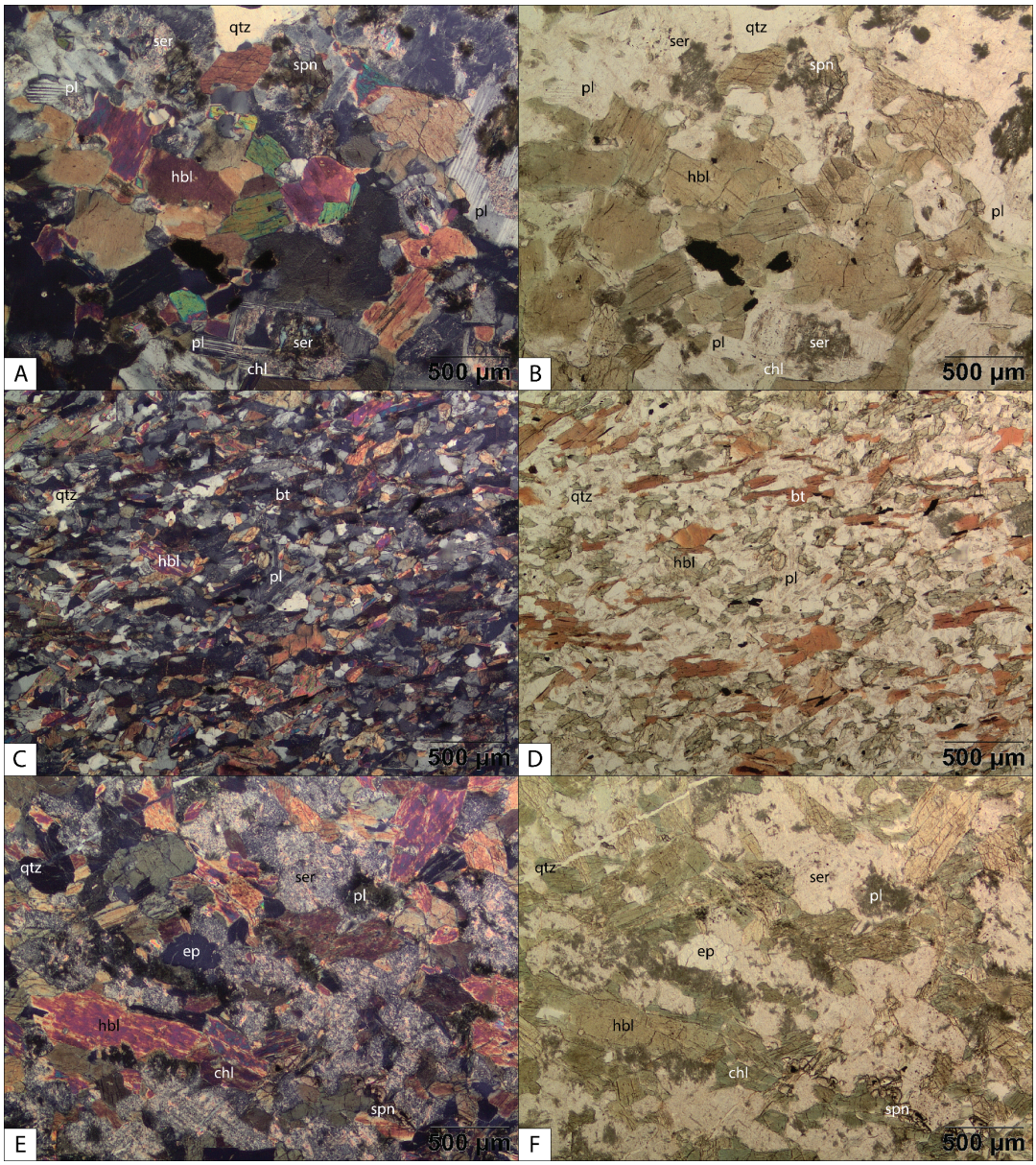


Figure 3.3. Photomicrographs of amphibolites within the Söğüt Metamorphics showing some mineralogical and textural features: (A-XPL, B-PPL; SM20) hbl-pl-spn-qtz-chl-ser of amphibolite, note the pl grain at the center displaying pericline twinning, (C-XPL, D-PPL; SM19) bt-hbl-pl-qtz of fine-grained amphibolite, (E-XPL, F-PPL; SM12) hbl-pl-spn-chl-ser-ep with cross cutting qtz-vein, micro faults can be observed cutting through the qtz-vein.

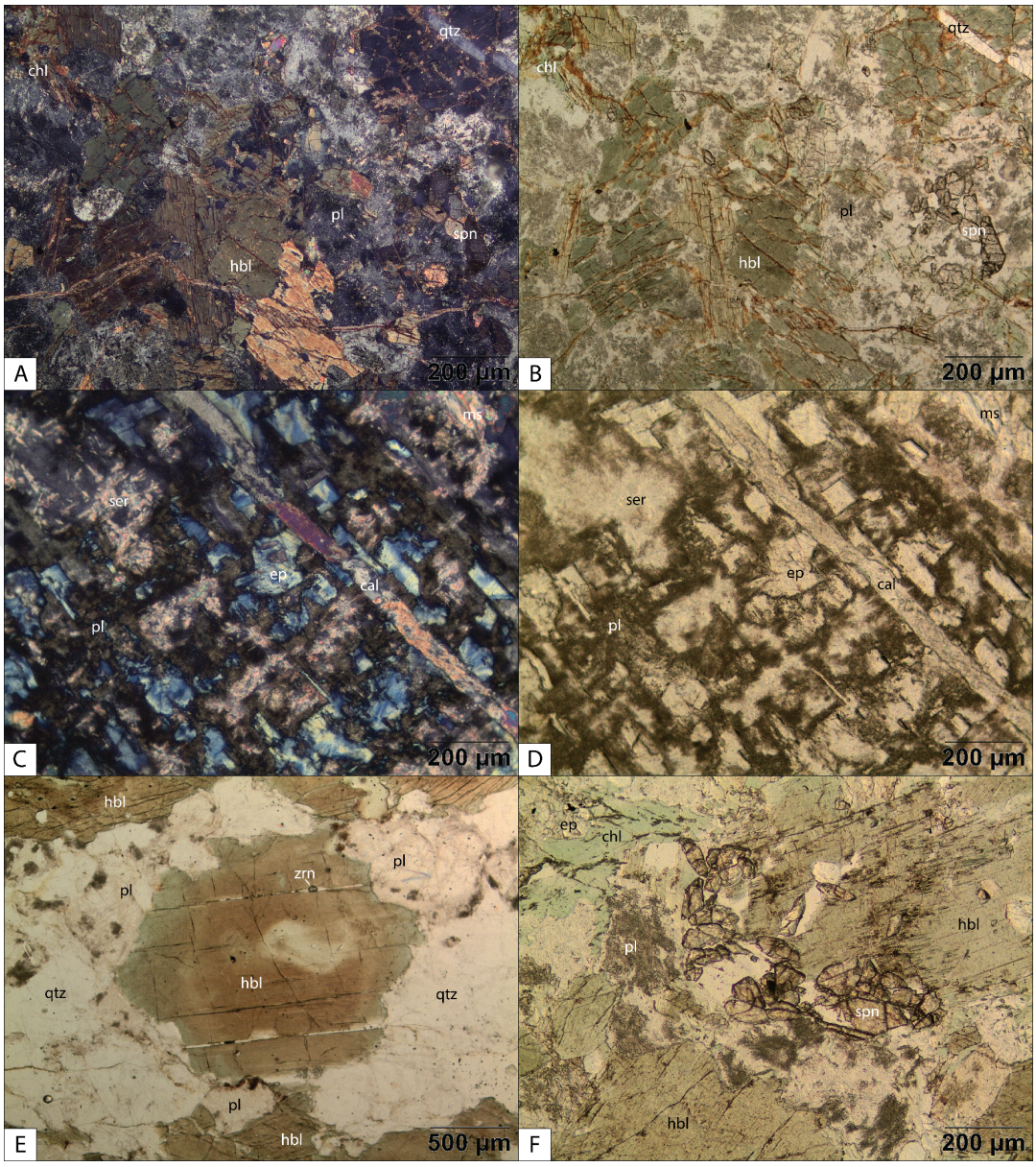


Figure 3.4. Photomicrographs of amphibolites within the Söğüt Metamorphics showing some mineralogical and textural features: (A-XPL, B-PPL; SM10) hbl-pl-spn-chl of amphibolite with cross-cutting quartz vein, note the cross-cutting oxide vein at the lower part, as well as the oxidization at the cracks of the horblende grains, (C-XPL, D-PPL; SM6) ep and pl replaced partly by sericite, note the cross-cutting cal vein, (E-PPL; SM20) Euhedral hbl, showing the metamorphic growth with brown core and green rim, as well as pl-qtz, zrn is present at the crack of the hornlende grain, (F-PPL, SM5) hbl-pl-ep-chl with spn of coarse-grained amphibolite.

3.2 Sarıcakaya Granitoid

Sarıcakaya Granitoid consists of granite, diorite, quartz-diorite, grano-diorite, and crosscuts the basement rocks. A limited number of thin sections were prepared from fresh quartz-diorite.

Quartz-diorite is composed of quartz, biotite, hornblende, plagioclases, and muscovite. Although this lithology is characterized by an equigranular texture, some rare large hornblende grains were observed as well. Zircon, apatite, and opaque minerals were observed as accessory phases. Hornblende was observed having both euhedral and anhedral shapes. Euhedral ones exhibit diamond-shaped outlines, showing simple twinning (Figure 3.5-A, B). Well-developed polysynthetic twinning was observed on plagioclase, with tapering twins on seldom grains. Quartz grains show undulose extinction as well as kinking and deformation lamellae on seldom grains, indicating deformation signatures (Figure 3.5-C, D). Although samples are generally alteration free, sericite was observed in minor amounts as the alteration products of plagioclase.

3.3 Tozman Metaophiolite

Tozman Metaophiolite were observed to the north of Çayköy village and to the west of Tozman village as a discontinues tectonic slice. At its boundaries, the leuco- and melano-gabbros are in faulted contact with orthogneiss. The mafic members of the unit are leuco- and melano-gabbros, whereas the ultramafic member is serpentinized peridotite. All the thin-sections show that samples are relatively fresh and free of alteration except plagioclases showing minor-alteration signatures, confirming the field observations.

It was observed that both mafic and ultramafic rocks display well-developed cumulate texture (Figure 3.6-A-D). In melanogabbro sections, dominating minerals are olivine, orthopyroxene and clinopyroxene, with a lesser amount of plagioclase.

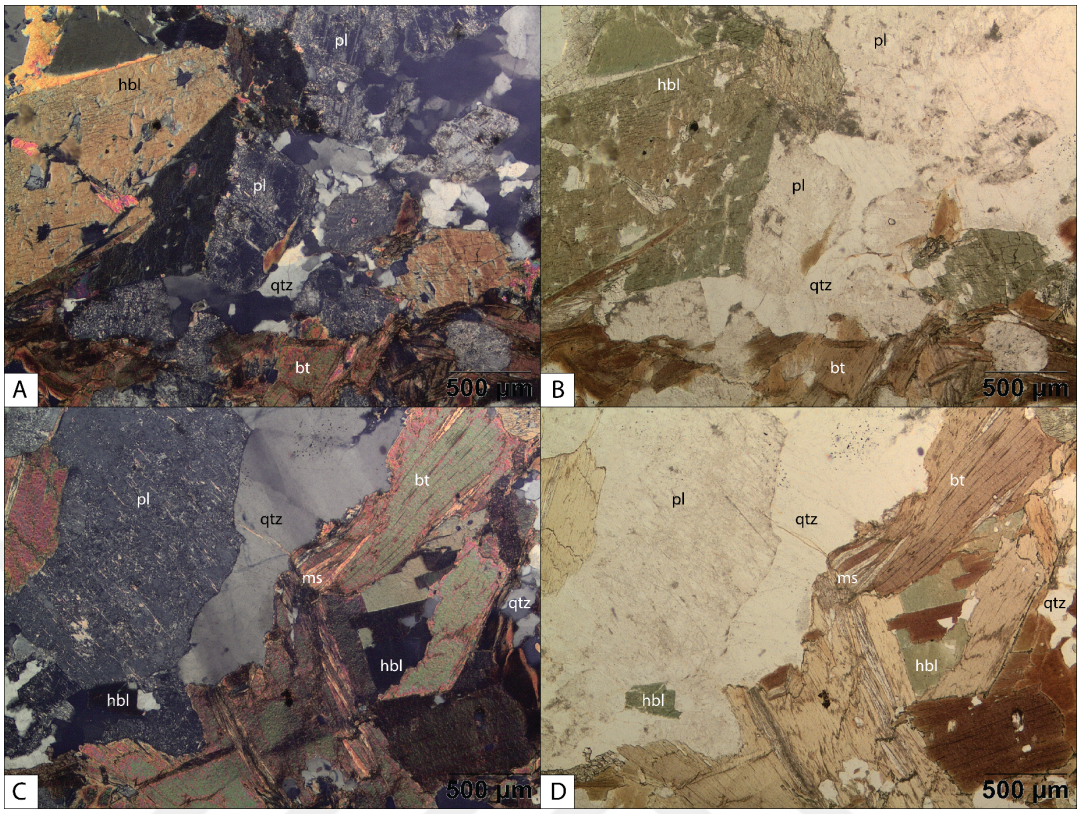


Figure 3.5. Photomicrographs of diorite of Sarıcakaya Granitoid showing some mineralogical and textural features: (A-XPL, B-PPL) hbl-bt-qtz-pl of diorite, simple twinning on hbl, polysynthetic twinning on pl, (C-XPL, D-PPL) qtz-pl-hbl-bt-ms of diorite, note the undulose extinction and kinking on the qtz grain in the center.

Clinopyroxene defines the intercumulus phase, whereas olivine, plagioclase, and orthopyroxene minerals were observed in the cumulus phase. In the leucogabbros, abundant amount of plagioclase minerals was observed, with lesser amount of olivine and pyroxene. The cumulate texture is consistent also with leucogabbros, displaying similar cumulus and intercumulus phases, yet, in samples located to the east of the tectonic slice, hornblende was additionally observed. The peridotitic samples display a mineral paragenesis completely made up of olivine and pyroxene, again with cumulate texture.

One thin section was carefully prepared from the leuco- and melano-gabbro transition, which displayed a change in the fractionating assemblage from an olivine+pyroxene-dominant mineralogy to a plagioclase-rich mineral assemblage.

Olivine grains are typically fractured with high relief. They are colorless under PPL, while displaying 2nd to 3rd order interference colors under XPL, and parallel extinction. In addition, almost all the olivine grains are serpentinized with varying intensity at the cracks and rims, displaying pale-green colors under PPL whereas displaying 1st order interference colors under XPL (Figure 3.5-C, D).

Pyroxene minerals were distinguished from each other mainly with the oblique extinction of clinopyroxene and parallel extinction of orthopyroxene, as well as the birefringence of clinopyroxene with 2nd to 3rd order of interference colors and 1st order interference colors for orthopyroxenes. It should also be noted that both clino- and ortho-pyroxenes displays well-developed cleavages. Furthermore, on several orthopyroxene grains, well developed polysynthetic twins and exsolution lamellae, and on several clinopyroxene grains, simple twins were observed (Figure 3.5-E, F).

Plagioclase display well-developed polysynthetic twinning on several grains, however, with thick twin laminaes. Although plagioclase is mostly free of alteration, a few grains were found to be altered.

Hornblende that was observed in the leuco-gabbro samples shows similar properties to those of the amphibolites. Although a slightly preferred orientation of hornblende grains was observed, it is not penetrative, yet, the cumulate texture was still observable.

In addition to the serpentinized olivine grains, serpentinite veins were observed under the thin sections of all rock types of this group. These veins are further classified as chrysotile veins, colorless under PPL, while having birefringence with 1st order interference colors under XPL and complimented with a distinctive fibrous texture (Figure 3.5-E, F).

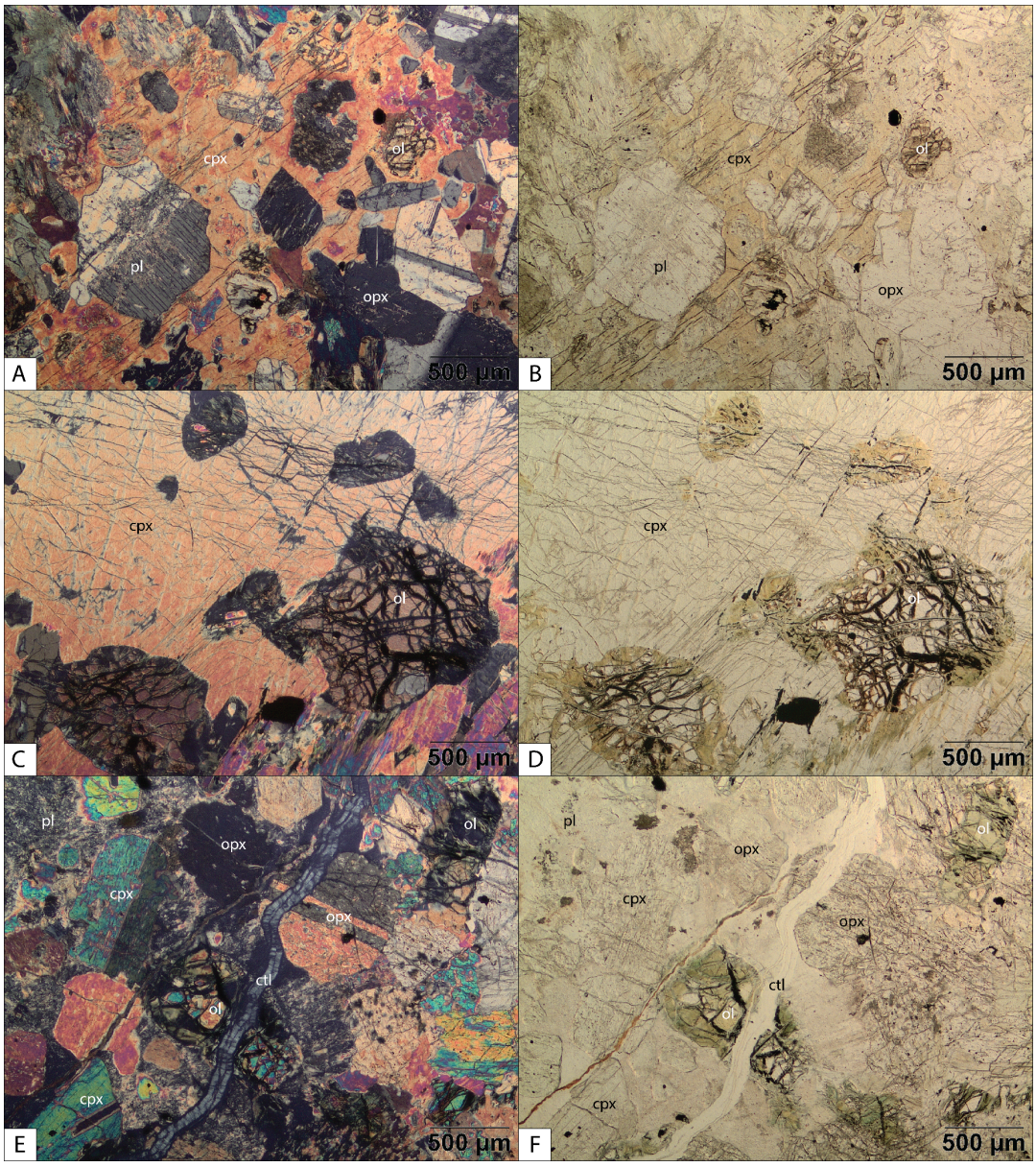


Figure 3.6. Photomicrographs of cumulate-gabbros of Tozman Metaophiolite showing some mineralogical and textural features: (A-XPL, B-PPL) altered pl, partially serpentinized ol, opx (cumulate phase), cpx (intercumulus phase), note the polysynthetic and simple twinning of pl, (C-XPL, D-PPL) Partially serpentinized ol (cumulate phase), cpx (intercumulus phase), (E-XPL, F-PPL) pl-cpx-opx-ol with cross-cutting ctl vein.

CHAPTER 4

GEOCHRONOLOGY AND GEOCHEMISTRY

The field and petrographic properties of the amphibolites are singular, yet as it would be introduced in this chapter; incohesive to fine- and coarse-grained varieties, two different types exist with respect to formation ages and geochemical characteristics. This chapter includes the presentation and interpretation of geochemical analyses in two parts; (1) U-Pb geochronology applied on selected 6 amphibolite samples, and (2) whole-rock geochemistry on 14 amphibolite samples distributed throughout the study area.

4.1 U-Pb Geochronology

Zircon mineral was selected for geochronological analysis due to its resistance to alteration and metamorphism. U is highly compatible with zircon, whereas Pb is not during magmatic crystallization. Based on this, the Pb that is present today can be assumed to be only due to the decay of U, therefore making zircon a reliable geochronometer (Schoene, 2014). During a metamorphic overprint or magmatic overgrowth, core-rim structures may form on zircon grains, where, original crystallization ratios are sustained at the cores, while the measurements from the rims indicating the ages of the secondary event. The application of LA-MC-ICP-MS U-Pb measurements on zircons separated from amphibolite samples, both enabled the determination of original crystallization ages of the protoliths, as well the determination of secondary events during their post-magmatic evolution.

Six amphibolite samples were chosen for zircon age determination considering their field distribution and their chemical affinities. Although a very high amount of sphene was observed during petrographic analysis, zircon was observed seldomly. Therefore, the separation was conducted from large amounts of samples from each

location. The separated zircons show rounded (very low amount) to euhedral shapes with unzoned to oscillatory and laminated zoning (Figure 4.1; Appendix A). In total 245 spots were analyzed from 231 zircons (Appendix B).

Samples SM6, SM19, and SM20 yielded Middle Carboniferous 336 ± 2.0 Ma, 327. 61 ± 0.99 Ma and 328.7 ± 1.6 Ma $^{206}Pb/^{238}U$ weighted mean ages, respectively (Figure 4.2, 4.3). SM6 (coarse-grained amphibolite) is from the north of Sarıcakaya town, whereas SM19 (fine-grained amphibolite) and SM20 (coarse-grained amphibolite) are from the north-east of Tozman village. On the other hand, samples SM12, SM21, and SM29 yielded Middle Ordovician 460.8 ± 2.6 Ma, 465.4 ± 2.0 Ma and 459.8 ± 2.9 Ma $^{206}Pb/^{238}U$ weighted mean ages respectively (Figure 4.2, 4.18). SM12 and SM29 (both coarse-grained amphibolites) are from the north of Mihalgazi town, and SM21 (coarse-grained amphibolite) is from the east of Çayköy village. Furthermore, measurements from the rims of the zircon from samples SM12 and SM 21 yielded Middle Carboniferous 332.3 ± 5.3 Ma and 339 ± 14 Ma $^{206}Pb/^{238}U$ weighted mean ages, respectively.

The Th/U ratios of all measurements are larger than 0.1 (including the measurements from the rims). This indicates that the calculated ages with the measurements from the cores represent crystallization ages of the protoliths of the amphibolites and the calculated ages with the measurements from the rims of zircons represents a magmatic overgrowth. Therefore, it is interpreted that the rims of the zircons from SM12 and SM21 formed due to the Middle Carboniferous basic magmatism.

The Middle Ordovician and Middle Carboniferous ages are presented in red and blue, respectively, and measurements with Pb-loss are presented in gray in the $^{207}Pb/^{235}U$ vs. $^{206}Pb/^{238}U$ diagrams presented below (Figure 4.2-4.4).

It was further determined that these samples further correlated with respect to their geochemical characteristics. Throughout the rest of the thesis, “Type 1” and “Type 2” notations are used, which encompass the Middle Ordovician and Middle Carboniferous samples, respectively.

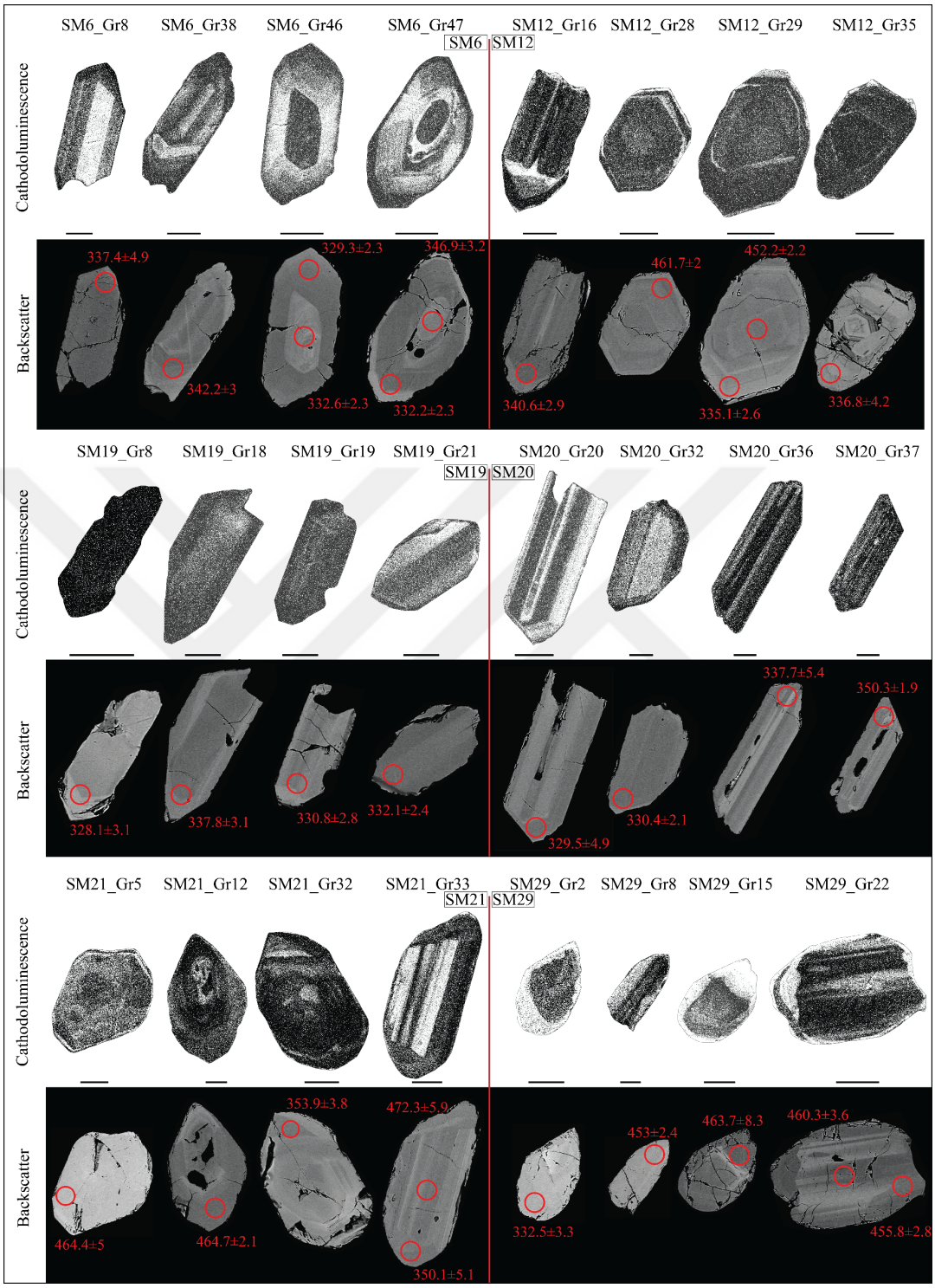


Figure 4.1. Selected zircon grains from analyzed samples. Each scale bar indicates 50 μm, whereas the spot marks of the analysis locations are 12 μm in diameter. Presented ages are $^{206}Pb/^{238}U$ ages of each spot.

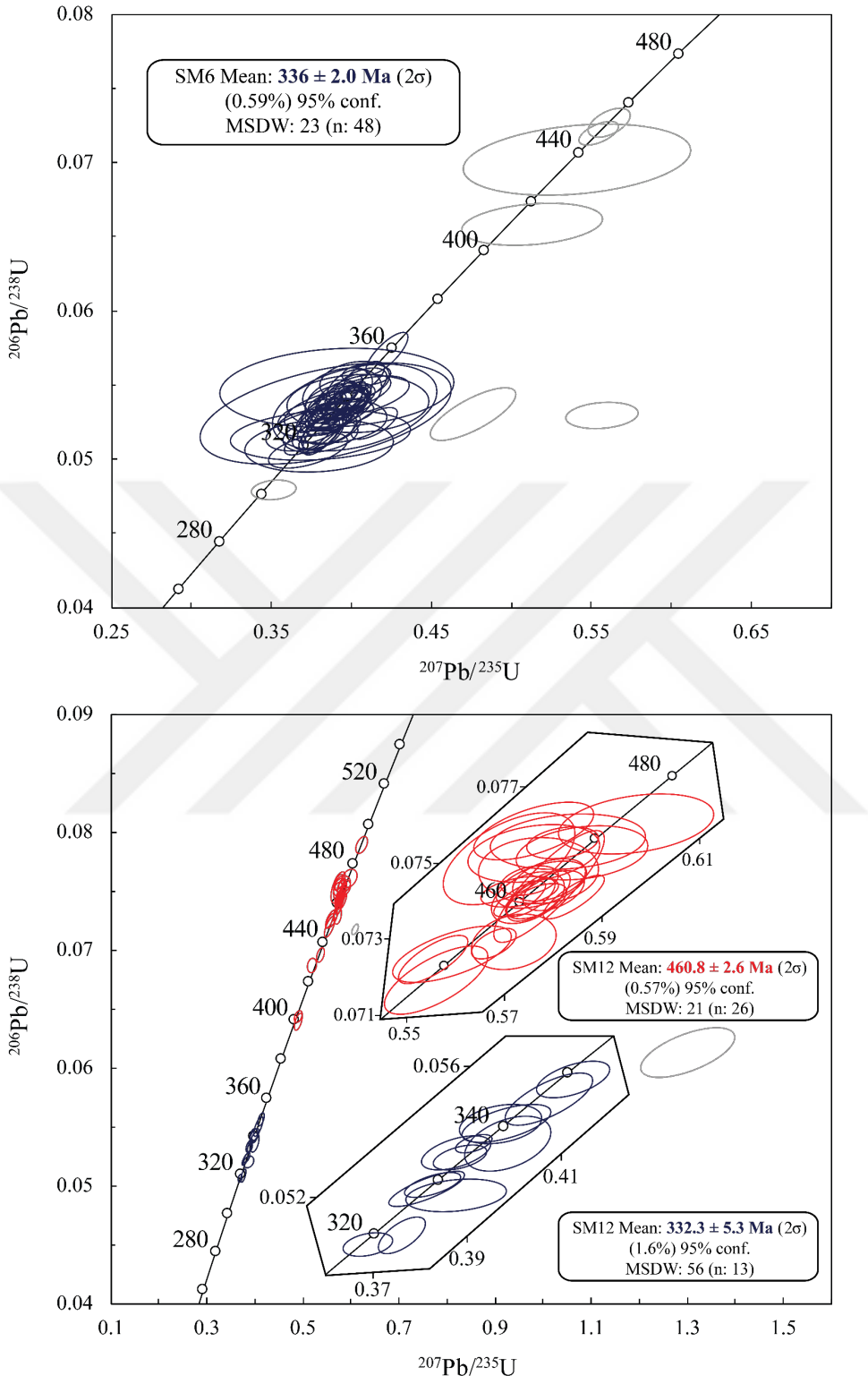


Figure 4.2. $^{207}Pb/^{235}U$ vs. $^{206}Pb/^{238}U$ diagram and weighted mean ages of SM6 (Type 2) and SM12 (Type 1) samples.

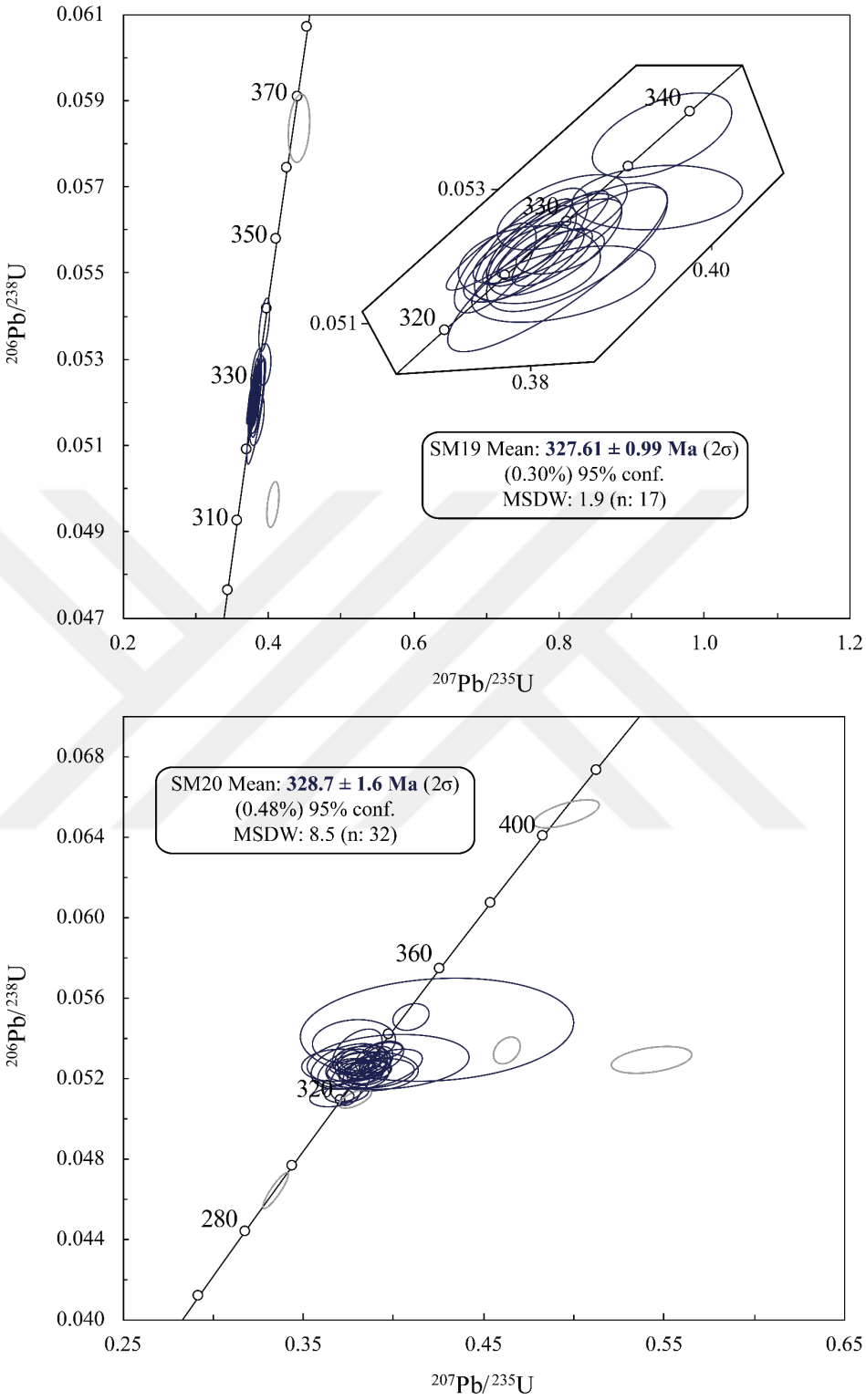


Figure 4.3. $^{207}Pb/^{235}U$ vs. $^{206}Pb/^{238}U$ diagram and weighted mean ages of SM19 and SM20 (Both are Type 2) samples.

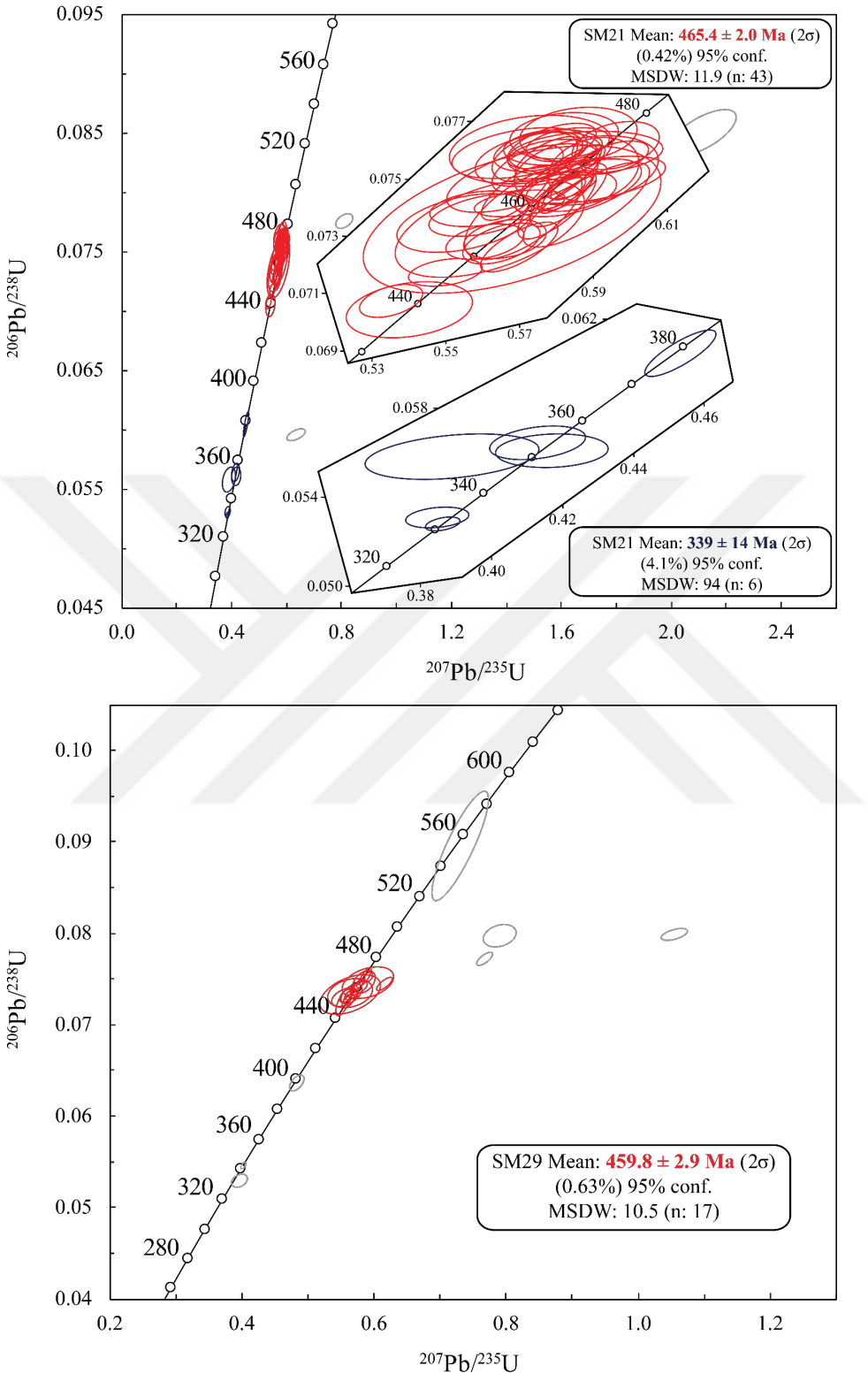


Figure 4.4. $^{207}Pb/^{235}U$ vs. $^{206}Pb/^{238}U$ diagram and weighted mean ages of SM21 and SM29 (Both are Type 1) samples.

4.2 Whole-Rock Geochemistry

On metamorphic rocks, with the effect of increasing pressure and temperature, and via solid-state reactions between existent minerals, mineral chemistry is affected, and new mineral paragenesis forms (also defining the metamorphic facies). During metamorphism, the bulk chemical composition is assumed to stay the same with the protoliths chemistry with the exception of volatiles and/or mobile elements, whereas the composition of immobile elements remains unaffected (e.g. Wood et al., 1976). Therefore, whole-rock geochemistry analyses (Table 4.1) conducted on amphibolites enables the determination/interpretation of the original composition and tectonic setting of the protoliths, the role of fractional crystallization, source characteristics, metasomatic modifications, with the use of Harker, tectonomagmatic discrimination, and multi-element diagrams combined with ratio diagrams. Analyses were conducted with ICP-AES and ICP-MS with the application of necessary QA/QC protocols (Chapter 1), which provides high precision and accuracy on the whole-rock geochemistry of the samples.

4.2.1 Assessment of Post-Crystallization Events

In order to assess the effects of post-crystallization events (i.e. metamorphism and alteration), the distribution of mobile and immobile elements should be evaluated carefully in order to determine their potential use for further examinations (Wood et al., 1976; Floyd and Winchester, 1978). Igneous lithologies influenced by low-grade alteration and/or metamorphism may be affected in terms of mobile element content, such as Large Ion Lithophile Elements (LILEs) (e.g. K, Rb, Sr, Ca, Ba) (e.g. Hart et al., 1974). On the other hand, High Field Strength Elements (HFSEs) (e.g. Th, Nb, Ce, Zr, Hf, Ti) and Rare Earth Elements (REEs) shows immobility under such conditions (e.g. Floyd and Winchester, 1978). It should also be noted that HFSEs and REEs may sustain their immobility through amphibolite facies conditions,

extending up to eclogite facies conditions (e.g. John et al., 2004; Sayit et al., 2016; Marroni et al., 2020).

Table 4.1. Whole-rock geochemical analysis results of amphibolites within Söğüt Metamorphics, including the major oxides (wt. %), trace elements (ppm) and REEs (ppm).

Sample ID	SM4	SM5	SM6	SM7	SM8	SM10	SM11
Location	293056 N 4436468 E	292723 N 4436468 E	296980 N 4438984 E	296844 N 4439492 E	293075 N 4436333 E	292783 N 4436796 E	292674 N 4437073 E
SiO_2	45.2	49.9	50.1	43.5	52	49.1	53.4
Al_2O_3	16.35	17	16.65	19.75	13.55	17.25	14
Fe_2O_3	14.6	8.11	8.34	12	8.04	9.55	6.62
CaO	7.92	9.49	10.8	9.88	6.77	9.75	9.7
MgO	5.25	5.95	6.48	5.71	10.9	5.44	7.49
Na_2O	3.44	3.18	2.6	1.26	2.39	3.48	2.65
K_2O	1.1	1.47	1.78	1.58	1.08	1.22	1.9
Cr_2O_3	0.002	0.005	0.027	0.004	0.108	0.008	0.069
TiO_2	2.62	0.96	0.6	1.91	0.28	1.35	0.67
MnO	0.2	0.14	0.15	0.18	0.12	0.15	0.13
P_2O_5	0.53	0.22	0.07	0.23	0.08	0.44	0.14
SrO	0.04	0.04	0.02	0.03	0.02	0.04	0.01
BaO	0.08	0.04	0.04	0.02	0.03	0.05	0.03
LOI	2.31	2.08	2.62	2.68	3.29	3.05	1.87
Total	99.64	98.59	100.28	98.73	98.66	100.88	98.68
Ba	784	416	371	219	276	509	303
Ce	96.3	38.5	12.5	24.2	20.2	86.5	24.5
Cr	10	30	180	10	820	40	660
Cs	0.59	0.93	1.6	1.29	0.57	0.88	0.82
Dy	9.93	4.5	1.67	5.69	2.63	8.21	3.09
Er	5.47	2.54	1.06	3.42	1.51	4.43	1.71
Eu	2.38	1.29	0.75	1.5	0.79	1.92	0.8
Ga	24.8	20.1	15	21	14	19.8	14.2
Gd	9.92	4.07	1.64	6.47	2.57	8.63	2.86
Hf	5.8	1.9	1.1	1.9	1	2.1	2.4
Ho	1.93	0.75	0.38	1.14	0.52	1.59	0.56
La	43.5	18	7.3	8.6	9.9	38.9	11.4
Lu	0.75	0.33	0.21	0.44	0.25	0.64	0.22
Nb	34.9	15.6	2.3	10.7	2.7	21.6	9
Nd	50.7	19.4	6.4	20.3	10.8	44.8	13.4
Pr	12.45	4.76	1.4	3.79	2.38	10.4	3.33
Rb	27.4	58.5	62	94.1	29.3	33.9	89.9
Sm	11.1	4.35	1.49	6.14	2.53	9.98	3.07
Sn	4	2	2	3	2	3	2
Sr	400	421	249	323	223	428	216
Ta	1.6	0.6	<0.1	<0.1	<0.1	0.4	0.5
Tb	1.54	0.64	0.31	0.98	0.41	1.33	0.43
Th	0.76	0.9	0.81	0.65	0.95	0.83	1.4
Tm	0.79	0.33	0.14	0.45	0.2	0.66	0.2
U	0.27	0.46	0.63	0.47	0.62	0.45	0.42
V	696	248	182	322	148	302	197
Y	55.2	24.7	9.1	29.1	13.6	43.9	18
Yb	4.77	2.31	1.04	2.66	1.45	3.86	1.64
Zr	224	68	38	44	42	69	94

Table 4.1. Cont'd.

Sample ID	SM12	SM19	SM20	SM21a	SM21b	SM24	SM29
Location	292790 N 4437624 E	288062 N 4439530 E	288428 N 4439152 E	283952 N 4435714 E	283952 N 4435714 E	282534 N 4436255 E	293043 N 4436422 E
SiO_2	51	56.1	53	47.6	50	46.9	46.2
Al_2O_3	15.75	16.55	16.55	16.05	16.25	12.9	17.25
Fe_2O_3	8.93	9.15	8.21	14.6	10.75	12.25	10.4
CaO	9.78	7.12	9.36	9.73	9.23	10.4	10.45
MgO	6.84	4.43	5.56	5.9	4.65	9.28	6.42
Na_2O	3.05	1.9	2.37	2.85	3.28	0.66	2.4
K_2O	1.51	1.27	0.93	1.3	1.3	2.02	1.5
Cr_2O_3	0.012	0.011	0.035	0.008	0.006	0.057	0.018
TiO_2	0.96	0.73	0.81	1.41	1.04	1.88	1.66
MnO	0.15	0.19	0.15	0.19	0.18	0.2	0.16
P_2O_5	0.15	0.1	0.12	0.23	0.6	0.2	0.47
SrO	0.02	0.01	0.02	0.03	0.04	<0.01	0.04
BaO	0.02	0.02	0.02	0.03	0.03	0.02	0.05
LOI	2.1	1.59	1.7	1.04	1.47	1.92	2.36
Total	100.27	99.17	98.84	100.97	98.83	98.69	99.38
Ba	220	228	171.5	277	305	136.5	499
Ce	31.9	22	23.6	43.8	75.5	23.7	63.3
Cr	90	70	270	50	40	450	130
Cs	0.49	2.74	1.63	0.6	0.59	2.53	1.2
Dy	3.02	2.86	2.63	4.95	9.31	4	5.22
Er	1.71	1.67	1.65	2.85	4.92	2.1	3.09
Eu	1.05	0.89	1.06	1.69	1.74	1.45	1.89
Ga	16.7	17.9	18.1	19.8	22.3	19.5	20.8
Gd	3.39	2.88	3.11	5.4	9.1	4.71	6.42
Hf	2.1	1.9	2.2	2.6	3	3	2.4
Ho	0.61	0.57	0.53	0.96	1.67	0.72	1.08
La	16.7	9.6	12.6	21.7	33	10.4	28.9
Lu	0.27	0.29	0.27	0.44	0.6	0.23	0.45
Nb	17.7	5.2	5.2	23.3	29.2	13.9	19.4
Nd	15.4	11.3	11.9	21.7	40.2	15.8	31.6
Pr	3.6	2.62	2.68	4.97	10.25	3.11	7.36
Rb	70.4	55.3	31.5	36.1	38.6	103	38.9
Sm	3.5	2.82	2.7	4.72	10.15	4.32	6.63
Sn	3	3	3	3	5	7	2
Sr	274	169	244	300	337	145	459
Ta	0.5	<0.1	<0.1	0.5	1.4	<0.1	0.1
Tb	0.52	0.47	0.42	0.83	1.51	0.71	0.93
Th	2.67	3.39	1.26	1.02	3.38	0.81	0.74
Tm	0.26	0.26	0.23	0.42	0.67	0.26	0.44
U	1.29	1.48	0.71	0.59	3.2	0.3	0.39
V	237	220	214	292	298	233	335
Y	16.9	15.9	14.1	24.9	49.5	18.9	28.2
Yb	1.72	1.63	1.45	2.52	4.09	1.42	2.73
Zr	82	64	78	107	101	114	77

For a throughout examination, the amphibolite samples are divided into two groups (namely Type 1 and Type 2) based on multi-element schematics (Figure 4.5), which will be explained in detail in further sub-chapters.

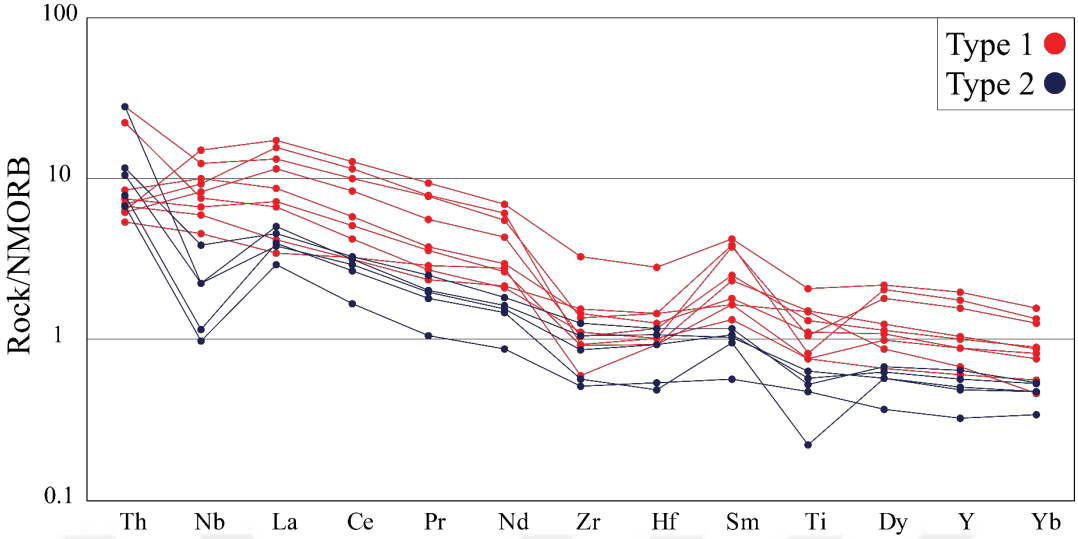


Figure 4.5. Multi-element spider diagram schematics of amphibolites from Söğüt Metamorphics, normalized with respect to N-MORB, values from Sun and McDonough, 1989.

Loss on Ignition (LOI) values of Type 1 and Type 2 varies between 1.04 and 3.05, and 1.7 and 3.29, respectively. This is consistent with amphibolite metamorphism and later-stage weathering overprint as displayed by petrographic observations under thin section (Chapter 3). Bivariate diagrams of trace elements Nb were used to demonstrate these effects (Figure 4.6). Mobilization is prone to take place in either of the events, and it was observed that LILEs (e.g. Ba, Sr), is affected partially. Although Ba and Sr values are scattered for Type 2 samples, they still demonstrate a slight trend for Type 1 samples. On the other hand, mobile elements such as Rb, K, Ca yields well developed linear trends for Type 1 samples when plotted against MgO. Therefore, although so-called mobile elements, such as LILEs, appear to be somewhat immobile (for Type 1 samples), these elements were used in further examinations carefully. Furthermore, High Field Strength Elements (HFSE) and Rare Earth Elements (REE) (e.g. La, Zr, Hf, Yb, Sm) shows well-developed linear trends against Nb and revealing their immobility under post-crystallization events, therefore, used for further examinations extensively.

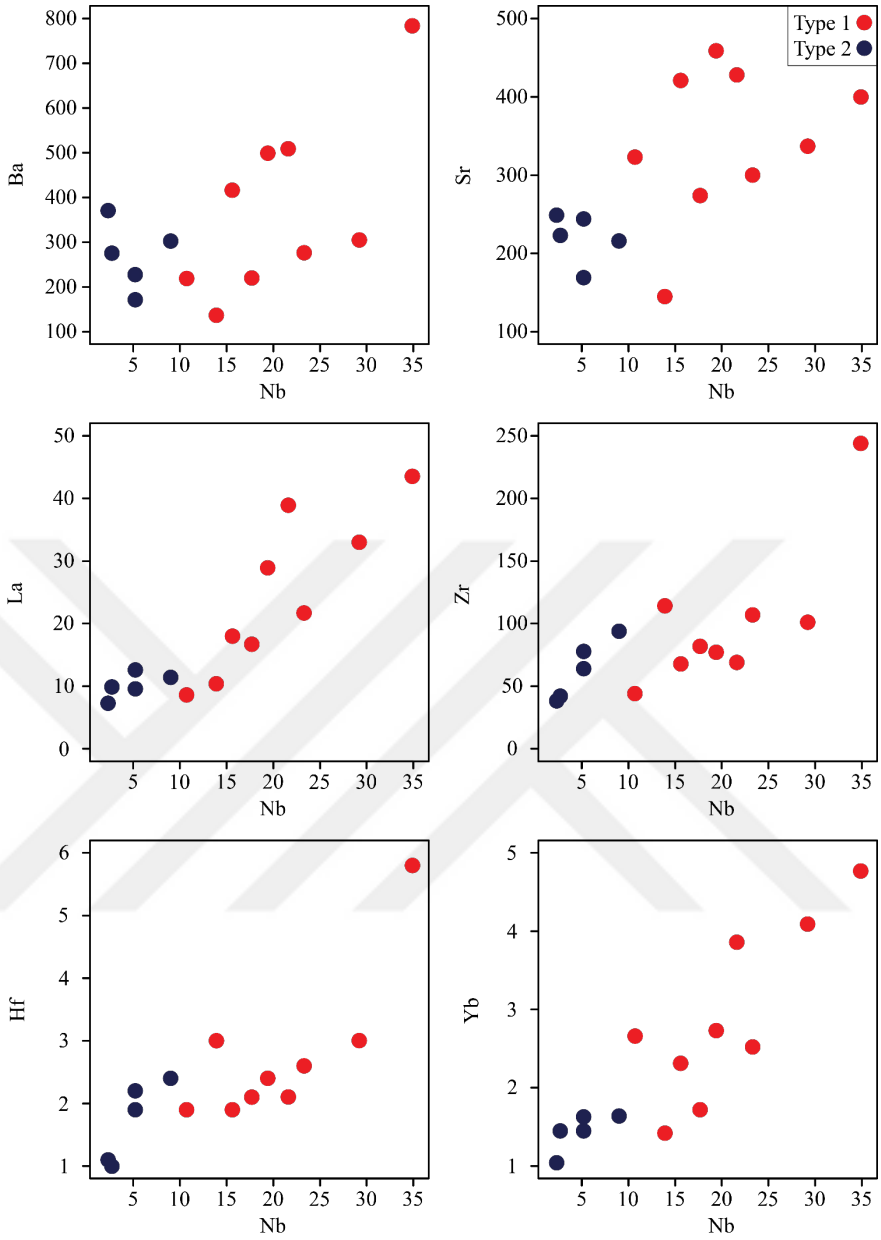


Figure 4.6. Distribution of selected trace elements against Nb, values are in ppm.

4.2.2 Classification

The classification of the analyzed amphibolite samples was conducted with Nb/Y vs. Zr/Ti diagram (Figure 4.7). The TAS (Total Alkali-Silica) diagram was disregarded to minimize the effect of mobile elements, K, Na, and Si. Instead, the Nb/Y vs. Zr/Ti diagram was chosen since it is entirely based on immobile elements, which may, in

turn, provide more reliable classification. The plot shows that the amphibolites have both alkaline to subalkaline characters with their protoliths ranging from basalt to basaltic andesitic rocks. Nb/Y ratios vary between 0.37 and 1.05 for Type 1, and 0.2 and 0.5 for Type 2. Type 2 samples are completely subalkaline, whereas Type 1 samples are observed to display a wider range, including subalkaline, transitional and alkaline varieties. Again, with the same reasoning, the AFM diagram was not preferred for the characterization of subalkaline samples at this stage, due to the use of mobile elements in the diagram. Further classification will be provided in the petrogenesis sub-chapter.

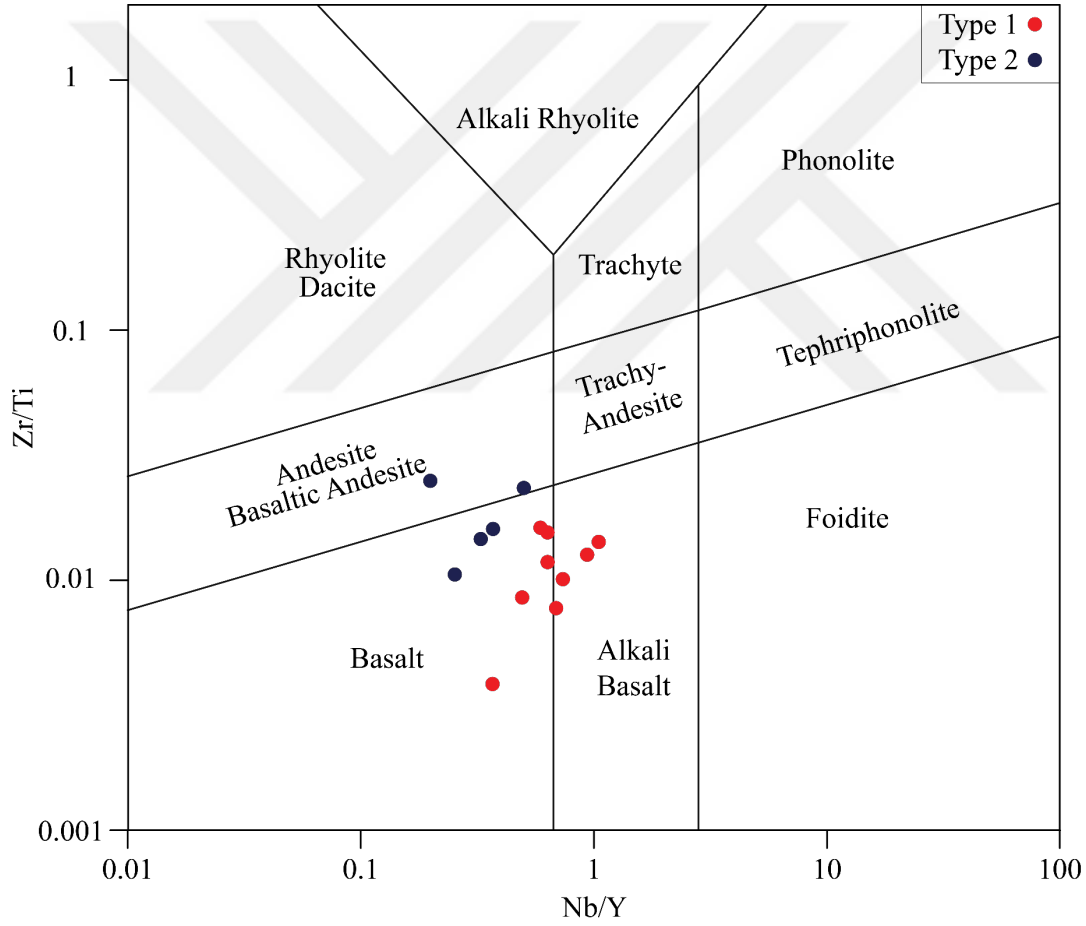


Figure 4.7. Nb/Y vs. Zr/Ti classification diagram (Winchester and Floyd, 1977 modified by Pearce, 1996) for the amphibolites of the Söğüt Metamorphics.

4.2.3 Elemental Variations

4.2.3.1 Major Oxides

The compositional variation of major oxides (wt. %) shows a wide range of distribution for Type 1 amphibolites. Except for K_2O and CaO, Type 2 amphibolites shows a narrow range. The SiO_2 content varies between 43.5-51 for Type 1, whereas Type 2 displays higher values, with 50.1-56.1. Al_2O_3 content varies between 12.9-19.75 for Type 1 samples. Type 2 samples, on the other hand, exhibit a narrower range with 13.55-16.65; thus, they are entirely confined within the interval defined by Type 1 samples. Fe_2O_3 content varies between 8.11-14.6 for Type 1 samples, and 6.62-9.15 for Type 2 samples. Although an overlap is present, Type 1 samples display higher values in general. CaO (Type 1: 7.92-10.45, Type 2: 6.77-10.8), MgO (Type 1: 4.65-9.28; Type 2: 4.43-10.9) and K_2O (Type 1: 1.1-2.02; Type 2: 0.93-1.9) content variations largely overlap for the two amphibolite types. Na_2O content varies with a wide range for Type 1 (0.66-3.48), whereas with a narrow range for Type 2 (1.9-2.65). Although an overlap is present, Type 1 samples reach up to higher values with respect to Type 2 samples. TiO_2 (Type 1: 0.96-2.62; Type 2: 0.28-0.81) and P_2O_5 (Type 1: 0.15-0.6; Type 2: 0.07-0.14) variations show that, both TiO_2 and P_2O_5 values are completely lower (with a narrow range) for Type 2 samples with respect to Type 1 samples (with a wide range) (Figure 4.8).

4.2.3.2 Trace Elements

Trace element distributions were examined in two respect; i) variations against MgO and ii) multi-element patterns. Similar to their distributions in the major oxide variations, Type 1 amphibolites exhibit a broad range of distribution on trace elements compositions, whereas Type 2 amphibolites show a wide range of distribution on only seldom elements such as Cr and Rb (Figure 4.9).

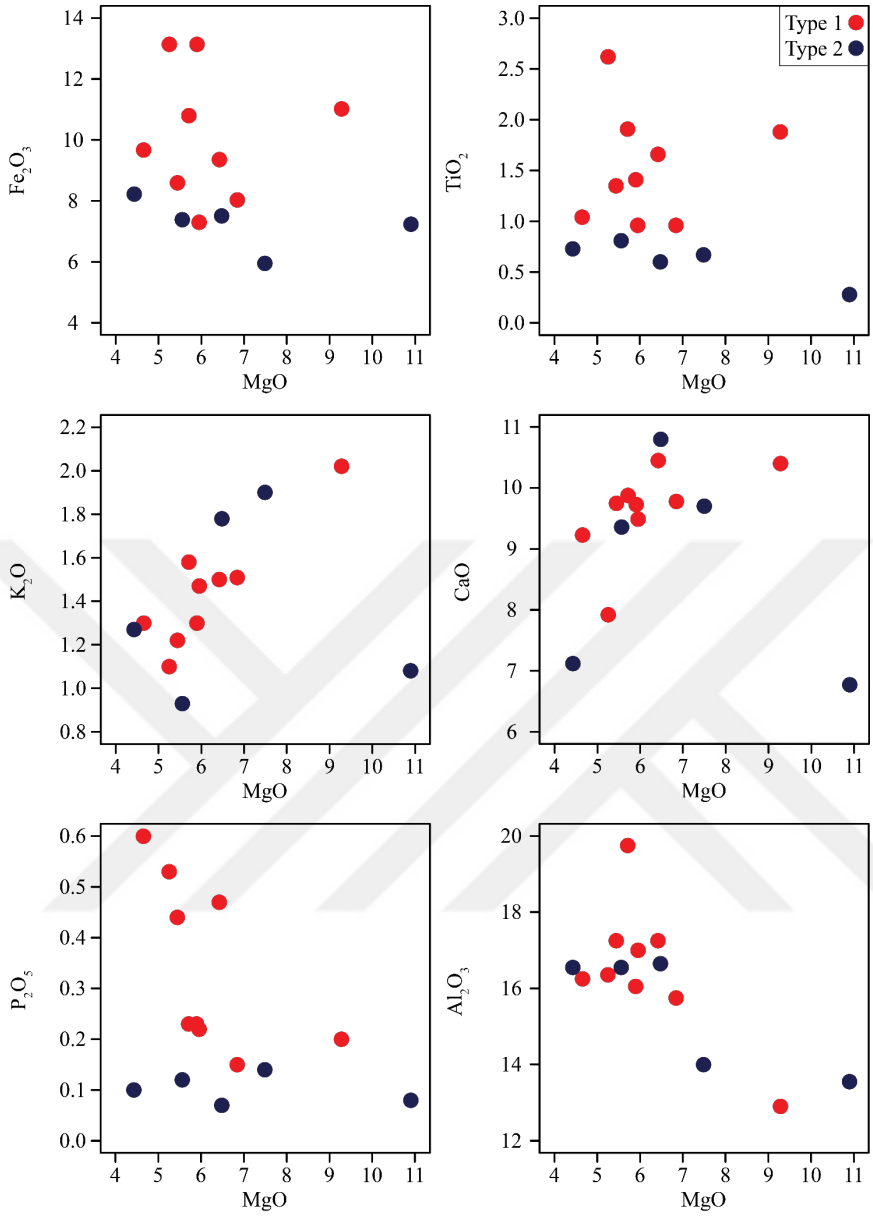


Figure 4.8. Distribution of major-oxides against MgO, values are in wt. %.

Ba values vary between 136.5-784 ppm for Type 1, and 171.5-371 ppm for Type 2, and Sr values vary between 145-459 ppm for Type 1 and 169-249 ppm for Type 2. For both elements, the narrow range of Type 2 samples is completely enveloped within the wide range of Type 1 samples, which also ranges up to higher values. On the other hand, Cr values range between 10-450 ppm for Type 1, and between 70-820 ppm for Type 2. Although an overlap is seen, Cr values range wider and up to higher values for Type 2 samples, compared to Type 1 samples. Rb values vary

between 27.4-103 ppm for Type 1 and 29.3-89.9 ppm for Type 2, although some overlap is present within a similar range, Type 1 values range up to higher values. La and Yb values range between 8.6-43.5 and 1.42-4.77 ppm respectively for Type 1; 7.3-12.6 and 1.04-1.64 ppm respectively for Type 2. For these elements, although a slight overlap is present at lower values, Type 1 samples exhibit a wider range and reach higher values. Sm values vary between 3.5-11.1 ppm for Type 1, and between lower values of 1.49-3.07 ppm for Type 2, without any overlap (Figure 4.9).

Further examination was conducted with multi-element diagrams normalized to Normal Mid-Ocean Ridge Basalt (N-MORB), and Chondrite. In order to remove the effect of post-magmatic events on mobile elements, only HFSEs and REEs were used.

N-MORB-normalized spider diagrams (Figure 4.10) yield that all Type 1 and partially Type 2 amphibolites are enriched with respect to N-MORB in highly incompatible elements (i.e. Th, Nb, and La), former having higher enrichment compared to latter. Yet, two samples of Type 2 have Nb contents plotting near unity, implying their N-MORB-like abundances in these elements. Considering Zr, Hf, Ti, Y, and HREEs, Type 1 samples show a wide range, including both enriched and depleted varieties, whereas all are enriched in Sm relative to N-MORB. On the other hand, Type 2 samples are all depleted in Ti, Y, and Heavy-REEs (HREEs), while showing depletion/unity for Zr, Hf, and Sm compared to N-MORB. The two groups are mainly separated from each other by the strong Nb negative anomaly present in Type 2 samples, which is largely lacking in Type 1 samples (Only two samples shows Nb depletion, which remains weaker when compared with Type 2) (Th/Nb: 0.02-0.15 for Type 1; 0.16-0.65 for Type 2). Negative anomaly in Zr and Hf is observed on all Type 1 samples (Nd/Zr: 0.14-0.65; Sm/Hf: 1.44-4.75), with the exception of one sample, whereas for Type 2 samples (Nd/Zr: 0.14-0.26; Sm/Hf: 1.23-2.53), this anomaly occurs only slightly, yet one sample shows a strong signature. Furthermore, a negative Ti anomaly exists for all the Type 2 samples, but this situation occurs for

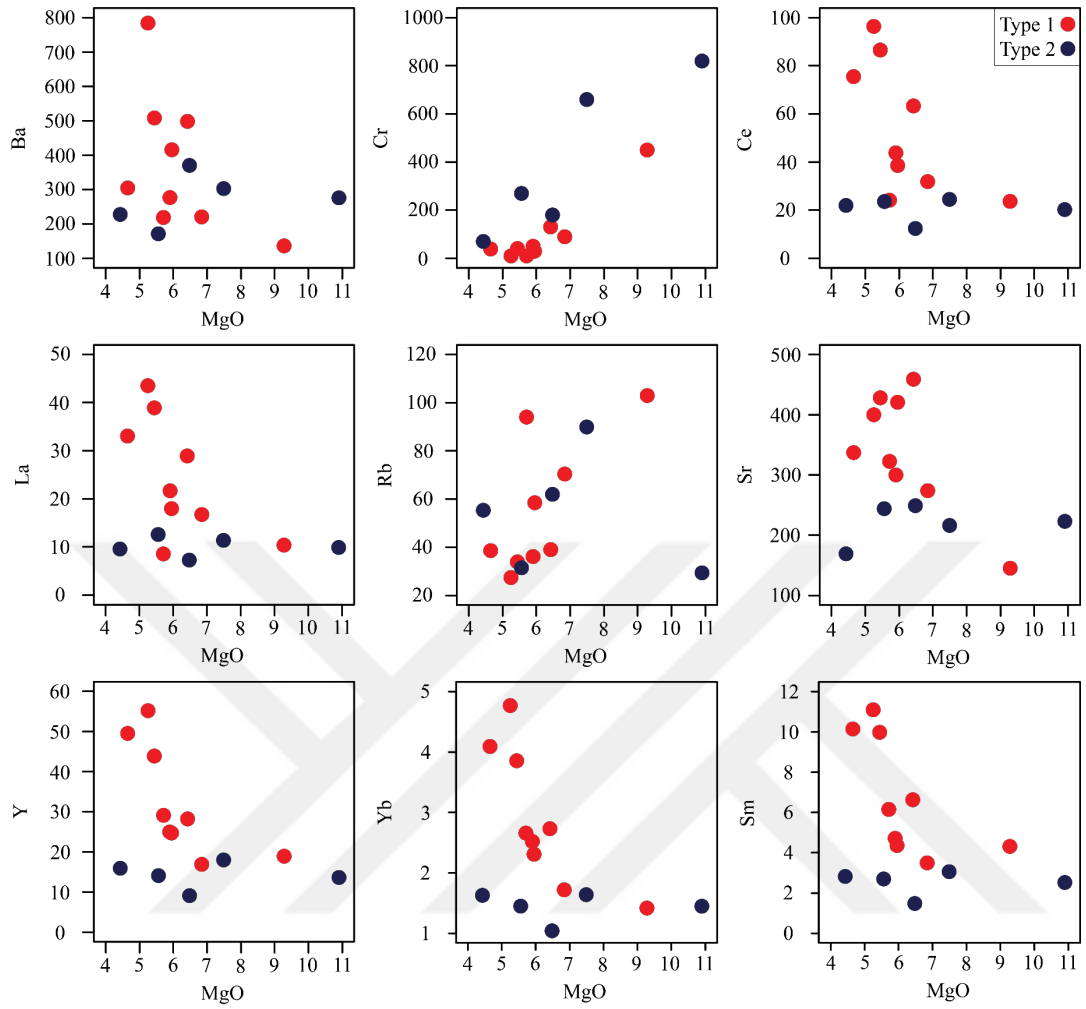


Figure 4.9. Distribution of selected trace elements against MgO. Trace element values are in ppm, MgO values are in wt. %.

only three samples in Type 1 ($[Sm/Ti]_N$: 0.88-3.76 for Type 1; 0.96-3.48 for Type 2; "N" denotes N-MORB-normalized). When compared with average N-MORB, E-MORB (Enriched Mid-Ocean Ridge Basalts) and OIB (Ocean Island Basalts) values (Sun and McDonough, 1989), it is seen that Type 1 samples are variable in terms of Th/Nb, being characterized by both higher and lower, whereas all Type 2 samples display higher ratios of Th/Nb (0.05 for N-MORB; 0.07 for E-MORB and 0.08 for OIB). For Nd/Zr and Sm/Hf ratios, Type 1 samples have completely higher values (Nd/Zr: 0.1, 0.12, 0.14 for N-MORB, E-MORB, OIB respectively; and Sm/Hf: 1.28 for N-MORB, E-MORB and OIB). On the other hand, although Type 2 samples also

have completely higher values of Nd/Zr ratios, they have a variety of higher and lower values of Sm/Hf ratios.

Chondrite-normalized REE diagrams (Figure 4.10) shows that both Type 1 and 2 samples are enriched in Light-REEs (LREEs) compared to HREEs with a negative slope on LREEs (Only one sample in Type 1 shows a positive slope in LREEs) and a relatively flat to slightly enriched pattern on HREEs ($[La/Sm]_N$: 0.9-3.16 for Type 1; 2.2-3.16 for Type 2; $[Dy/Yb]_N$: 1.18-1.89 for Type 1; 1.07-1.26 for Type 2; "N" denotes Chondrite-normalized). Negative Eu anomalies are observed in four samples of Type 1, whereas a positive anomaly in the same element is present in two samples of Type 2.

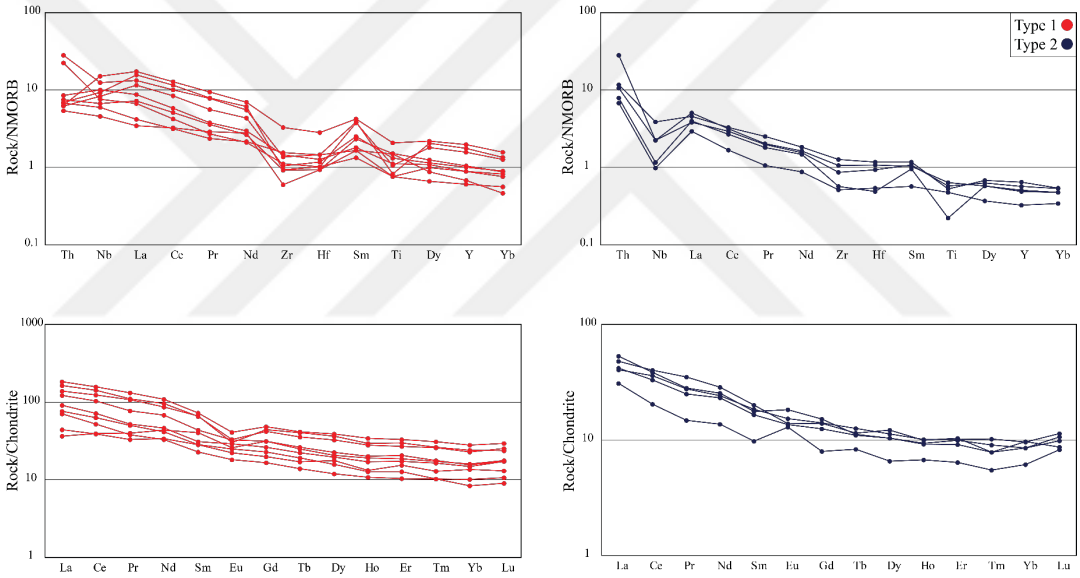


Figure 4.10. Multi-element spider diagram schematics of amphibolites from Söğüt Metamorphics, normalized with respect to N-MORB and Chondrite values from Sun and McDonough, 1989.

4.2.4 Petrogenesis

4.2.4.1 Fractional Crystallization

For the evaluation of the role of fractional crystallization during the formation of the protoliths of the Söğüt Amphibolites, diagrams of MgO vs. major oxides, MgO vs. trace elements, and chondrite-normalized REE diagrams were integrated. Although they are oxides of mobile elements, K_2O and CaO show a decreasing trend towards more evolved compositions (decreasing MgO) for Type 1 samples. Yet, in the rest of the Harker diagrams (Fe_2O_3, TiO_2, P_2O_5, Al_2O_3 against MgO), samples are scattered and do not provide any information for the evaluation of fractional crystallization. Furthermore, when the plots of the Type 2 samples are considered, they are all either scattered (K_2O and CaO against MgO) or have a horizontal linear trend (P_2O_5, and Al_2O_3 against MgO) and a slightly increasing trend with respect to Fe_2O_3 and TiO_2 against MgO, which again does not provide any information for interpreting the role of fractional crystallization (Figure 4.8).

Trace element variations against MgO yield relatively more information for the assessment of fractional crystallization (Figure 4.9). For Type 1 samples, a decreasing trend for Rb and Cr can be observed with the evolving magma, yet an increasing trend of Y, Yb and Sm are present which does not provide information on fractionation. On the other hand, for Type 2 samples, a decreasing trend is observed only for Cr with the evolving magma. For the rest of the trace elements for both types, plots are either scattered, presents a horizontal linear, and/or a slightly linear increasing trend, and therefore, are not suitable for the evaluation of fractional crystallization.

Combining these results, it is apparent that K, Ca, Rb, and Cr for Type 1 samples, and Cr for Type 2 samples may have been modified during the crystallization history of their protoliths. For amphibole, a variety of Partition Coefficient (K_d) values are presented in the literature for K (K_d: 0.6, Philpotts and Ague, 2009; K_d: 1.36, Balpe

and Baker, 1994), Ca (K_d: 2.95, Higuchi and Nagasawa, 1969), and Rb (K_d: 0.29, Winter, 2014; K_d: 1.9, Villemant et al., 1981) with differentiating compositions for basalt, basaltic andesites, basanites, alkali basalts. Although the fractional crystallization of amphibole is possible considering these elements, a confirming schematic should also be observed in the REE diagram. For basaltic compositions, amphibole has K_d>1 for all the REEs expect for La, Ce, and Nd, and higher values of Middle-REEs (MREE) compared to LREEs and HREEs (Philpotts and Ague, 2009; Rollinson, 1993). For Type 1 samples, this pattern is not provided, as both MREE and HREEs have a flat pattern. Therefore, it is concluded that fractional crystallization of amphibole is not effective for Type 1 samples. On the other hand, for the fractional crystallization of plagioclase, on some of the Type 1 samples (relatively more evolved samples of this type with lower MgO wt. % values), a strong Eu (K_d: 1.5, Winter, 2014) negative anomaly was observed. Eu negative or positive anomaly indicates removal or accumulation of plagioclase, respectively (Winter, 2014). Considering also the trend defined by Ca, it was concluded that fractional crystallization for plagioclase might be effective for Type 1 samples. On the other hand, a positive Eu anomaly is apparent for two samples of Type 2 samples, which indicates that plagioclase is accumulated during the evolution of magma; therefore, fractional crystallization of plagioclase is not effective for Type 2 samples. Finally, the decreasing trend of Cr (K_d: 34 (clinopyroxene); K_d: 10 (orthopyroxene), Arth, 1976) with the evolving magma indicates an essential role for the fractionation of pyroxene for both types.

Considering the points stated above, it is interpreted that during the crystallization of the protoliths of the amphibolites, fractional crystallization of pyroxene was important for both Type 1 and Type 2 samples, while fractional crystallization of plagioclase appears to have played some role for Type 1 samples. The trend observed on K and Rb is attributed to source characteristics, effects of either metasomatism or metamorphism, or alteration products.

4.2.4.2 Source Characteristics

In order to understand the source characteristics of the mantle source of the Söğüt Amphibolites, several diagrams were employed using trace elements ratios. In addition to the Nb/Yb vs. TiO_2/Yb of Pearce (2008) (Figure 4.11); variations of Th/Yb, Th/Nb, and Nd/Zr against Nb/Yb; Th/Nb against La/Nb; and Th/Nb against Nb_N were examined. Comparison of the Söğüt Amphibolites were proceeded in the mentioned plots with several characteristic modern tectonic settings, including Mariana Back-Arc (Pearce et al., 2005), South-Sandwich Arc (Pearce et al., 1995), Aeolian Arc (Calanchi et al., 2002), Greater Antilles Arc (Jolly et al., 2007), Mid-Atlantic Ridge (Niu et al., 2001), Walvis Ridge (Salters and Salci-Kocher, 2010), East-African Rift (Furman et al., 2006), Rio-Grande Rift (Gibson et al., 1993), West Greenland (Larsen et al., 2003), East Greenland (Hanghøj et al., 2003), St. Helena (Kawabata et al., 2011), and Samoa (Jackson et al., 2010) (Figure 4.12, 4.13). For a relative comparison, Primitive Mantle (PM), N-MORB, E-MORB, and OIB values from Sun and McDonough (1989) were also integrated to the diagrams and throughout the discussion.

The Nb/Yb vs. TiO_2/Yb diagram of Pearce (2008) presents the distinction of OIB and MORB related sources, respective melting conditions, and alkalinity affinities with respect to the variations of Nb and Ti. The OIB array is defined with an enriched Ti content (TiO_2/Yb: 2.87 for OIB) compared to the MORB array, which is defined by relatively depleted N-MORB (TiO_2/Yb: 1.27) and E-MORB (TiO_2/Yb: 1). Furthermore, Nb content is also indicative of enrichment from N-MORB (Nb/Yb: 0.76) to E-MORB (Nb/Yb: 3.50) and OIB (Nb/Yb: 22.2), whereas the PM is characterized by Nb/Yb: 1.45. Therefore, where N-MORB represents a depleted mantle source, E-MORB and OIB sources represents enriched mantle sources. Altogether, enrichment with respect to Ti and Nb values indicates an enriched source and/or lower degrees partial melting. On the diagram, the majority of the amphibolites plots on the shallow melting-MORB array around E-MORB, indicating an enriched source for both types of amphibolites within the Söğüt metamorphics,

rather than a depleted N-MORB source. Although all the samples are confined within the MORB array, Type 1 samples have a relatively more enriched source than Type 2 samples. In addition, several Type 1 samples plot closer to OIB, which indicates a variation of enrichment trough Type 1 samples as well.

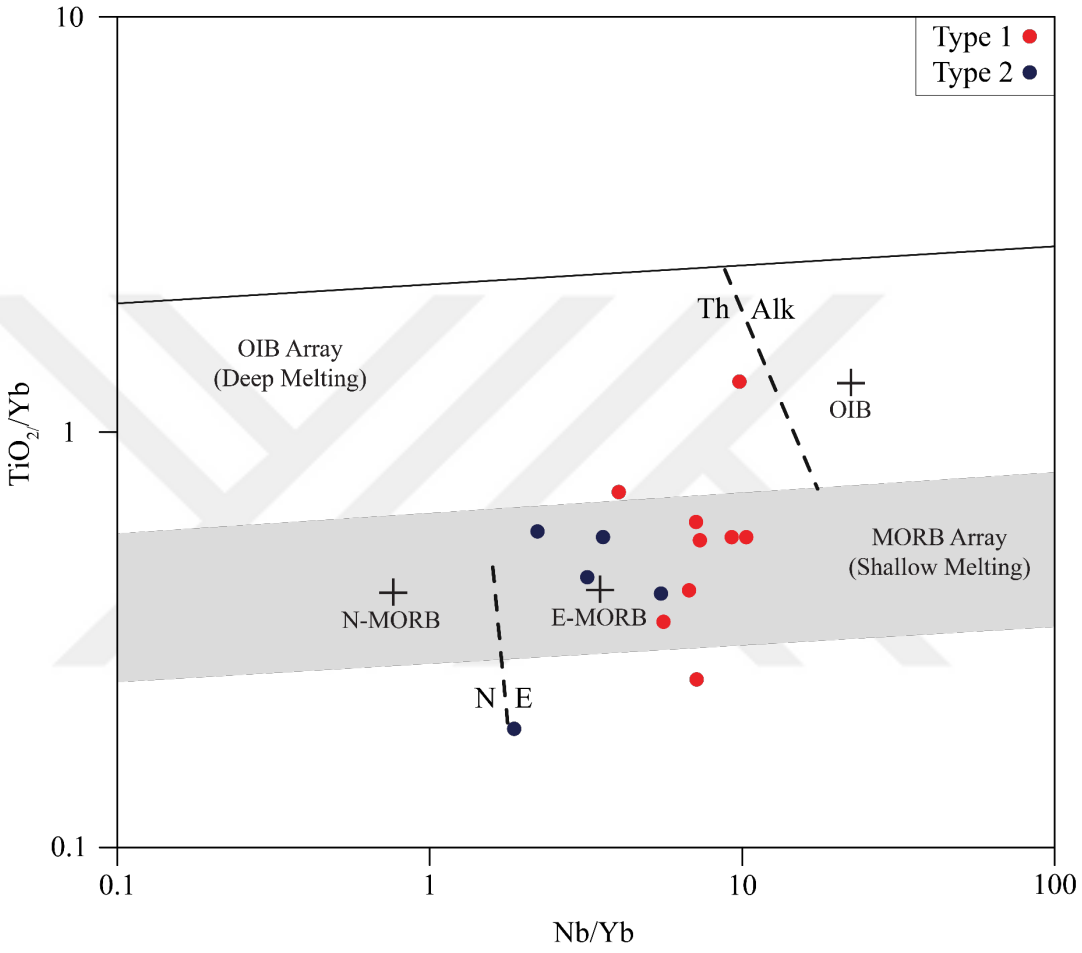


Figure 4.11. Nb/Yb vs. TiO_2/Yb ratio diagram after Pearce (2008).

Nb/Yb vs. Th/Yb ratio diagram (Figure 4.12-A) is useful to understand the mantle source characteristics, particularly for the metasomatic modification by subduction enrichment. Within a subduction zone, enrichment in subduction-mobile elements (e.g. Th, LILE, LREEs) and depletion in subduction-immobile elements (e.g. HFSEs and HREEs) are observed (Pearce et al., 2005). Therefore, while Th is mobilized from the subducting slab via melt phase, which in return is transferred to the mantle wedge, Nb behaves immobile and prefers to stay intact with the subducting slab

creating the respective negative anomaly on multi-element spider diagrams. As a result, the addition of the subduction component will lead to an increasing Th/Yb ratio, while keeping Nb/Yb ratio constant. On the other hand, for the non-subduction melts, represented by the MORB-OIB array, with the enrichment of the source material (from depleted N-MORB to enriched OIB source), Th and Nb act similar, and develops a linear array with an increase in both elements. Therefore, with the use of this diagram, it is made possible to separate the subduction and non-subduction sources from each other, while distinguishing respective enrichment levels on the MORB-OIB array. As it can be seen, subduction-modified sources are clearly distinguished with separation from the MORB-OIB array with higher Th/Yb and lower Nb/Yb ratios, therefore with higher Th/Nb ratios. Varieties of subduction settings can be further classified with continental arcs (e.g. Aeolian Arc) having a higher Th/Yb and Nb/Yb ratios, as compared to oceanic arcs (e.g. South-Sandwich Arc and Greater Antilles Arc) and back-arcs (e.g. Mariana Back-Arc). On the other hand, ridge settings (e.g. Mid-Atlantic Ridge and Walvis Ridge) have lower Th/Yb ratios with increasing Nb/Yb ratios, ranging from depleted sources (N-MORB; Nb/Yb: 0.76) to enriched sources (OIB; Nb/Yb: 22.2). OIB and rift settings (e.g. OIB: St. Helena and Samoa Islands; Rift: Rio-Grande and East-African) show a combined enrichment of Th and Nb. The East-Greenland Dyke Swarm, which consists of tholeiitic picrites, and transitional to alkaline dykes, displays a wide range of Nb composition, plotting in between enriched sources of E-MORB (Nb/Yb: 3.5) and OIB, while alkaline basalts of West Greenland plots on a wider field, showing an enrichment extending from E-MORB to OIB. When the Söğüt Amphibolites are considered, Type 1 samples appear to have a subduction-unmodified source (yet, 2 samples of Type 1 have relatively high Th/Nb ratios, although they do not extend up to the levels of Type 2 samples) with an enrichment level between E-MORB and OIB, showing a wide range of Nb while some samples showing a Th depleted nature with respect to the MORB-OIB array, and mostly confined within West Greenland and East-African Rift fields. On the other hand, Type 2 samples are defined with well-developed Th enrichment with relatively lower Nb concentration of a relatively

depleted (with respect to Type 1) subduction modified melt, and plots on the Greater Antilles Island-Arc and one sample is on Aeolian Continental Arc.

Similarly, the Nb/Yb vs. Th/Nb diagram (Figure 4.12-B) enables the differentiation of subduction and non-subduction melts with the same principles introduced previously. The subduction component is again defined with higher Th/Nb ratios, whereas, subduction in-effective regions are defined with lower Th/Nb ratios. Furthermore, La/Nb vs. Th/Nb diagram (Figure 4.12-C) again enables a similar separation of subduction enrichment with higher Th/Nb and La/Nb ratios from the MORB-OIB environments with lower Th/Nb and La/Nb ratios, La behaves similarly to Th in a subduction zone and is transferred to the wedge. Although relative Th and La enrichment over Nb is a characteristic of arc-related systems, such subduction signatures can be observed in continental intraplate magmas (e.g. Rio-Grande rift) as well, which are associated with the metasomatism of the subcontinental lithospheric mantle (SCLM) (Gibson et al., 1993). On the other hand, for the La/Nb vs. Th/Nb diagram, it is not possible to separate the relatively more enriched OIB (La/Nb: 0.77) characteristics from E-MORB (La/Nb: 0.76). However, this diagram enables the distinction of Type 1 samples from East Greenland, which has relative enrichment with respect to La content (La/Nb: 0.69-3.55). On Nb/Yb vs. Th/Nb diagram, Type 1 samples plots mainly on to relatively enriched East-African Rift and West Greenland fields whereas, Type 2 samples, are confined within the Greater Antilles Arc with one sample again plotted on to the Aeolian Arc field. On La/Nb vs. Th/Nb diagram, Type 1 samples are scattered between N-MORB and more enriched OIB and E-MORB, with lower Th/Nb ratios and a relatively narrow range of La/Nb (0.75-1.80) compared to Type 2 samples (1.27-3.67). Most of the samples are again encompassed within the East African Rift and West Greenland field, while some are showing more enriched source characteristics. Type 2 samples show a repeated relationship with oceanic arc environments such as Greater Antilles and South Sandwich island arcs, except for one sample showing a similarity with Aeolian continental arc. Yet, it should be noted that all the samples are confined within the Rio-Grande rift.

Finally, the Nb_N ("N" denotes N-MORB-normalized) vs. Th/Nb diagram (Figure 4.12-D) again distinguished subduction modified melts from the MORB-OIB array. Except for Rio-Grande rift, high Th/Nb ratios indicate subduction enrichment, whereas, with the increase in Nb_N, the source material is enriched trough the average OIB. With this distinction, Type 1 samples show higher Nb content, compatible with enriched sources, and confined within West Greenland and East Greenland fields, whereas the source for Type 2 samples again shows signatures of subduction enrichment with higher Th/Nb ratios.

Both types of Söğüt Amphibolites shows a depletion of Zr and Hf in their N-MORB-normalized multi-element spider diagrams, Type 1 samples having higher Nd/Zr and Sm/Hf values compared to Type 2 samples (Figure 4.10). In order to assess their relationship with different source environments, Nb/Yb vs. Nd/Zr diagram (Figure 4.13) was plotted. While the sources within the MORB-OIB array are mostly confined within a narrow range of Nd/Zr ratios, sources of the enriched, metasomatized Rio-Grande rift, and West Greenland basalts shows much higher ratios. As it can be seen, while Type 1 samples show much higher ratios than those of the MORB-OIB array, Type 2 samples show Nd/Zr and Nb/Yb ratios ranging within a similar extent of the sources of subduction-related settings. Type 1 samples show a very similar range to the Rio-Grande Rift and West Greenland basalts field (although they differ in their Nb/Yb ratios), both revealing characteristics of a metasomatized SCLM source (Gibson et al., 1993; Larsen et al., 2003), while Type 2 samples are completely confined within the Greater Antilles Island Arc field.

The occurrence of a negative anomaly in Zr-Hf (and to some extent in Ti) is typical for almost all Söğüt Amphibolites. The negative Nb anomaly, on the other hand, is especially prominent in Type 2. It was mentioned previously that a decoupled behavior occurs between LILEs-Th-LREEs and HFSEs-HREEs for both Type 1 and Type 2 amphibolites of Söğüt Metamorphics. The diverse behavior between these groups of elements can be attributed to mantle sources that are metasomatically modified by slab-derived fluids and/or melts.

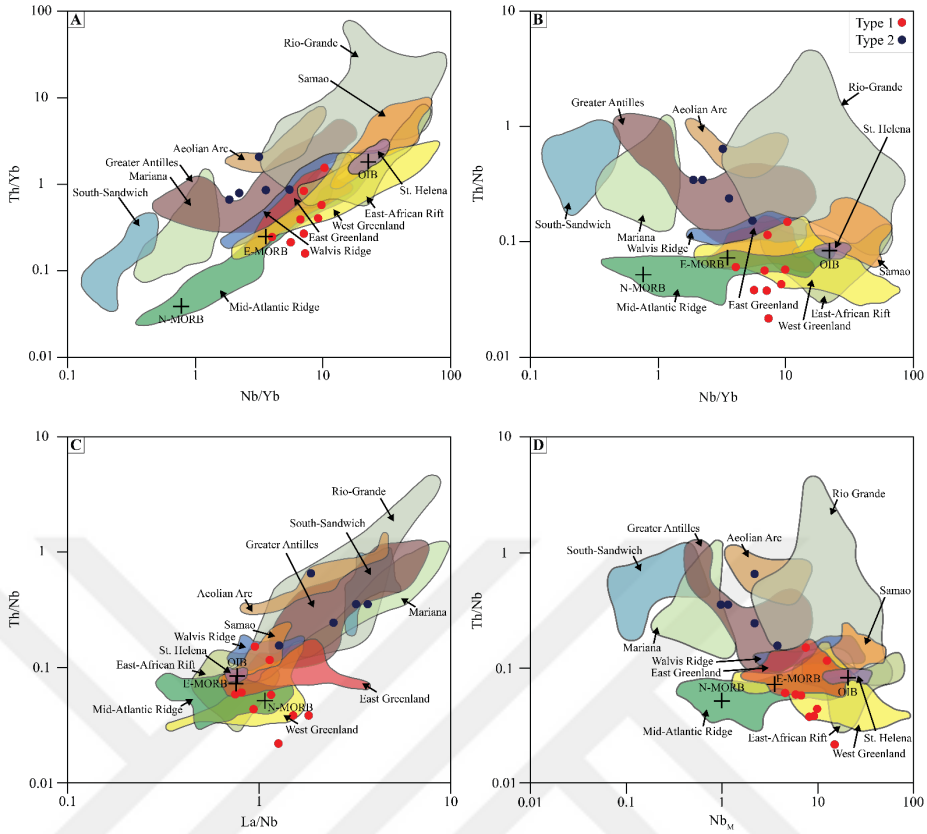


Figure 4.12. Comparison of selected element ratios of amphibolites within Söğüt Metamorphics and basalts from modern tectonic settings: (A) Nb/Yb vs. Th/Yb; (B) Nb/Yb vs. Th/Nb; (C) La/Nb vs. Th/Nb; (D) Nb_N vs. Th/Nb. Data sources: Mariana Back-Arc (Pearce et al., 2005); South-Sandwich Arc (Pearce et al., 1995); Aeolian Arc (Calanchi et al., 2002); Greater Antilles Arc (Jolly et al., 2007); Mid-Atlantic Ridge (Niu et al., 2001); Walvis Ridge (Salters and Salci-Kocher, 2010); East-African Rift (Furman et al., 2006); Rio-Grande Rift (Gibson et al., 1993); West Greenland (Larsen et al., 2003); East Greenland (Hanghøj et al., 2003); St. Helena (Kawabata et al., 2011); Samoa (Jackson et al., 2010). E-MORB, N-MORB, and OIB values are taken from Sun and McDonough (1989). Fields of Mariana Back-Arc, South-Sandwich Arc, Aeolian Arc, Greater Antilles Arc, East African Rift and Rio-Grande Rift for (A) and (B), and Mariana Back-arc, Greater Antilles Arc, East-African Rift and Rio Grande Rift for (C-D), and South-Sandwich Arc, Aeolian Arc (D) are taken from Sayit et al. (2015). Field of Mid-Atlantic Ridge for (A) is taken from Sayit et al. (2016).

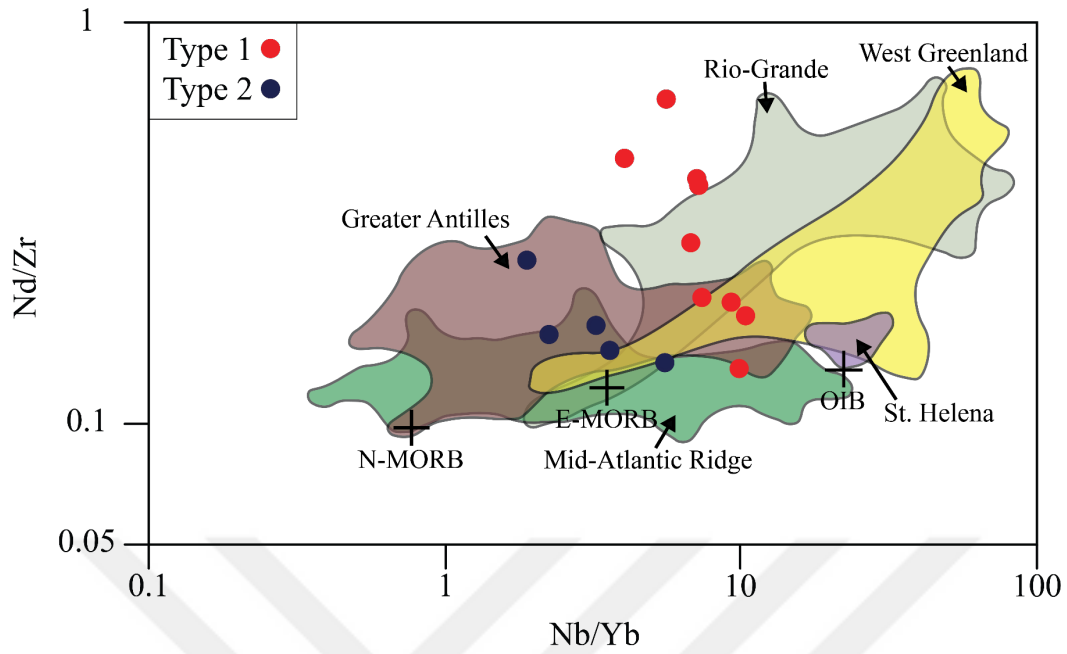


Figure 4.13. Comparison of selected element ratios (Nb/Yb vs. Nd/Zr) of amphibolites within Söğüt Metamorphics and basalts from modern tectonic settings. Data sources are the same as in Figure 4.12.

This feature is typically observed in magmas developed at subduction zones where the mantle wedge is fluxed by metasomatic agents or at continental intraplate settings where the metasomatic fluids/melts infiltrate SCLM (e.g., Gibson et al., 1993; Larsen et al., 2003; Sayit et al., 2015). Metasomatism is defined as the sub-solidus modification of the chemical characteristics of a rock body via a flow of a fluid solution into the system (Best, 2003). One of the diagnostic features of mantle metasomatism is the relative enrichment of LILEs (e.g. Rb, Ba, K and Sr) and LREE with respect to primitive mantle abundances (e.g. Roden and Murthy, 1985; Willshire, 1984) which is well defined for both Type 1 and Type 2 samples. In the PM-normalized multi-element spider diagrams (Figure 4.14), LREEs and incompatible LILEs such as Rb, Sr, K and Ba show extreme enrichment.

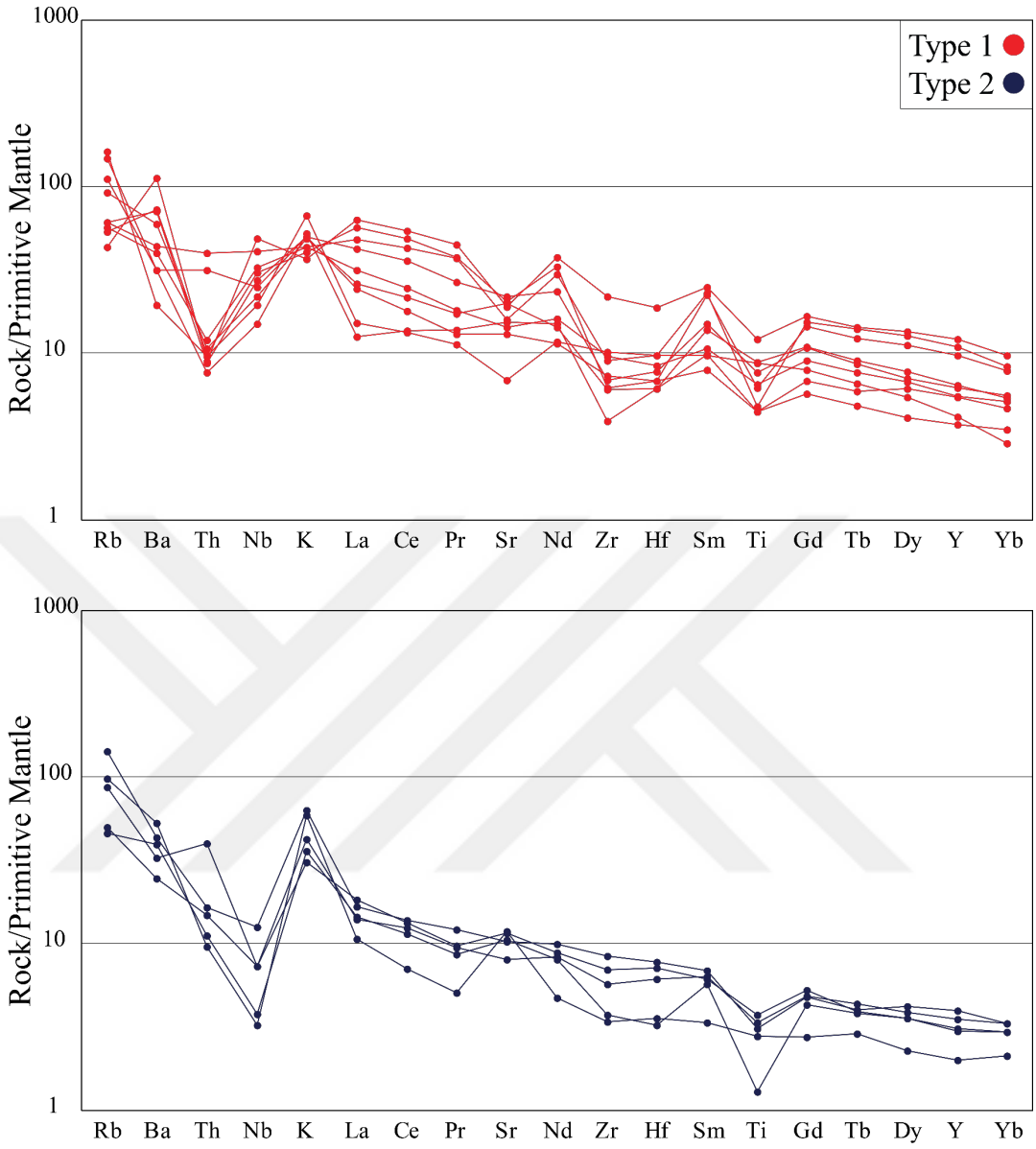


Figure 4.14. Multi-element spider diagram schematics of amphibolites from Söğüt Metamorphics, normalized with respect to Primitive Mantle. Primitive Mantle values from Sun and McDonough, 1989.

Furthermore, as discussed beforehand on the N-MORB-normalized diagrams, both Type 1 and Type 2 samples are characterized with high Nd/Zr, Sm/Hf, and Sm/Ti ratios, Type 1 samples with higher ratios. These signatures of Zr, Hf, and Ti depletion, combined with Rb, Ba, Sr, and K enrichment, indicate a role for the metasomatism of the sources of both Type 1 and Type 2 amphibolites' protoliths.

More specifically, a metasomatized SCLM source is interpreted for the protoliths of Type 1 amphibolites, whereas, a mantle source (likely to be a mantle wedge) metasomatized by slab-derived fluids/melts is proposed for the protoliths of Type 2 amphibolites.

4.2.4.3 Tectonic Discrimination

Similar to the source characteristics, each tectonic environment has its own geochemical signatures (Wood, 1980), which can be evaluated through binary and ternary tectonic discrimination diagrams, and with multi-element spider diagrams. For this reason, in addition to established discrimination diagrams, the modern tectonic settings, which were evaluated for the evolution of source characteristics, were used again, on N-MORB normalized multi-element schematic comparisons.

The Ti/Y vs. Zr/Y diagram of Pearce and Gale (1977) (Figure 4.15-A), shows that all of the samples of Söğüt Amphibolites plots within the field of Plate-Margin Basalts field including arc and arc-related environments as well as MORB material, with the exception of only one sample from Type 1 plotting to Within-Plate Basalts field including rift settings and OIB like material. However, it should be noted that a characteristic separation between amphibolite types cannot be maintained with this diagram. Furthermore, in the Ti/1000 vs. V diagram of Shervais (1982) (Figure 4.15-B), the distinction between Type 1 and Type 2 samples can be observed more clearly, with Type 1 samples having Ti/V ratios ranging from 20 and 50, and Type 2 samples having mostly a Ti/V ratio of 20. Therefore, Type 1 samples plot on to Ocean Floor Basalts (OFB) field including back-arc basalts, continental-rifts, MORBs and OIBs, whereas Type 2 samples plot on to Arc field, which includes mainly Island Arc tholeiites similar to their source characteristic discussed before.

The ternary diagrams must be discussed carefully for the tectonomagmatic characterization of the Söğüt amphibolites, particularly for Type 1 samples reflecting an unusual depletion in Zr and Hf possibly related to metasomatism. Because the

ternary diagrams are based heavily on these elements, the information reflected by such samples may result in misdirected interpretations. In the 2*Nb-Zr/4-Y diagram of Meschede (1986) (Figure 4.16-A), Type 1 samples plots on to WPA (Within-Plate Alkali), WPT (Within-Plate Tholeiites) and P-MORB fields, whereas, Type 2 samples plot on to VAB (Volcanic Arc Basalts) and N-MORB fields. In the Ti/100-Zr-3*Y diagram of Pearce and Cann (1973) (Figure 4.16-B), all the samples are scattered in all the tectonic setting variations in the diagram and do not provide a reliable distinction and interpretation. Finally, in the Hf/3-Th-Nb/16 and Zr/117-Th-Nb/16 diagrams of Wood (1980) (Figure 4.16-C, D), Type 1 samples plots on to E-MORB and rift fields, whereas, Type 2 samples are plotted onto the field of arc basalts. Altogether, these diagrams revealed a possible within-plate tectonic setting with an affinity to E-MORB and OIB for Type 1 samples, whereas an arc-related setting for Type 2 samples, coherent on all diagrams. These results appear to be consistent with the source characteristics for both chemical types. However, due to the extreme Zr-Hf depletion on the amphibolite samples, interpretations will be further discussed with multi-element spider diagram schematics.

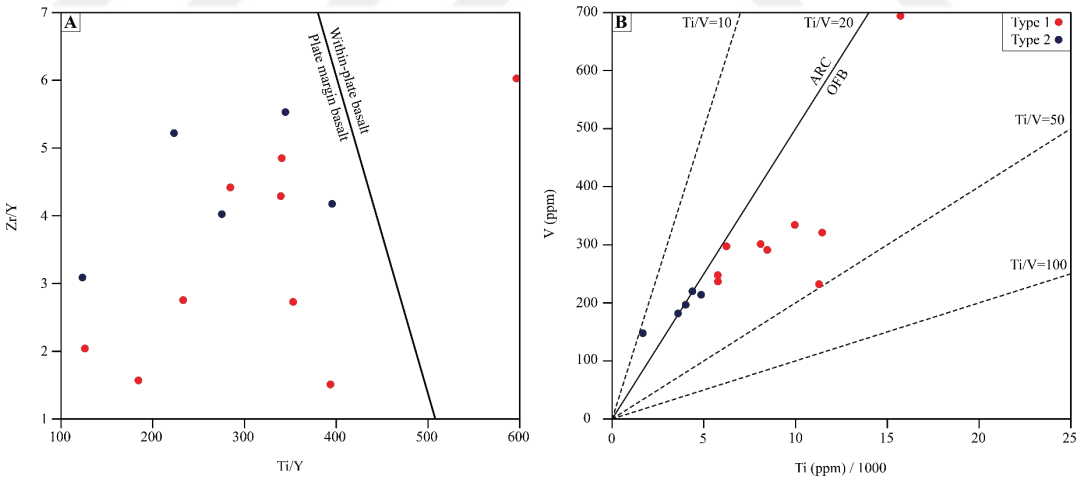


Figure 4.15. Binary tectonic discrimination diagrams: (A) Ti/Y vs. Zr/Y diagram of Pearce and Gale (1977); (B) Ti/1000 vs. V diagram of Shervais (1982). OFB: Ocean Floor Basalts.

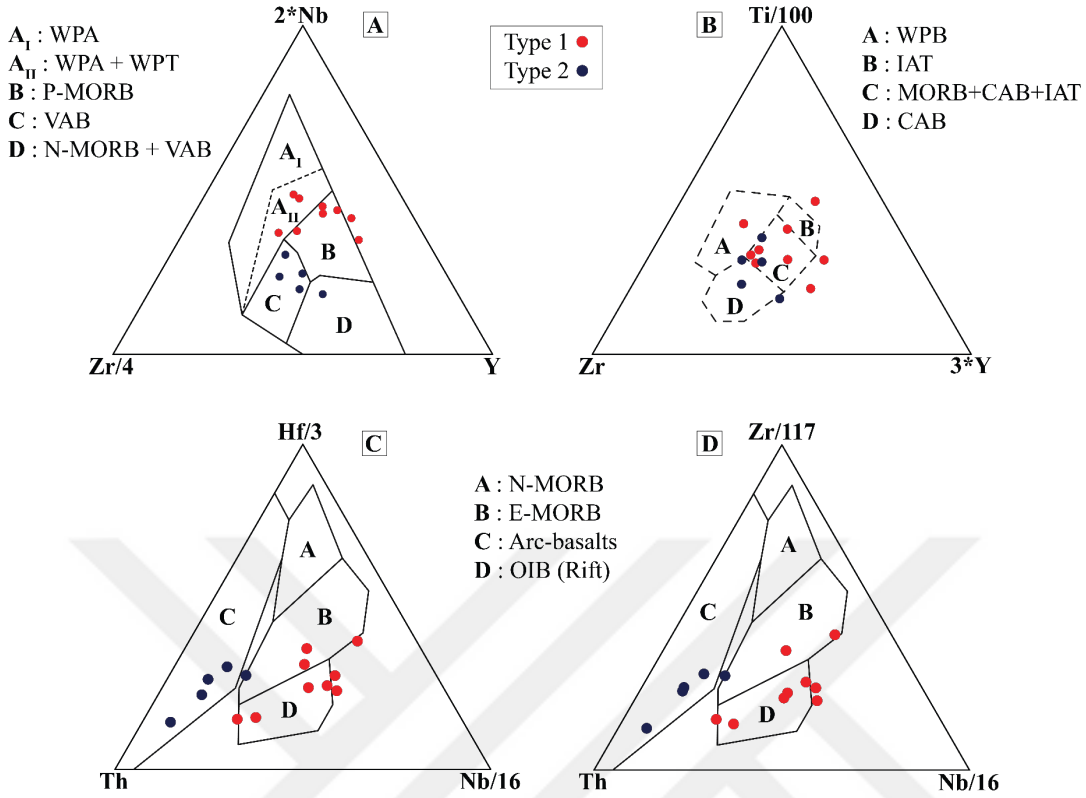


Figure 4.16. Terniary tectonic discrimination diagrams: (A) 2*Nb-Zr/4-Y diagram of Meschede (1986); (B) Ti/100-Zr-3*Y diagram of Pearce and Cann (1973); (C-D) Hf/3-Th-Nb/16 and Zr/117-Th-Nb/16 diagrams of Wood (1980). WPA: Within-Plate Alkali; WPT: Within-Plate Tholeiites; WPB: Within-Plate Basalts; VAB: Volcanic Arc Basalts; CAB: Continental Arc Basalts; IAT: Island Arc Tholeiites; MORB: Mid Oceanic Ridge Basalt; P-MORB: Primitive-MORB; N-MORB: Normal-MORB; E-MORB: Enriched-MORB; OIB: Ocean Island Basalts.

For the comparison on multi-element spider diagrams of Söğüt Amphibolites with samples from various modern tectonic settings (same settings discussed within the previous subchapter), a representative sample was chosen from each locality with MgO>4% which is also showing the most of compatible schematic with Type 1 and Type 2 samples. The samples were chosen with these criteria to demonstrate the differences/similarities thoroughly.

The comparison of Söğüt Amphibolites with samples from the mid-ocean ridge and OIB-related settings shows that both Type 1 and Type 2 samples do not have an

overlapping pattern. The samples from Mid-Atlantic Ridge (Figure 4.17-A) and Walvis Ridge (Figure 4.17-B) show that Type 2 samples are considerably depleted, whereas a relatively better overlap can be seen with Type 1 samples in terms of enrichment levels. Furthermore, the samples from the OIB environments of St. Helena (Figure 4.17-C) and Samoa Islands (Figure 4.17-D) include relatively more enriched elemental compositions than both Type 1 and Type 2 samples, as also observed in the ratio diagrams. Furthermore, both ridge- and OIB-related settings lack the strong Zr and Hf negative anomaly, characteristic of Type 1 samples, and lack the Nb and Ti negative anomaly characteristic of Type 2 samples. Therefore, it is very hard to produce a protolith for both types of amphibolites in a ridge- or OIB-related tectonic setting.

On the other hand, continental within-plate environments, such as continental rifts, are considered, a perfect match was observed for the Type 1 samples' pattern, whereas Type 2 samples do not have an overlapping pattern. When compared with the Rio-Grande Rift (Figure 4.18-A), Type 1 samples are relatively depleted, yet, a very similar Zr-Hf negative anomaly is present as observed in Nb/Yb vs. Nd/Zr diagram (Figure 4.13). Furthermore, a slight Nb negative anomaly is noticeable, similar to two of the Type 1 samples. The East-African Rift (Figure 4.18-B), appears to be a perfect match to produce Type 1 samples with relatively similar Zr and Hf negative anomaly, as well as having a similar level of enrichment. When the transitional to alkaline basaltic rocks of East and West Greenland (Continental within-plate) (Figure 4.18-C, D) is considered, it was observed that they have a very confirmable trend with the Type 1 samples, having a similar range of Zr and Hf negative anomaly, with a comparable level of enrichment. On the other hand, when the Type 2 samples are considered with respect to these settings, it was observed that the samples from these settings are much more enriched and have much stronger Zr and Hf negative anomaly, while lacking a strong Nb and Ti negative anomaly. Therefore, a continental within-plate tectonic environment is a strong candidate to produce the protoliths of Type 1 amphibolites, whereas, such a tectonic environment is very unlikely for the generation of the protoliths of Type 2 amphibolites.

Finally, all the samples from different arc-related settings have a similar trend, including a strong Nb, a relatively week Zr and Hf, and a slight to strong Ti negative anomaly. While Type 1 samples show a completely different trend with more enriched composition on almost all the elements, Type 2 samples show a strong overlap with this trend. When the trend of the Type 2 samples is considered, while the Aeolian continental arc (Figure 4.19-C) displays enrichment in almost all the elements, South-Sandwich Island Arc (Figure 4.19-B) is extremely depleted with respect to Nb, La, Ce, Pr, and Nd elements while having a similar pattern. On the other hand, samples from Mariana Back-Arc (Figure 4.19-A) and Greater Antilles Island Arc (Figure 4.19-D) shows a great coherence with Type 2 samples. It must be noted that, while Type 1 samples dominantly have a much higher Zr and Hf depletion, a slight Nb depletion is observed in two samples. Altogether, an arc-related setting appears as the most probable tectonic environment for Type 2 samples, whereas, it is not very likely to produce the protoliths of Type 1 samples in such an environment.

To sum up, considering the tectonic discrimination diagram plots and the comparisons with the multi-elements spider schematics of various modern tectonic settings, a continental within-plate setting (e.g. continental rift) for the protoliths of Type 1 amphibolites; and an intra-oceanic subduction setting for the protoliths of the Type 2 amphibolites is concluded.

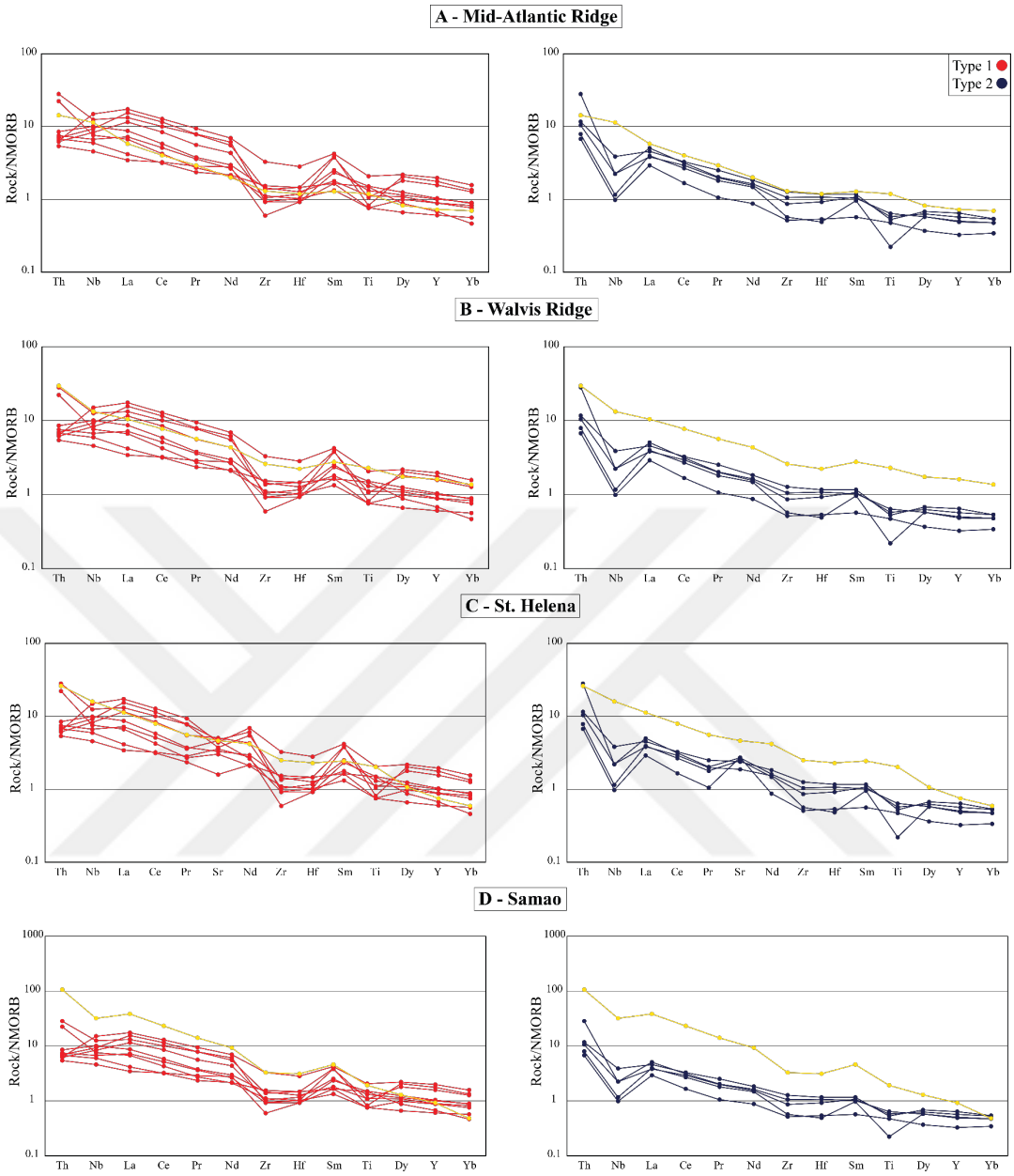


Figure 4.17. Comparison of selected samples from various MORB-OIB related tectonic settings with amphibolites from Söğüt Metamorphics with respect to multi-element spider diagrams: (A) Mid-Atlantic Ridge (Sample ID: OT18-04); (B) Walvis Ridge (Sample ID: 74-528-46R-1, 78-86); (C) St. Helena (Sample ID: SH-15); (D) Samoa (Sample ID: ALIA-DR118-23). Normalized with respect to N-MORB, values from Sun and McDonough (1989). Data sources are same with Figure 4.12.

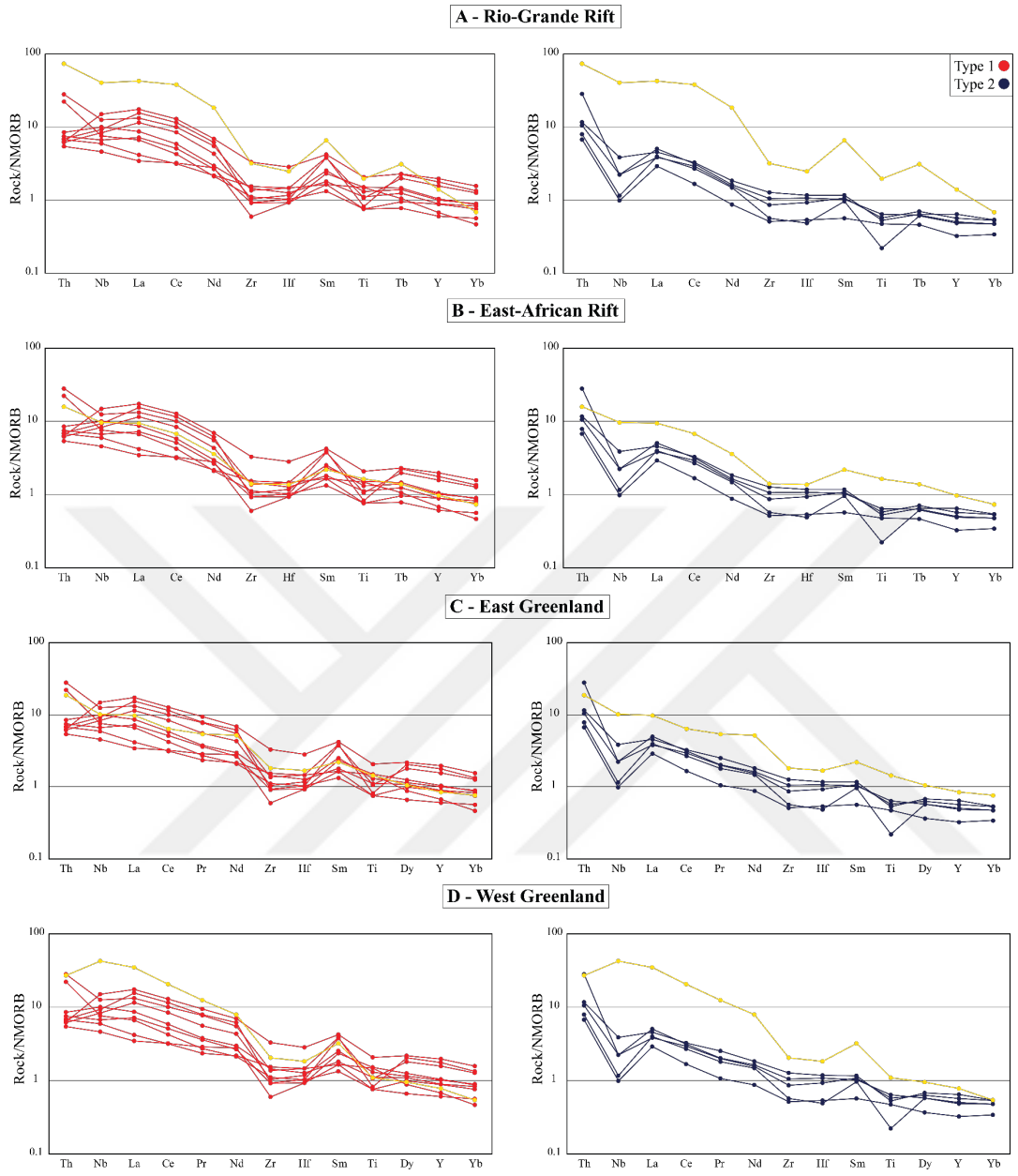


Figure 4.18. Comparison of selected samples from various continental within-plate tectonic settings with amphibolites from Söğüt Metamorphics with respect to multi-element spider diagrams: (A) Rio-Grande Rift (Sample ID: 89LT192); (B) East-African Rift (Sample ID: KL 18); (C) East Greenland (Sample ID: 417377); (D) West Greenland (Sample ID: 326787). Normalized with respect to N-MORB, values from Sun and McDonough (1989). Data sources are same with Figure 4.12.

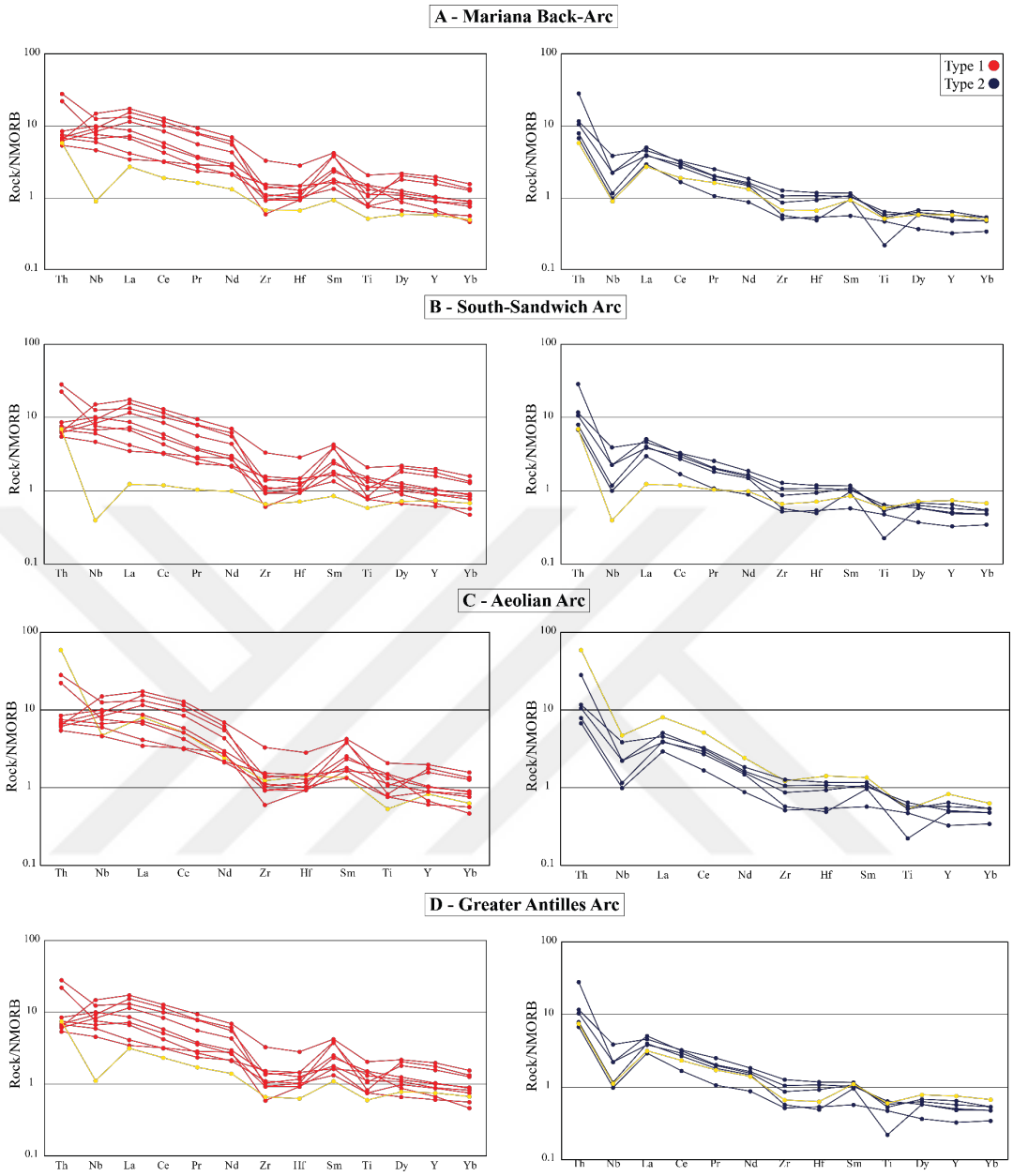


Figure 4.19. Comparison of selected samples from various arc and arc related tectonic settings with amphibolites from Söğüt Metamorphics with respect to multi-element spider diagrams: (A) Mariana Back-Arc (Sample ID: D7-1-1); (B) South-Sandwich Arc (Sample ID: SST 7(1)); (C) Aeolian Arc (Sample ID: PN255); (D) Greater Antilles Arc (Sample ID: RBL135/51). Normalized with respect to N-MORB, values from Sun and McDonough (1989). Data sources are same with Figure 4.12.

CHAPTER 5

DISCUSSION

This chapter includes an overview of all the presented data, including the field and petrographic observations integrated with the interpretations of analytical results retrieved with whole-rock geochemistry and U-Pb zircon geochronology from the amphibolites within the Söğüt Metamorphics. Furthermore, these derivations will be discussed with respect to the previous studies, and the resolution of the geodynamic evolution of the Sakarya Composite Terrane (SCT) will be enriched.

5.1 Field Characteristics of Amphibolites

In the field, amphibolites within the Söğüt Metamorphics were observed with fine- and coarse-grained varieties as bands, lenses, boudins, or tectonic slices within para- and ortho-gneisses. The fine-grained group amphibolites appear as completely black, whereas the coarse-grained amphibolites have the characteristic black and white color due to 50-50% plagioclase-hornblende abundance. Outcrops of the amphibolites are mostly weathered; fresh exposures are rarely found. In addition, brittle deformation is apparent throughout the outcrops with joint set developments. Furthermore, migmatitic fabrics were observed on the coarse-grained amphibolites indicatives of partial melting conditions. Finally, foliation is only seldomly apparent on the coarse-grained amphibolites.

It was previously mentioned that amphibolites cross-cuts the orthogneisses and a metaclastic sequence of metaconglomerate, quartzite, quartz-schists and paragneiss disconformably covers the later assemblage (Uğurcan et al., 2019). However, such an observation was not confirmed throughout the field study, instead, the protoliths of orthogneisses was observed as an intruded body into the previously deposited protoliths of paragneisses, where amphibolites were situated within both para- and

ortho-gneisses combined. Furthermore, although quartzite, quartz-schists were present seldomly, metaconglomerate was not present in the N-S sections that were examined within this study.

A complete petrofabric analysis was not conducted throughout the study. However, the foliation measurements taken from paragneisses outcrops, and the orientations of the shear zones within which amphibolites occur as lenses indicates an E-W elongated south-vergent deformation. This is consistent with the Tuzaklı-Gümele thrust fault lying to the southern margin of the Söğüt Metamorphics. This deformed nature of the Söğüt Metamorphics is further supported by the intracrystalline deformation signatures observed on plagioclase and quartz grains, and the occurrence of micro-faults displacing micro-veins as revealed by the thin-section examinations. Although ductile deformation signatures are more dominant on paragneisses, brittle deformation signatures were observed strongly on the amphibolites and orthogneisses.

5.2 Metamorphic Conditions

The petrographic examinations on the fine- and coarse-grained amphibolites revealed a similar paragenesis with hornblende-plagioclase domination along with quartz, sphene, epidote, chlorite, calcite, muscovite and zircon as accessory minerals. On the other hand, biotite was restricted to the fine-grained amphibolite samples, and the preferred orientation of this mineral defines the foliation in these lithologies. For amphibolites, hornblende+plagioclase+biotite±sphene paragenesis defines the prograde phase, whereas, epidote+chlorite+muscovite paragenesis defines the retrograde phase for the metamorphic conditions. Furthermore, the peak prograde metamorphic conditions are defined with the sillimanite+biotite±cordierite paragenesis of the host paragneisses. The coexistence of biotite-sillimanite (of paragneiss) and biotite-garnet (of orthogneiss) indicates that equilibrium is maintained at high temperatures and at upper amphibolite facies conditions (Turner, 1981). In addition, the foliation is penetrative only on the paragneiss samples, which

is defined by the preferred orientation of biotite and sillimanite, whereas, as mentioned before, foliation is dominant on the biotite-bearing fine-grained amphibolite samples. On the other hand, foliation was seldomly observed on coarse-grained amphibolites and orthogneisses. Considering these observations, the contribution of pressure is interpreted to be at low to medium grades. Altogether, on the basis of mineral assemblages indicated above, the metamorphic conditions for the Söğüt Metamorphics are identified to have occurred under high-temperature, low to medium-pressure conditions and at amphibolite facies.

5.3 Petrogenesis

The whole-rock geochemistry analyses on the amphibolites revealed two distinct chemical types concerning their protoliths with respect to their multi-element schematics. It should be mentioned that these chemical types do not show any correlation with the fine- and coarse-grained varieties distinguished in the field. Through the assessment of alteration and metamorphism effects on the amphibolites, it was observed that while the LILEs have been mobilized to some extent, though not significantly, HFSE and REEs have remained intact, showing complete immobility. The protoliths of Type 1 amphibolites have a basaltic composition with mainly transitional to alkaline affinity, whereas the protoliths of Type 2 amphibolites have basaltic to basaltic-andesitic composition with subalkaline affinity. Considering bivariate variation diagrams and Chondrite-normalized REE diagrams, it was determined that fractional crystallization is effective with the removal of pyroxene and plagioclase for Type 1 amphibolites, and only for pyroxene for Type 2 amphibolites.

On the N-MORB-normalized spider diagrams, Type 1 samples display strong negative anomaly in Zr, Hf, and Ti, whereas Type 2 samples display strong negative anomaly on Nb and Ti, and a relatively weak negative anomaly for Zr and Hf elements. Both types of amphibolites show absolute enrichment for N-MORB. Type 1 amphibolites are relatively more enriched compared to Type 2 amphibolites. On

the Nb/Yb vs. TiO_2/Yb diagram, both types are confined within the MORB array with shallow melting characteristics. Also, they plot around the E-MORB in the same diagram, suggesting that both types may have derived from an enriched source. With bivariate ratio diagrams of Th/Yb and Th/Nb against Nb/Yb, and La/Nb vs. Th/Nb and Nb_N vs. Th/Nb, differentiation of the source characteristic of amphibolite types were further characterized. Within these plots, it was observed that Type 1 samples are primarily characterized by enriched non-subduction signatures and somewhat analogous to magmas generated at modern continental intraplate settings. On the other hand, Type 2 samples are particularly enriched in subduction-mobile elements with E-MORB-like HFSE and HREE signatures, thus reflecting geochemical features more akin to the magmas from intra-oceanic subduction zones.

The effect of metasomatism on the protoliths of amphibolites was examined by Nb/Yb vs. Nd/Zr plot, as well as PM-normalized multi-element diagrams, including both immobile and mobile elements. On the bivariate ratio diagrams, it was observed that Type 1 amphibolites are characterized with high ratios of Nd/Zr, similar to continental intraplate lavas derived from metasomatized sources, such as the Rio-Grande rift and West-Greenland. On the other hand, Type 2 samples show similar values to the subduction zone magmas, where the mantle source is fluxed by slab-derived melts. This is evidenced by the PM-normalized multi-element diagram, where a decoupling occurs between LILEs-Th-LREEs and HFSEs-HREEs, with the relative enrichment in the former elements. Consequently, a metasomatized SCLM source is proposed for Type 1 amphibolites. On the other hand, a subduction-modified mantle source appears to be more suitable for the petrogenesis of Type 2 amphibolites.

Binary and ternary tectonic discrimination diagrams suggest a within-plate setting for the crystallization of protoliths of Type 1 amphibolites, whereas an arc setting for Type 2 amphibolites. The results from these diagrams were further supported by the N-MORB-normalized spider diagrams, in which the Söğüt Amphibolites are compared with the samples from various modern tectonic settings worldwide. In these plots, Type 1 amphibolites show a strong correlation with continental within-

plate settings (e.g. Rio-Grande rift, East-African rift, East-Greenland, and West Greenland), with also comparable levels of Zr-Hf negative anomalies. On the other hand, Type 2 amphibolites display similar trends with subduction-related settings characterized by strong Nb and Ti, and slight Zr-Hf negative anomalies. Furthermore, concerning the origin of Type 2 samples, an intra-oceanic subduction setting (e.g. Greater Antilles Arc, Mariana back-arc) seems a more suitable alternative rather than a continental arc setting (e.g. Aeolian Arc). Altogether, combining the interpretations on the source characteristics and tectonic environment, melt generation from a metasomatized SCLM source in a within-plate rift setting is concluded for the protoliths of Type 1 amphibolites, whereas a slab-modified mantle wedge in an intra-oceanic subduction setting is concluded for the protoliths of Type 2 amphibolites.

5.4 Tozman Metaophiolite

In addition to the amphibolites, and para- and ortho-gneisses of the Söğüt Metamorphics, Tozman Metaophiolite was also examined in detail with respect to field relationships and petrographic properties. The field observations revealed the tectonic emplacement of the gabbroic and ultramafic body as a discontinuous slice onto the Söğüt Metamorphics. The sheared contacts between the leuco-gabbros and orthogneisses are located to the south and north, with E-W elongation, with N-S elongated strike-slip faults connecting the shear zones at the eastern and western limits. In addition, a large road-cut surfaced a section of the body to the north of Çayköy Village. Within this outcrop, the inner structure revealed thrusting to both south and north at respective boundaries.

Previously Othman (2016) and Topuz et al. (2020) interpreted this ophiolitic body as an intrusion into the Söğüt Metamorphics during the Variscan orogeny, yet the observations conducted throughout this study suggests an opposite interpretation. Furthermore, there is no radiometric age data retrieved previously from this unit, therefore the geodynamic position of this unit within the evolution of the area is

extremely controversial. However, considering that the Tozman Metaophiolite was not metamorphosed to the grade that of the Söğüt Metamorphics and also that it was not cross-cut by the Sarıcakaya Granitoid, the ophiolitic body can be interpreted to have been emplaced at a later stage than the Late Carboniferous. This, in turn, suggests that the ophiolite emplacement is related to post-Variscan events.

5.5 Formation and Metamorphism Age

The zircon U-Pb LA-MC-ICP-MS spot analysis revealed Ordovician (465-459 Ma) and Carboniferous (336-327 Ma) crystallization ages for the protoliths of Type 1 and Type 2 amphibolites, respectively. Furthermore, spots that were located within the rims of the zircons of two samples of Type 1 yielded Carboniferous (332.3 ± 5.3 Ma and 339 ± 14 Ma) ages. The Th/U ratios retrieved from the spots on the rims of zircons are all greater than 0.1 (with the exception of four measurements, which is statistically insignificant). This result also indicates that these measurements are related to a magmatic overgrowth, rather than a metamorphic overprint; therefore, the Carboniferous magmatism is further confirmed with rim measurements from the zircons of Ordovician Type 1 samples. The U-Pb dating enabled to differentiate the crystallization ages of Type 1 and Type 2 amphibolites and distinguished for the first time a later-stage basic magmatism before the metamorphism of the pre-Variscan Central Sakarya basement.

Considering the age constraints previously available in the literature (Table 5.1) on the Paleozoic basement of the Central Sakarya Terrane, there appear several geochronological attempts on the schists, amphibolites, paragneisses, and orthogneisses from the Söğüt Metamorphics. For the sillimanite-bearing-schists, detrital zircon U-Pb ages are presented as Precambrian-Cambrian (2738-551 Ma) (Ustaömer et al., 2012), whereas the ages from detrital zircons of a metaconglomerate and paragneiss samples were introduced as Cambrian-Ordovician (532-444 Ma; Uğurcan et al., 2019), and with a peak at Ordovician (Mueller et al., 2019), respectively. Furthermore, the crystallization ages of the protoliths of

orthogneisses with U-Pb zircon geochronology were published as Cambrian-Early Ordovician (503-473 Ma) (Uğurcan et al., 2019) and Silurian (435-430 Ma) (Topuz et al., 2020). Finally, for the crystallization ages of the protoliths of amphibolites, two distinct U-Pb zircon ages are available (although these studies are statically questionable, due to very limited amount of measurements) as Early Ordovician (472 Ma) (Uğurcan et al., 2019) and Silurian (434-419 Ma) (Topuz et al., 2020).

Table 5.1. Geochronological data from the Söğüt Metamorphics (SM) and Bayırköy Formation (BF).

Age (Ma)	Period	Lithology	Mineral	Method	Study
336-327	Middle Carboniferous*	Amphibolite (SM)	Zircon (Magmatic)	U-Pb	This Study
465-459	Middle Ordovician*	Amphibolite (SM)	Zircon (Magmatic)	U-Pb	This Study
2738-551	Precambrian-Cambrian*	Schists (SM)	Detrital Zircon	U-Pb	Ustaömer et al., 2012
?	Ordovician Peak*	Paragneiss (SM)	Detrital Zircon	U-Pb	Muellar et al., 2019
503-473	Cambrian-Early Ordovician*	Orthogneiss (SM)	Zircon (Magmatic)	U-Pb	Uğurcan et al., 2019
472	Early Ordovician*	Amphibolite (SM)	Zircon (Magmatic)	U-Pb	
335	Carboniferous**	Paragneiss (SM)	Biotite	Ar-Ar	
331	Carboniferous**	Paragneiss (SM)	Muscovite	Ar-Ar	
532-444	Cambrian-Ordovician*	Metaconglomerate (?) (SM)	Detrital Zircon	U-Pb	
435-430	Silurian*	Orthogneiss (SM)	Zircon (Magmatic)	U-Pb	Topuz et al., 2020
434-419	Silurian*	Amphibolite (SM)	Zircon (Magmatic)	U-Pb	
346-319	Carboniferous**	Sandstone (BF)	Detrital Rutile	U-Pb	Şengün et al., 2020

*Crystallization age, **Metamorphism age

When the published geochronological data mentioned above are integrated with the analyses conducted in this study, it appears that the protoliths of the paragneisses and schists were deposited during the Ordovician or an older period. Furthermore, the provenance study of Ustaömer et al. (2012) on the sillimanite-bearing-schists suggests that the sources of the protoliths originated from northern Gondwana, specifically the Arabian-Nubian shield. The data provided by Mueller et al. (2019) also constrain the deposition of the protoliths of paragneisses to be completed by Ordovician. On the other hand, detrital zircon ages from metaconglomerate (?)

sample of Uğurcan et al. (2019) denoted that the maximum deposition age is Latest Ordovician, which is not consistent with the provenance study of Ustaömer et al. (2012), and further contradicts the geodynamic evolution that is proposed with the new data presented in this study. In addition, the dating on metaconglomerate was presented to be proceeded on a single sample, which provides limited data on the evolution of a complex metamorphic belt.

The anorogenic acidic magmatism (Topuz et al., 2020), which later produced the orthogneisses of the Söğüt Metamorphics, appears to have taken place during the Cambrian to Silurian (Uğurcan et al., 2019 and Topuz et al., 2020 combined). However, it should be noted that, there appears a 40-70 Ma age difference between the ages retrieved from the same unit within the Söğüt Metamorphics in these two publications.

On the other hand, for the protoliths of the amphibolites, the basic magmatism events were separated into two on the basis of the data presented in this study. Combining the data previously available in the literature and this study, the first phase of basic magmatism (which is referred to as the crystallization of the protoliths of Type 1 amphibolites) started during the Ordovician (this study; Uğurcan et al., 2019) and continued until the Silurian (Topuz et al., 2020). Although an overlapping age constraint is observed with the data presented in Uğurcan et al. (2019), again a strong contradiction is present with the ages presented in Topuz et al. (2020). The geochronological results presented in this study indicate that the magmatism that caused the within-plate rifting started during Middle Ordovician. Furthermore, the second phase of basic magmatism (which is referred to as the crystallization of the protoliths of Type 2 amphibolites' protoliths) that is distinguished within the Söğüt Metamorphics occurred during the Carboniferous, before the metamorphic event.

The ages representing the metamorphism of the CST are presented as Carboniferous (335-331 Ma by Ar-Ar dating on biotite and muscovite) from a paragneiss sample (Uğurcan et al., 2019). In addition, detrital rutile U-Pb dating on sandstone samples from the Bayırköy Formation yielded 346 Ma and 319 Ma lower intercept ages,

which are inferred to represent the metamorphism age of the Söğüt Metamorphics (Şengün et al., 2020). These ages display an overlap with the crystallization ages of Type 2 amphibolites. This conflict brings out two possible scenarios for the evaluation of the Type 2 amphibolites. In the first scenario, the Type 2 protoliths were formed as an intra-oceanic arc setting, then they underwent metamorphism in a separate event with respect to the rest of the CST basement assemblage and amalgamated later on. In the second scenario, after the crystallization of Type 2 amphibolites, they were amalgamated in a short time frame to the CST basement assemblage, and the whole body underwent metamorphism in a singular event. Considering the geological and petrographical features of Type 2 amphibolites, the second scenario appears to be more likely. In the field, amphibolite bodies are emplaced entirely within the host gneissic bodies, and the geochemical distribution of amphibolites is also interchanging. Furthermore, these lithologies have mineral parageneses that indicate identical metamorphic P-T conditions. It seems more likely, therefore, that the metamorphic event is singular. However, to construct a well-established metamorphic history of the CST, more analytical data are required, particularly from the amphibolites themselves. This can be carried out by Ar-Ar dating on hornblende or U-Pb dating on sphene from Type 1 and Type 2 amphibolites, which would, in turn, help to understand the whole metamorphic history thoroughly.

5.6 Regional Geodynamic Implications

As it is mentioned in the overview presented above, the first phase of basic magmatism occurred in a continental within-plate setting, similar to the interpretations of Uğurcan et al. (2019) and Topuz et al. (2020). The whole-rock geochemical analysis conducted in this study and by Topuz et al. (2020) indicates that this event was caused by within-plate rifting. Within this study it was further established that this rifting is related to a magmatic event with a metasomatized SCLM source. On the other hand, the second phase of basic magmatism that took

place in the Carboniferous appears to have occurred as intra-oceanic arc magmatism, which is later amalgamated to the basement consisting of the protoliths of para- and ortho-gneisses, and Type 1 amphibolites before the metamorphism of the basement assemblage.

The first phase (Type 1 amphibolites) of basic magmatism is interpreted to occur during the rifting of the northern margin of Gondwana during the Middle Ordovician. This rifting event is further correlated with the initial separation of the fragments of the peri-Gondwanan or northern Turkish Terranes and led to the opening of a Paleozoic oceanic branch within an arc-like continental terrane with silicic rocks (paragneisses) and a granitic substratum (orthogneisses). Whether this oceanic branch corresponds to the Paleo-Tethys Ocean (e.g sensu Stampfli, 2000; Topuz et al., 2020) or to the Rheic Ocean (e.g. sensu Göncüoğlu, 1997; Nance et al., 2010) is an ongoing matter of debate. Topuz et al. (2020) and Uğurcan et al. (2019) have proposed that this rifting event is correlated with the opening of Paleo-Tethys Ocean, whereas, Stampfli (2000) indicated that a back-arc spreading event caused the opening of Paleo-Tethys Ocean due to the southward subduction of Rheic Ocean. Although overlapping petrogenetic implications were proposed by Topuz et al. (2020), the geochronological findings of this study indicate that the basic magmatism that caused the rifting of peri-Gondwanan Terranes started earlier, during Middle Ordovician, rather than Silurian. On the other hand, considering the new findings discussed in this chapter, particularly, the field observations, petrological futures and geochronological constraints, it appears more likely that this event contributes to the opening of Rheic Ocean sensu Göncüoğlu (1997), rather than Paleo-Tethys Ocean sensu Stampfli (2000).

The second phase (Type 2 amphibolites) of basic magmatism is interpreted to occur at an intra-oceanic subduction zone within the same Paleozoic Ocean during the Middle Carboniferous. The protoliths of the Type 2 amphibolites were then collided with continental lithosphere-type intruded by the protoliths of the Type 1 amphibolites. This collision and related crustal thickening may have resulted in

intense deformation and metamorphism at amphibolite facies during the Middle to Late Carboniferous and the generation of the Söğüt Metamorphics.

Regionally, these successions of events are contemporaneous with the late stages of the Variscan Orogeny as a result of the closure of the Paleozoic Ocean. Following the main metamorphic event, the melting of the lower continental lithosphere gave way to the formation of the Sarıcakaya Granitoid cross-cutting the Söğüt Metamorphics during the Late Carboniferous, completing the formation of the Paleozoic basement assemblage of Central Sakarya Terrane.

CHAPTER 6

CONCLUSION

Considering the field observations, petrographic examinations, integrated with whole-rock geochemistry and zircon U-Pb geochronology on the amphibolites within the Söğüt Metamorphics of the Central Sakarya Terrane (CST) the following conclusions are finalized:

1. Amphibolites are situated within the host para- and ortho-gneisses, and they occur as bands, lenses, boudins, or tectonic slices. In hand specimen, amphibolites have fine- and coarse-grained varieties. In the field, foliation was not observable in fine-grained outcrops, whereas it was weekly developed on coarse-grained outcrops. Migmatitic fabric was observed on coarse-grained outcrops, indicative of partial-melting conditions.
2. Under microscope, hornblende+plagioclase+biotite±sphene paragenesis defines the prograde phase, whereas, epidote+chlorite+muscovite paragenesis defines the retrograde phase for the metamorphic conditions of amphibolites. The mineral assemblage of fine- and coarse-grained amphibolites are same, except for biotite, which is exclusive for fine-grained amphibolites and defines the foliation with its' preferred orientation on these samples. Furthermore, the peak metamorphic conditions were estimated with sillimanite+biotite±cordierite paragenesis of the host paragneisses and indicates low-to-medium P/high T amphibolite facies.
3. Two distinctive geochemical signature type was established within amphibolite samples: (1) basaltic protolith with transitional to alkaline affinity, and (2) basaltic to basaltic andesitic protolith with subalkaline affinity. Type 1 amphibolites have enriched, somewhat E-MORB characteristics, with prominent negative Zr-Hf anomalies (Nd/Zr: 0.14-0.65; Sm/Hf: 1.44-4.75) and variable enrichment in the highly incompatible

elements (Nb/Yb: 4.02-10.29), and Type 2 amphibolites have subduction-modified geochemical signatures with negative Nb anomalies (Th/Nb=0.16-0.65; La/Nb=1.27-3.67). Type 1 amphibolites have a metasomatized SCLM source, whereas Type 2 amphibolites have a mantle source metasomatized by slab-derived fluids/melts. Furthermore, tectonic discrimantion diagrams indicate that the protoliths of Type 1 amphibolites crystallized in a within-plate rift setting, whereas, Type 2 amphibolites crystallized in an oceanic arc setting.

4. Geochronological examination was conducted with U-Pb zircon LA-MC-ICP-MS for samples from both amphibolite types. Samples from Type 1 amphibolites yielded Middle Ordovician (460.8 ± 2.6 Ma, 465.4 ± 2.0 Ma and 459.8 ± 2.9 Ma) $^{206}Pb/^{238}U$ weighted mean ages for the crystallization of its' protoliths, whereas samples from Type 2 amphibolites yielded Middle Carboniferous (336 ± 2.0 Ma, 327. 61 ± 0.99 Ma and 328.7 ± 1.6 Ma) $^{206}Pb/^{238}U$ weighted mean ages for the crystallization of its' protoliths. Correlated with the distinctive geochemical signatures, these ages, for the first time, revealed a second phase of basic magmatism within the Söğüt Metamorphics.
5. The geochemical and geochronological conclusions confirm the opening of a Paleozoic Tethys branch (Rheic Ocean: Göncüoğlu, 1997; Nance et al., 2010; Paleo-Tethys: Stampfli, 2000; Topuz et al., 2020) due to within-plate rifting, rather than due to back-arc spreading (Stampfli and Borel, 2002) on a Cadomian marginal arc and its Lower Paleozoic basement. Yet, our data indicates that the rifting started earlier during Middle Ordovician, rather than Silurian (Topuz et al., 2020). In addition, the newly defined Middle Carboniferous basic magmatism within this assemblage indicates occurrence of an oceanic arc within this Paleozoic Tethys, which later amalgamated to the Paleozoic basement of the CST, before its' Late Carboniferous metamorphism.

6. The “Tozman Metaophiolite” is shown to be a non-metamorphic tectonic sliver within the Söğüt Metamorphic but not their member (Göncüoğlu et al, 1996, 2000) or an ultramafic intrusive body (Othman, 2016; Topuz et al., 2020) cross-cutting them.
7. For the complete disclosure of the metamorphic age constraints of the CST, further geochronological applications are required from Type 1 and Type 2 amphibolites.

REFERENCES

Altıner, D., Koçyiğit, A., Farinacci, A., Nicosia, U. and Conti, M. A. (1991). Jurassic-Lower Cretaceous Stratigraphy and Paleogeographic Evolution of the Southern Part of North-Western Anatolia (Turkey). Geologica Rom., 27, 13-80.

Altınlı, I.E. (1975). Orta Sakarya Jeolojisi. Cumhuriyetin 50. yılı Yerbilimleri Kongresi, Maden Tetkik ve Araştırma Ens., 159-191.

Arth, J.G. (1976). Behavior of trace elements during magmatic processes - a summary of theoretical models and their applications. J. Res. U.S. Geol. Surv., 4: 41-47.

Ayaroğlu, H. (1978). Bozöyük-Söğüt Bölgesinin Jeolojsi ve Petrografisi. Ankara University, Department of Geological Engineering. [Unpublished, Ph.D. Thesis].

Bingöl, E., Akyürek, B. and Korkmazer, B. (1975). Biga yarımadasının jeolojisi ve Karakaya Formasyonunun bazı özellikleri. Proceedings of the 50th Anniversary of the Turkish Republic Earth Science Congress. Mineral Research and Exploration Institute of Turkey (MTA) Publications, 70-77. [In Turkish].

Büyükkahraman, G. (2013). Petrology and Geodynamic Evolution of Bozaniç (Sarıcakaya-Mihalgazi, Eskişehir) Eocene Volcanic Rocks. Balıkesir University, Department of Geological Engineering. [Unpublished, Ph.D. Thesis]. [In Turkish with English Abstract].

Delaloye, M. and Bingol, E. (2000). Granitoids from western and northwestern anatolia: geochemistry and modeling of geodynamic evolution. International Geology Review, 42(3): 241-268.

Calanchi, N., Peccerillo, A., Tranne, C.A., Lucchini, F., Rossi, P.L., Kempton, P., Barbieri, M. and Wu, T.W. (2002). Petrology and geochemistry of volcanic rocks from the island of Panarea: implications for mantle evolution beneath the Aeolian island arc (southern Tyrrhenian sea). J. Volcanol. Geotherm. Res., 115: 367-395.

Dalpe, C. and Baker, D.R. (1994). Partition coefficients for rare-earth elements between calcic amphibole and Ti-rich basanitic glass at 1.5 Gpa, 1100 degrees C. Mineralogical Magazine, 58: 207-208.

Demirkol, C. (1977). Geology of the Üzümlü-Tuzaklı (Bilecik Province) area. Bulletin of the Geological Society of Turkey, 20: 9-16. [In Turkish with English abstract].

Duru, M., Gedik, İ. and Aksay, A. (2002). Geological Map of the Adapazarı H24 Quadrangle, 1:100,000 Scale. General Directorate of Mineral Research and Exploration of Turkey (MTA). Department of Geological Research. [In Turkish with English abstract].

Eroskay, S.O. (1965). Paşalar boğazı-Gölpazarı sahasının jeolojisi. İstanbul Üniversitesi Fen Fakültesi Mecmuası, seri B, cilt XXX, 3-4: 135-170.

Floyd, P.A., and Winchester, J.A. (1978). Identification and discrimination of altered and metamorphosed volcanic rocks using immobile elements, 21: 291-306.

Furman, T., Kaleta, K.M., Bryce, J.G. and Hanan, B.B. (2006). Tertiary mafic lavas of Turkana, Kenya: Constraints on East African plume structure and the occurrence of High-μ volcanism in Africa. Journal of Petrology, 47(6): 1221-1244.

Gedik, İ. and Aksay, A. (2002). Geological Map of the Adapazarı H25 Quadrangle, 1:100,000 Scale. General Directorate of Mineral Research and Exploration of Turkey (MTA). Department of Geological Research. [In Turkish with English abstract].

Gibson, S.A., Thompson, R.N., Leat, P.T., Morrison, M.A., Hendry, G.L., Dickin, A.P. and Mitchell, J.G. (1993). Ultrapotassic Magmas along the Flanks of the Oligo-Miocene Rio Grande Rift, USA: Monitors of the Zone of Lithospheric Mantle extension and thinning beneath a continental rift. Journal of Petrology, 34(1): 187-228.

Göncüoğlu, M.C. (2019). A Review of the Geology and Geodynamic Evolution of Tectonic Terranes in Turkey. In: Pirajno F., Ünlü T., Dönmez C., Şahin M. (Eds). Mineral Resources of Turkey. Modern Approaches in Solid Earth Sciences, 16: 19-72.

Göncüoğlu, M.C. (2010). Introduction to the geology of Turkey: Geodynamic evolution of the Pre-Alpine and Alpine terranes. MTA Monography Series. 5: 1-69.

Göncüoğlu, M.C., Gürsu, S., Tekin, U.K., and Köksal, S. (2008). New data on the evolution of the Neotethyan oceanic branches in Turkey: Late Jurassic ridge spreading in the Intra-Pontide branch. Ofioliti, 33: 153-164.

Göncüoğlu, M.C., Çapkınoğlu, S., Gürsu, S., Noble, P., Turhan, N., Tekin, U.K., Okuyucu, C., and Göncüoğlu, Y. (2007). The Mississippian in the Central and Eastern Taurides (Turkey): constraints on the tectonic setting of the Tauride-Anatolide Platform. Geologica Carpathica, 58: 427-442.

Göncüoğlu, M.C., Turhan, N., Şentürk, K., Özcan, A., Uysal, Ş. and Yaliniz, M.K. (2000). A Geotraverse Across Northwestern Turkey: Tectonic Units of the Central Sakarya Region and their Tectonic Evolution. In: Bozkurt, E., Winchester, J.A. and Piper, J.A.D. (Eds), Tectonics and Magmatism in Turkey and Surrounding Area. Geological Society, London, Special Publications, 173: 139-161.

Göncüoğlu, M.C. and Kozlu, H. (2000). Early Paleozoic evolution of the NW Gondwanaland: data from southern Turkey and surrounding regions. Gondwana Research, 3: 315-323.

Göncüoğlu, M.C. and Kozur, H. (1999). Remarks on the pre-Variscan development in Turkey. In: Linnemann, U., Heuse, T., Fatka, O., Kraft,P. Brocke, R. and Erdtmann, B.T. (Eds), Pre-variscan Terrane Analyses of "Gondwanean Europa", Proceedings, Schriften des Staatl. Mus. Min. Geol. Dresden, 9: 137-138.

Göncüoğlu, M.C. (1997). Distribution of Lower Paleozoic rocks in the Alpine terranes of Turkey: Paleogeographic Constraints. Turkish Association of Petroleum Geologists Special Publication. 3: 13-23.

Göncüoğlu, M.C., Dirik, K. and Kozlu, H. (1997). Pre-Alpine and Alpine terranes in Turkey: Explanatory notes to the terrane map of Turkey. Annales Géologiques Des Pays Helléniques. 37: 515-536.

Göncüoğlu, M.C., Turhan, N., Şentürk, K., Uysal, Ş., Özcan, A. and Işık, A. (1996). Geological characteristics of the strucural units in Central Sakarya between Nallihan and Saricakaya. General Directorate of Mineral Research and Exploration of Turkey (MTA). [Unpublished, Report No: 10094]. [In Turkish].

Göncüoğlu, M.C., Erendil, M., Tekeli, O., Aksay, A., Kuşcu, İ. and Ürgün, B. (1987). Geology of the Armutlu Peninsula. In: Field Excursion along W-Anatolia. Mineral Research and Exploration Institute of Turkey (MTA) Publications, 12-18.

Gürsu, S. and Göncüoğlu, M.C. (2005). Early Cambrian back-arc volcanism in the western Taurides, Turkey: implications for rifting along the northern Gondwanan margin. Geol Mag., 142: 617-631.

Granit, Y. and Tintant, H. (1960). Observations preliminaires sur le Jurassique de la region de Bilecik (Turquie). Lab. de Geol. Geol. Faculte des Sciences, Dijon.

Hanghøj, K., Storey, M and Stecher, O. (2003). An isotope and trace element study of the East Greenland Tertiary dyke swarm: Constraints on temporal and

spatial evolution during continental rifting. Journal of Petrology, 44(11): 2081-2112.

Hart, S.R., Erlank, A.J., and Kable, E.J.D. (1974). Sea Floor Basalt Alteration: Some Chemical and Sr Isotopic effects. Contributions to Mineralogy and Petrology, 44: 219-230.

Higuchi, H. and Nagasawa, H. (1969). Partition of trace elements between rock-forming minerals and the host volcanic rocks. Earth and Planetary Science Letters, 7: 281-287.

İlbeyli, N., Demirbilek, M., Kibici, Y. (2015). Geochemistry and petrogenesis of the Late Paleozoic magmatism in the Sakarya Zone (NW Turkey). Journal of Mineralogy and Geochemistry, 192(2): 177-194.

Jackson, M.G., Hart, S.R., Konter, J.G., Koppers, A.A.P., Staudigel, H., Kurz, M.D., Blusztajn, J., Sinton, J.M. (2010). Samoan hot spot track on a "hot spot highway": Implications for mantle plumes and a deep Samoan mantle source. Geochem. Geophys. Geosyst., 11(12): 1-24.

Jackson, S.E., Pearson, N.J., Griffin, W.L., and Belousova, E.A. (2004). The application of laser ablation-inductively coupled plasma-mass spectrometry to in situ U-Pb zircon geochronology. Chemical Geology, 211: 47-69.

John T., Scherer E.E., Haase K., Schenk V. (2004). Trace element fractionation during fluid-induced eclogitization in a subducting slab: trace element and Lu–Hf–Sm–Nd isotope systematics. Earth and Planetary Science Letters, 227: 441-456.

Jolly, W.T., Schellekens, J.H., Dickin, A.P. (2007). High-Mg andesites and related lavas from southwest Puerto Rico (Greater Antilles Island Arc): Petrogenetic links with emplacement of the Late Cretaceous Caribbean mantle plume. Lithos, 98: 1-26.

Kawabata, H., Hanyu, T., Chang, Q., Kimura, J., Nichols, A.R.L. and Tatsumi, Y. (2011). The petrology and geochemistry of St. Helena Alkali Basalts: Evaluation of the oceanic crust-recycling model for HIMU OIB. Journal of Petrology, 52: 791-838.

Ketin, İ. (1966). Tectonic units of Anatolia, Mineral Research and Exploration Institute of Turkey (MTA) Bulletin, 66: 23-34.

Kibici, Y., İlbeyli, N., Yıldız, A. and Bağcı, M. (2010). Geochemical constraints on the genesis of the Saricakaya intrusive rocks, Turkey: Late Paleozoic crustal melting in the central Sakarya Zone. Chemie Der Erde, 70: 243–256.

Koçyiğit, A., Altiner, D., Farinacci, A., Nicosia, U. and Conti, M.A. (1991). Late Triassic-Aptian Evolution of the Sakarya Divergent Margin: Implications for the Opening History of the Northern Neo-Tethys, in North-Western Anatolia, Turkey. Geologica Rom. 27: 81-99.

Lapierre, H., Samper, A., Bosch, D., Maury, R. C., Bechennec, F., Cotten, J., Demant, A., Brunet, P., Keller, F., Marcoux, J. (2004). The Tethyan plume: Geochemical diversity of Middle Permian basalts from the Oman rifted margin. Lithos, 74, 167-198.

Larsen, L.M., Pedersen, A.K., Sundvoll, B. and Frei, R. (2003). Alkali picrites formed by melting of old metasomatized lithospheric mantle: Manitdlat Member, Vaigat Formation, Palaocene of West Greenland. Journal of Petrology, 44 (1): 3-38.

Ludwig, K.R. (2008). Manual for Isoplot 3.7: Berkeley Geochronology Center, Special Publication, 4: 77.

Marroni, M., Göncüoğlu, M.C., Frassi, C., Sayit, K., Pandolfi, L., Ellero, A., Ottria, G. (2020). The Intra-Pontide ophiolites in Northern Turkey revisited: From birth to death of a Neotethyan oceanic domain. Geosciences Frontiers, 11: 129-149.

Meschede, M. (1986). A method of discriminating between different types of mid-oceanic ridge basalts and continental tholeiites with the Nb-Zr-Y diagram. Chemical Geology. 56: 207–218.

Mueller, M.A., Licht, A., Campbell, C., Ocakoğlu, F., Taylor, M.H., Burch, L., Ugrai, T., Kaya, M., Kurtoğlu, B., Coster, P.M.C., Metais, G., Beard, K.C. (2019). Collision Chronology Along the İzmir-Ankara-Erzincan Suture Zone: Insights from the Sarıcakaya Basin, Western Anatolia. Tectonics, 38: 3652-3674.

Murphy, J.B., Gutierrez-Alonso, G., Nance, R.D., Fernandez-Suarez, J., Keppie, J.D., Quesada, C., Strachan, R.A., and Dostal, J. (2006). Origin of the Rheic Ocean: Rifting along a Neoproterozoic suture? Geology, 34: 325-328.

Nance, R.D., Gutierrez-Alonso, G., Keppie, J.D., Linnemann, U., Murphy, J.B., Quesada, C., Strachan, R.A., Woodcock, N.H. (2010). Evolution of the Rheic Ocean. Gondwana Research, 17: 194-222.

Nance, R.D., Linnemann, U. (2008). The Rheic Ocean: Origin, Evolution, and Significance. GSA Today. 18(12): 4-12.

Niu, Y., Bideau, D., Hekinian, R., Batiza, R. (2001). Mantle compositional control on the extent of mantle melting, crust production, gravity anomaly, ridge morphology, and ridge segmentation: a case study at the Mid-Atlantic Ridge 33-35º N. Earth and Planetary Science Letters, 186: 383-399.

Ocakoğlu, F., Hakyemez, A., Açıkalın, S., Altıner, S., Büyükmeriç, Y., Licht, A., Demircan, H., Şafak, Ü., Yıldız, A., Yılmaz, İ.Ö., Wagreich, M. and Campbell, C. (2019). Chronology of subduction and collision along the İzmir-Ankara suture in Western Anatolia: records from the Central Sakarya Basin. International Geology Review. 61(10): 1244-1269.

Okay, A.I., Sunal, G., Sherlock, S., Kylander-Clark, A.R.C. and Özcan, E. (2020). İzmir-Ankara suture as a Triassic to Cretaceous plate boundary - data from central Anatolia. Tectonics, In Press.

Okay, A.I. and Topuz, G. (2017). Variscan Orogeny in the Black Sea Region. International Journal of Earth Sciences. 106: 569-592.

Okay, A.I. and Nikishin, A.M. (2015). Tectonic evolution of the southern margin of Laurasia in the Black Sea region. International Geological Review. 57(5-8): 1051-1076.

Okay, A.I., Noble, P.J., Tekin, U.K. (2011). Devonian radiolarian ribbon cherts from the Karakaya Complex, Northwest Turkey: Implications for the PaleoTethyan evolution. C.R. Palevol, 10: 1-10.

Okay, A.I., Satır, M. and Siebel, W. (2006). Pre-Alpide Palaeozoic and Mesozoic orogenic events in the Eastern Mediterranean region. In: Gee, D. G. and Stephenson, R. A. (Eds). European Lithosphere Dynamics. Geol. Soc. London, Memoirs, 32: 389-405.

Okay, A.I. and Göncüoğlu, M.C. (2004). The Karakaya Complex: A review of data and concepts. Turkish Journal of Earth Sciences. 13: 77-95.

Okay, A.I., Satır, M., Maluski, H., Siyako, M., Monie, P., Metzger, R. and Akyüz, S. (1996). Paleo- and Neo-Tethyan events in northwest Turkey: geological and geochronological constraints. In: A. Yin and M. Harrison (Eds). Tectonics of Asia, Cambridge University Press, 420-441.

Okay, A. I., Siyako, M. and Bürkan, K.A. (1991). Geology and tectonic evolution of the Biga Peninsula. Special Issue on Tectonics (Ed. J.F. Dewey). Bulletin of the Technical University of Istanbul, 44: 191-255.

Othman, M. and Hassan, S.H. (2018). Using Trace Element Discrimination of Different Types of Plutonic Rocks to Identify Tectonic Setting of Sarıcakaya Complex (Eskişehir, NW Turkey). Special Issue for the 2nd Annual Conference on Theories and Applications of Basic and Biosciences. 620-627.

Othman, M. (2016). Petrogenesis of the Sarıcakaya Intrusive Rocks (Eskişehir, NW Turkey) and Their Implications. İstanbul Technical University (ITU), Eurasia Institute of Earth Sciences. [Unpublished, M.Sc. Thesis].

Paton, C., Hellstrom, J., Paul, B., Woodhead, J., Hergt, J. (2011). Iolite: freeware for the visualisation and processing of mass spectrometric data. J. Anal. At. Spectrom., 26: 2508-2518.

Pearce, J.A. (2008). Geochemical fingerprinting of oceanic basalts with applications to ophiolite classification and the search for Archean oceanic crust. Lithos, 100: 14-48.

Pearce, J.A., Stern, R.J., Bloomer, S.H., Fryer, P. (2005). Geochemical mapping of the Mariana arc-basin system: implications for the nature and distribution of subduction components. Geochem. Geophys. Geosyst., 6(7): 1525-2027.

Pearce, J.A. (1996). A Users guide to basalt discrimination diagrams. In: Wyman, D.A. (Ed.), Trace Element Geochemistry of Volcanic Rocks: Applications for Massive Sulphide Exploration. Geological Association of Canada, Short Course Notes. 12: 79–113.

Pearce, J.A., Baker, P.E., Harvey, P.K., Luff, I.W. (1995). Geochemical evidence for subduction fluxes, mantle melting and fractional crystallization beneath the South Sandwich island arc. Journal of Petrology, 36: 1073-1109.

Pearce, J.A., and Gale, G.H. (1977). Identification of ore-deposition environment from trace-element geochemistry of associated igneous host rocks. The Institution of Mining and Metallurgy and the Geological Society, 7: 14-24.

Pearce, J.A. and Cann, J.R. (1973). Tectonic setting of basic volcanic rocks determined using trace element analyses. Earth and Planetary Science Letters, 19: 290-300.

Philpotts, A.R. and Ague, J.J. (2009). Principles of Igneous and Metamorphic Petrology. Cambridge, UK: Cambridge University Press.

Roden, M.F. and Murthy, V.R. (1985). Mantle metasomatism. Annual Review of Earth and Planetary Sciences, 13: 269-296.

Rollinson, H.R. (1993). Using Geochemical data: Evaluation, Presentation, Interpretation. Longman/Wyllie. Harlow/New York.

Salters, V.J.M. and Sachi-Kocher, A. (2010). An ancient metasomatic source for the Walvis Ridge basalts. Chemical Geology, 273: 151-167.

Sayit, K., Marroni, M., Göncüoğlu, M.C., Pandolfi, L., Ellero, A., and Frassi, C. (2016). Geological setting and geochemical signatures of the mafic rocks from the Intra-Pontide Suture Zone: implications for the geodynamic reconstruction of the Mesozoic Neotethys. Int. J. Earth Sci. (Geol. Rundsch), 105: 39-64.

Sayit, K., Göncüoğlu, M.C. and Tekin, U.K. (2015). Middle Carnian Arc-Type Basalts from the Lycian Nappes, Southwestern Anatolia: Early Late Triassic Subduction in the Northern Branch of Neotethys. Journal of Geology, 123 (6): 561-579.

Sayit, K. and Göncüoğlu, M.C. (2013). Geodynamic evolution of the Karakaya Mélange Complex, Turkey: A review of geological and petrological constraints. Journal of Geodynamics. 65: 56-65.

Sayit, K., Göncüoğlu, M.C., Furman, T. (2010). Petrological reconstruction of Triassic seamounts/oceanic islands within the Palaeotethys: geochemical implications from the Karakaya subduction/accretion Complex, Northern Turkey. Lithos, 119: 501-511.

Şengör, A.M.C., Yılmaz, Y., and Sungurlu, O. (1984). Tectonics of the Mediterranean Cimmerides: nature and evolution of the western termination of Paleo-Tethys. In: Dixon, J. E., and Robertson, A. H. F., (eds). The geological evolution of the Eastern Mediterranean. Geol. Soc. London, Spec. Publ., 17: 77-112.

Şengör, A.M.C. and Yılmaz, Y. (1981). Tethyan evolution of Turkey: A plate tectonic approach. Tectonophysics. 75: 181-241.

Şengün, F., Zack, T., Dunkl, I. (2020). Provenance of detrital rutiles from the Jurassic sandstones in the Central Sakarya Zone, NW Turkey: U-Pb ages and trace element geochemistry. Geochemistry, In Press.

Şengün, F. and Koralay, O.E. (2019). Petrography, geochemistry, and provenance of Jurassic sandstones from the Sakarya Zone, NW Turkey. Turkish Journal of Earth Sciences. 28: 1-20.

Şentürk, K. and Karaköse, C. (1979). Geology of the Central Sakarya Region. General Directorate of Mineral Research and Exploration of Turkey (MTA). [Unpublished, Report No: 6642]. [In Turkish].

Shervais, M. (1982). Ti-V plots and the petrogenesis of modern and ophiolitic lavas. Earth and Planetary Science Letters, 59: 101-118.

Schoene, B. (2014). U-Th-Pb Geochronology. Princeton University, Princeton, NJ, USA.

Slama, J. Kosler, J., Condon, D.J., Crowley, J.L., Gerdes, A., Hanchar, J.M., Horstwood, M.S.A., Morris, G.A., Nasdala, L., Norberg, N., Schaltegger, U., Schoene, N., Tubrett, M.N. and Whitehouse, M.J. (2008). Plesovice zircon - a new natural reference material for U-Pb and Hf isotopic microanalysis. Chemical Geology, 249 (1-2): 1-35.

Stampfli, G.M. and Borel, G.D. (2002). A plate tectonic model for the Paleozoic and Mesozoic constrained by dynamic plate boundaries and restored synthetic oceanic isochrones. Earth and Planetary Science Letters, 196: 17-33.

Stampfli, G.M., von Raumer, J.F., and Borel, G.D. (2002). Paleozoic evolution of pre-Variscan terranes: From Gondwana to the Variscan collision. In Martínez Catalán, J.R., Hatcher, R.D., Jr., Arenas, R., and Díaz García, F. (eds). Variscan-Appalachian dynamics: The building of the late Paleozoic

basement: Boulder, Colorado. Geological Society of America Special Paper, 364: 263-280.

Stampfli, G.M., (2000). Tethyan oceans. In: Bozkurt, E., Winchester, J. A. and Piper, J. D. (eds) Tectonics and Magmatism in Turkey and the Surrounding Area. In: Bozkurt, E., Winchester, J. and Piper, J.A. (eds). Tectonics and magmatism in Turkey and the Surrounding Area. Geol. Soc. London Spec. Publ., 173, 1-23.

Sun, S.S. and McDonough, W.F. (1989). Chemical and isotopic systematics of oceanic basalts: implications for mantle composition and processes. In: Saunders, A. and Norry, M.J. (Eds.), Magmatism in the Ocean Basins. Geological Society of London Special Publication. 42: 313–345.

Tekin, U.K., Okuyucu, C. Sayit, K., Bedi, Y., Noble, P.J., Krystyn, L., Göncüoğlu, M.C. (2019). Integrated Radiolaria, benthic foraminifera and conodont biochronology of the pelagic Permian blocks/tectonic slices and geochemistry of associated volcanic rocks from the Mersin Mélange, southern Turkey: Implications for the Permian evolution of the northern Neotethys. Island Arc, 28(2): 1-36.

Tetiker, S., Yalçın, H., Bozkaya, Ö. and Göncüoğlu, M.C. (2015). Metamorphic evolution of the Karakaya Complex in northern Turkey based on phyllosilicate mineralogy. Mineralogy and Petrology. 109: 201-215.

Tera, F., Wasserburg, G.J. (1972). U-Th-Pb systematics in lunar highland samples from the Luna 20 and Apollo 16 missions. Earth and Planetary Science Letters, 17: 36-51.

Topuz, G., Candan, O., Okay, A.I., Quadt, A., Othman, M., Zack, T., Wang, J. (2020). Silurian anorogenic basic and acidic magmatism in Northwest Turkey: Implications for the opening of the Paleo-Tethys. Lithos, 356-357.

Topuz, G., Altherr, R., Schwarz, W.H., Dokuz, A., Meyer, H.P. (2007). Variscan amphibolite facies metamorphic rocks from the Kurtoğlu metamorphic

complex (Gümüşhane area, Eastern Pontides, Turkey). Int. J. Earth Sci., 96: 861-873.

Topuz, G., Altherr, R., Kalt, A., Satır, M., Werner, O., Schwarz, M. (2004). Aluminous granulites from the Pulur complex, NE Turkey: a case of partial melting, efficient melt extraction and crystallization. Lithos, 72: 183-207.

Turner, F.J. (1981). Metamorphic Petrology: Mineralogical, field and tectonic aspects: New York, McGraw-Hill.

Uğurcan, O.G., Ustaömer, T., Gerdes, A. (2019). Cambrian-Early Ordovician magmatism, Mid-Late Paleozoic Sedimentation and Early Carboniferous Metamorphism in the Central Sakarya Terrane; Sakarya Zone, NW Turkey. International Earth Science Colloquium on the Aegean Region Abstracts, 11.

Ustaömer, P.A., Ustaömer, T. and Robertson, A.H.F. (2012). Ion Probe U-Pb Dating of the Central Sakarya Basement: A peri-Gondwana Terrane Intruded by Late Lower Carboniferous Subduction/Collision-related Granitic Rocks. Turkish Journal of Earth Sciences. 21: 905-932.

Villemant, B., Jaffrezic, H., Joron, J.L. and Treuil, M. (1981). Distribution Coefficients of Major and Trace-Elements - Fractional Crystallization in the Alkali Basalt Series of Chaine-Des-Puys (Massif Central, France). Geochimica et Cosmochimica Acta, 45(11): 1,997-2,016.

Wiedenbeck, M., Alle, P., Corfu, F., Griffin, W.L., Meier, M., Oberli, F., Quadt, A., Roddick, J.C. and Spiegel, W. (1995). Three natural zircon standards for U-Th-Pb, Lu-Hf, trace element and REE analyses. Geostandards Newsletter, 19: 1-23.

Wilshire, H.G. (1984). Mantle metasomatism: The REE story. Geology, 12: 395-398.

Winchester, J.A. and Floyd, P.A. (1977). Geochemical discrimination of different magma series and their differentiation products using immobile elements. Chemical Geology, 20: 325-343.

Winter J.D. (2014). Principles of Igneous and Metamorphic Petrology. 2nd Edition. New Jersey, USA: Pearson Education, Inc.

Wood, D.A. (1980). The application of a TH-Hf-Ta diagram to problems of tectonomagmatic classification and to establishing the nature of crustal contamination of basaltic lavas of the British Tertiary Volcanic Province. Earth and Planetary Science Letters, 50: 11-30.

Wood, D.A., Gibson, I.L., and Thompson, R.N. (1976). Elemental mobility during zeolite facies metamorphism of the Tertiary basalts of eastern Iceland. Contributions to Mineralogy and Petrology, 55(3): 241-254.

Yaşar, I.D., Sayit, K. and Göncüoğlu, M.C. (2019). Mafic and ultramafic rocks within the Söğüt Metamorphics of the Sakarya Composite Terrane, NW Eskişehir, Turkey: Preliminary field and petrological findings. International Earth Science Colloquium on the Aegean Region Abstracts, 13.

Yıldız, A., Kibici, Y., Bağcı, M., Dumlupunar, İ., Kocabaş, C. and Aritan, A.E. (2015). Petrogenesis of the post-collisional Eocene volcanic rocks from the Central Sakarya Zone (Northwestern Anatolia, Turkey): Implications for source characteristics, magma evolution, and tectonic setting. Arabian Journal of Geosciences. 8: 11239–11260.

Yılmaz, Y. (1976). Relict Pyroxenes of Söğüt Metabasite. İstanbul University Earth Sciences. 41(1-4): 27–33.

Yılmaz, Y. (1977). Petrogenetic Evolution of the Old Basement Complex in the Bilecik-Söğüt Area. İstanbul University. [Unpublished, Habilitation Thesis]. [In Turkish with English Abstract].

Yılmaz, Y. (1979). Polyphase Metamorphism of the Söğüt-Bilecik Region, and their tectonic implications. Bulletin of the Geological Society of Turkey. 22: 85-100. [In Turkish with English Abstract].

Yılmaz, Y. (1981). Tectonic Evolution of the Southern Margin of the Sakarya Continent, NW Turkey. İstanbul University Earth Sciences, 1/2: 33-52. [In Turkish with English Abstract].

Yılmaz, Y. (1985). Orta Sakarya Bölgesi Eski Temel ve Ofiyolit Sorunu. Sixth Colloquim on Geology of the Aegean Region. 699-707 [In Turkish with English Abstract].

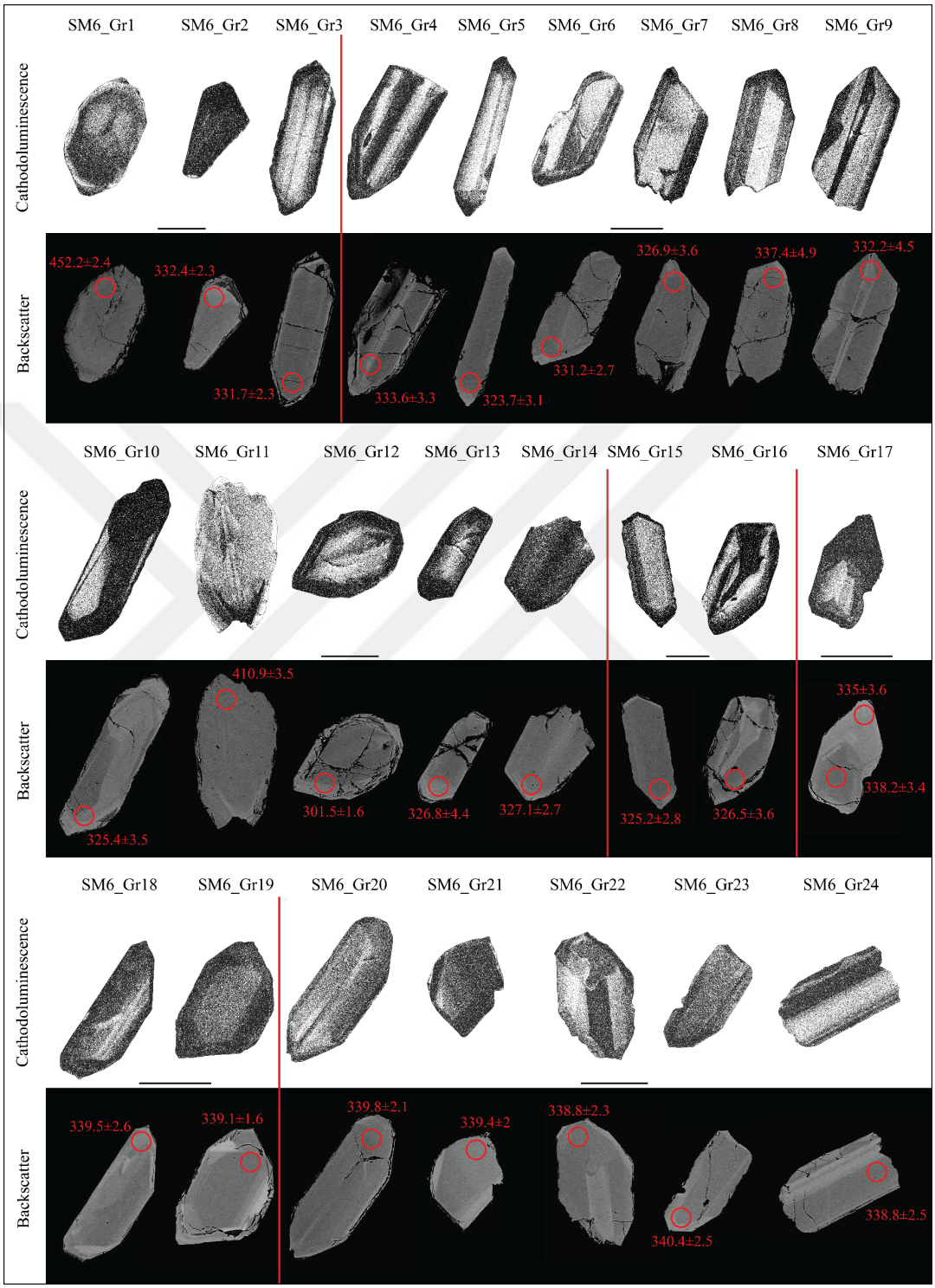
Yılmaz, Y. (1990). Allochthonous Terranes in the Tethyan Middle East: Anatolia and the Surrounding Regions. Philosophical Transactions of the Royal Society, London., Series A. 331: 611-624.

APPENDICES

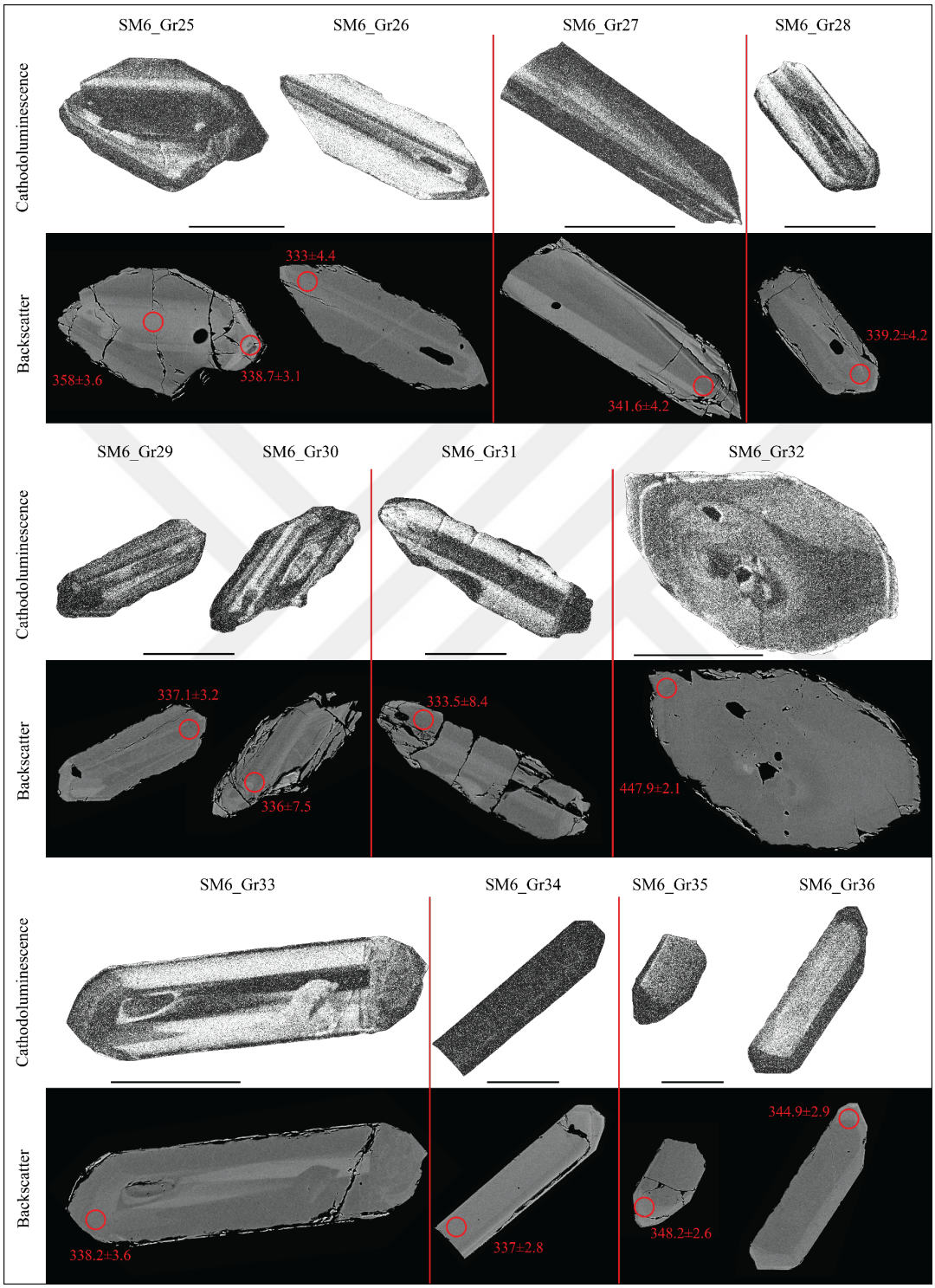
A. ZIRCON PLATES

In this appendix, the analyzed zircon grains of each sample are presented with cathodoluminescence (CL) and back-scattered scanning electron microscopy (SEM) photographs. The CL photographs are presented with a white background as to reveal the internal structures of the zircons grains whereas the SEM photographs are presented with a black background as to reveal the inclusions and fractures of the zircon grains. Each scale bar on the plates indicates 100 μm, whereas the spot marks of the analysis locations are 12 μm in diameter. Presented ages are $^{206}Pb/^{238}U$ ages of each spot.

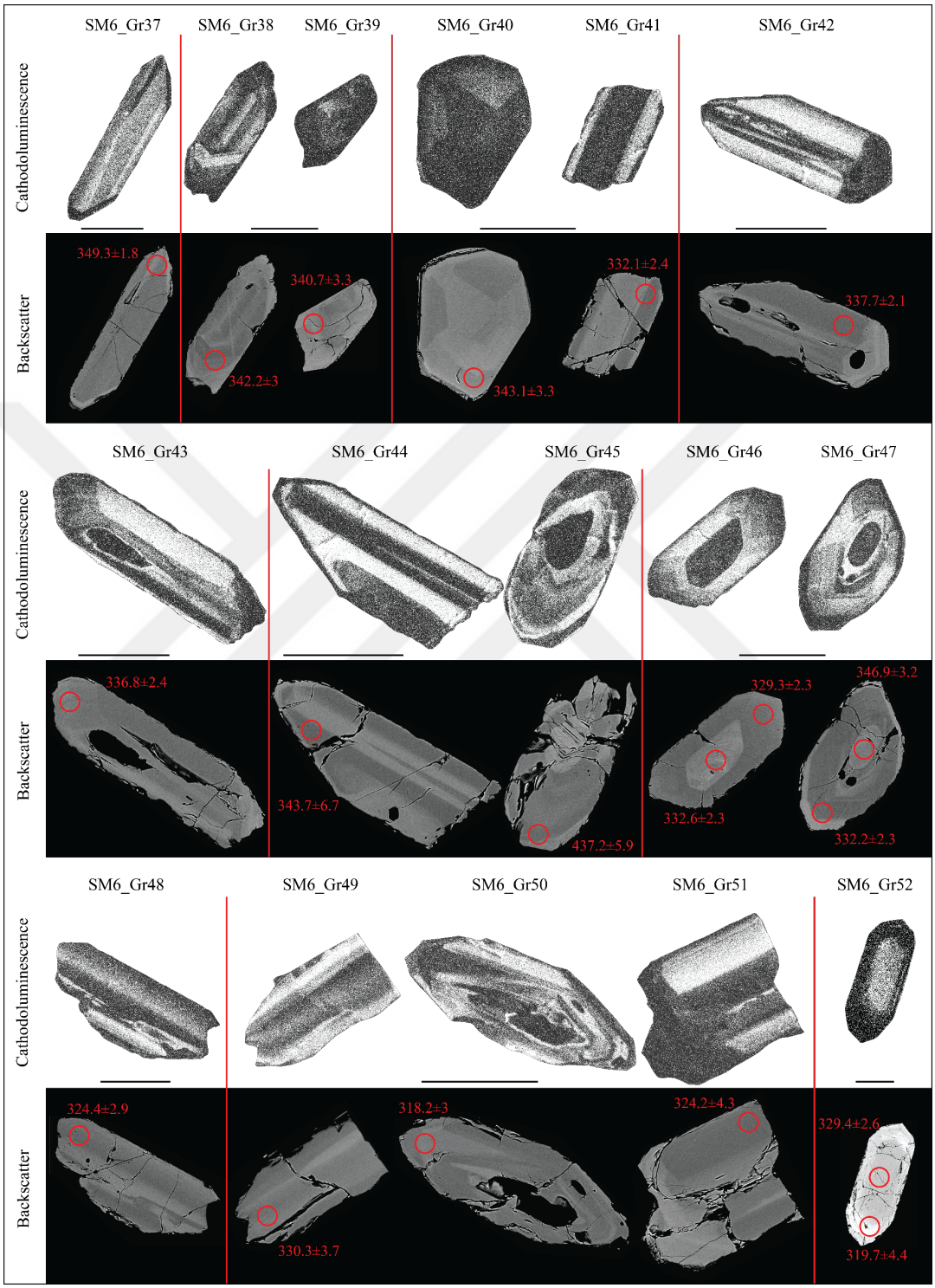
SM6 PLATE I


SM6_Gr1
SM6_Gr2
SM6_Gr3
SM6_Gr4
SM6_Gr5
SM6_Gr6
SM6_Gr7
SM6_Gr8
SM6_Gr9
Cathodoluminescence
Backscatter
452.2±2.4
332.4±2.3
331.7±2.3
333.6±3.3
323.7±3.1
331.2±2.7
326.9±3.6
337.4±4.9
332.2±4.5
SM6_Gr10
SM6_Gr11
SM6_Gr12
SM6_Gr13
SM6_Gr14
SM6_Gr15
SM6_Gr16
SM6_Gr17
Cathodoluminescence
Backscatter
410.9±3.5
325.4±3.5
301.5±1.6
326.8±4.4
327.1±2.7
325.2±2.8
326.5±3.6
335±3.6
338.2±3.4
SM6_Gr18
SM6_Gr19
SM6_Gr20
SM6_Gr21
SM6_Gr22
SM6_Gr23
SM6_Gr24
Cathodoluminescence
Backscatter
339.5±2.6
339.1±1.6
339.8±2.1
339.4±2
338.8±2.3
340.4±2.5
338.8±2.5

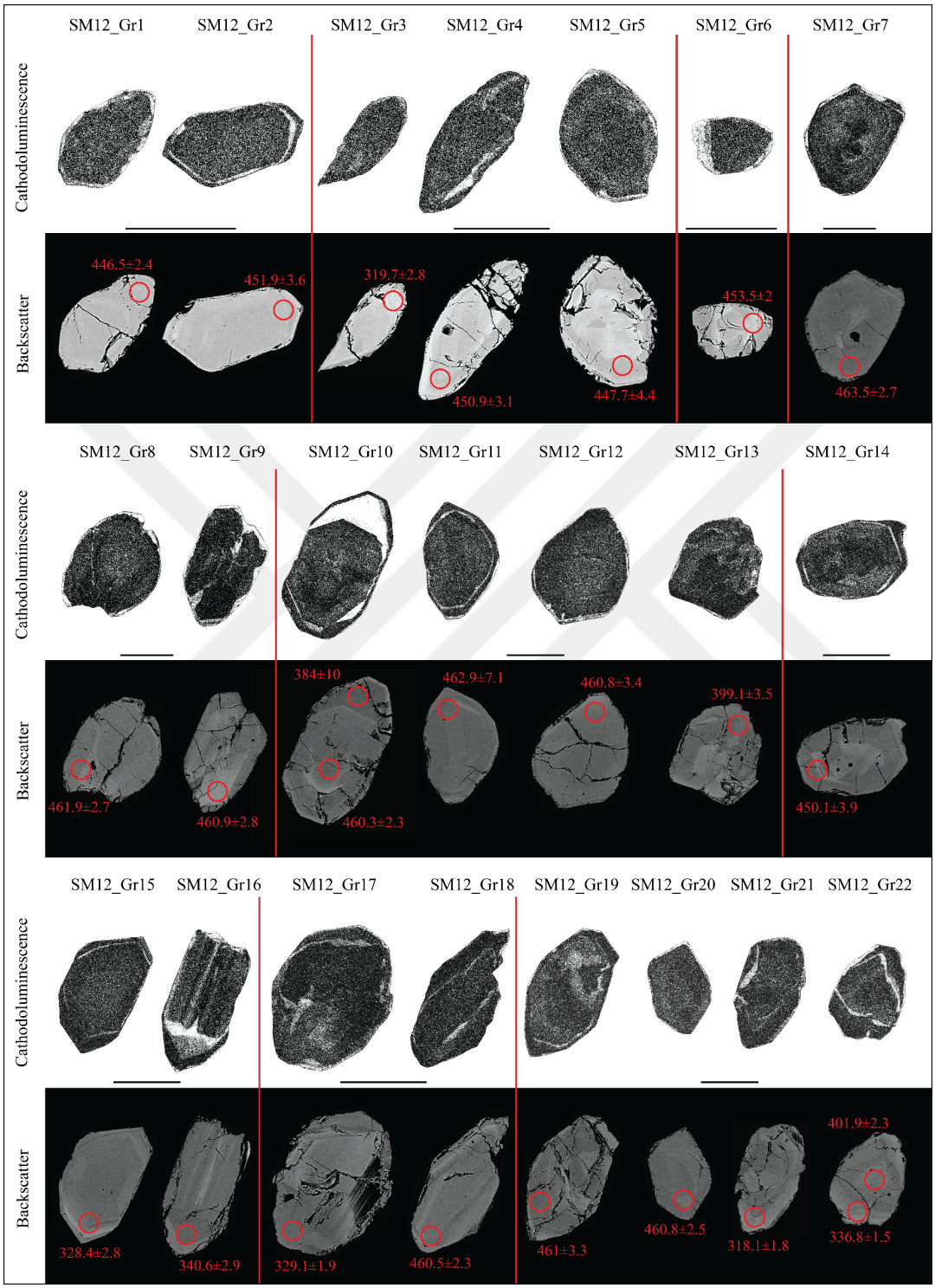
SM6 PLATE II


SM6_Gr25
SM6_Gr26
SM6_Gr27
SM6_Gr28
Cathodoluminescence
Backscatter
333±4.4
358±3.6
338.7±3.1
341.6±4.2
339.2±4.2
SM6_Gr29
SM6_Gr30
SM6_Gr31
SM6_Gr32
Cathodoluminescence
Backscatter
337.1±3.2
336±7.5
333.5±8.4
447.9±2.1
SM6_Gr33
SM6_Gr34
SM6_Gr35
SM6_Gr36
Cathodoluminescence
Backscatter
338.2±3.6
337±2.8
348.2±2.6
344.9±2.9

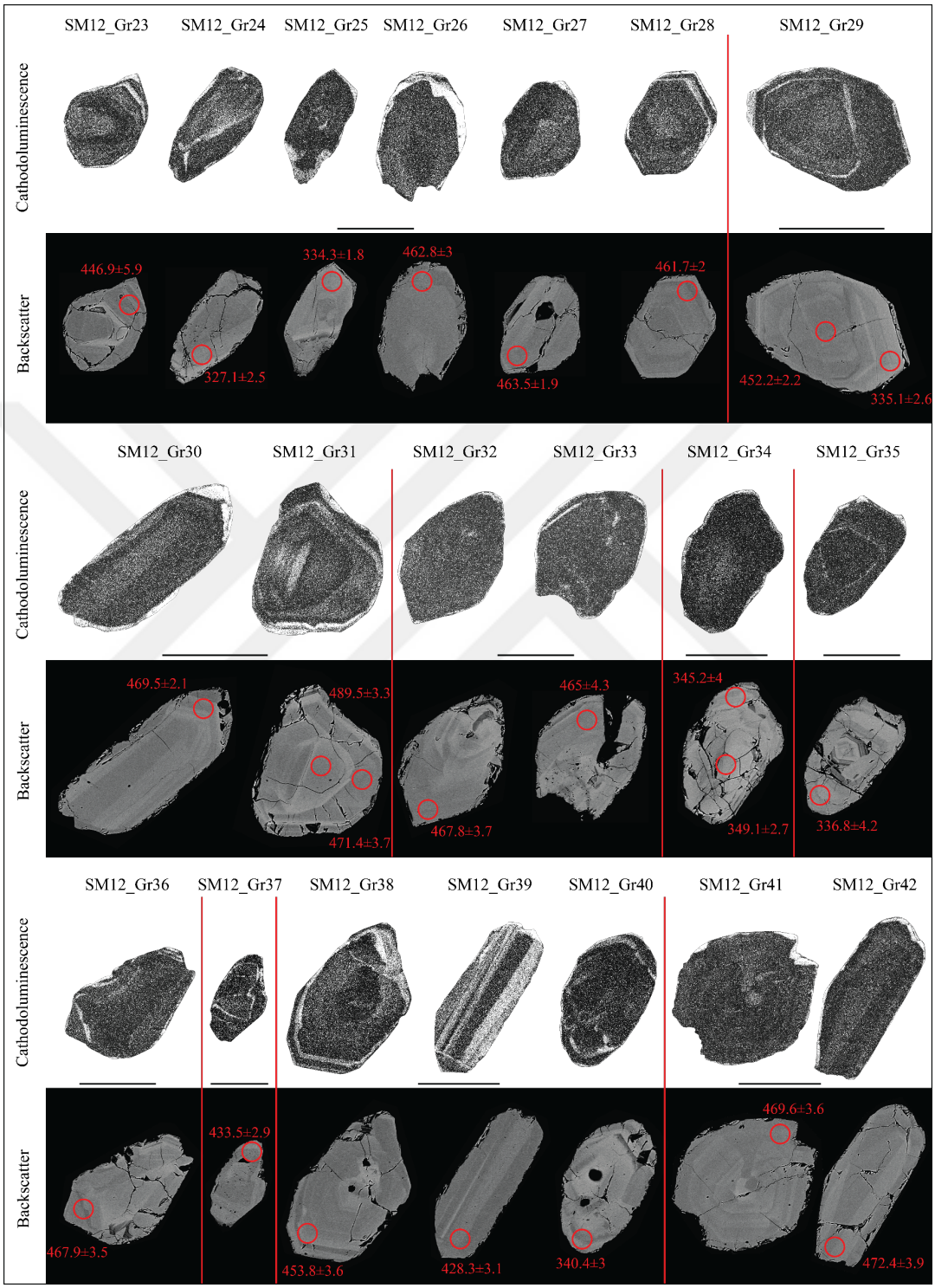
SM6 PLATE III



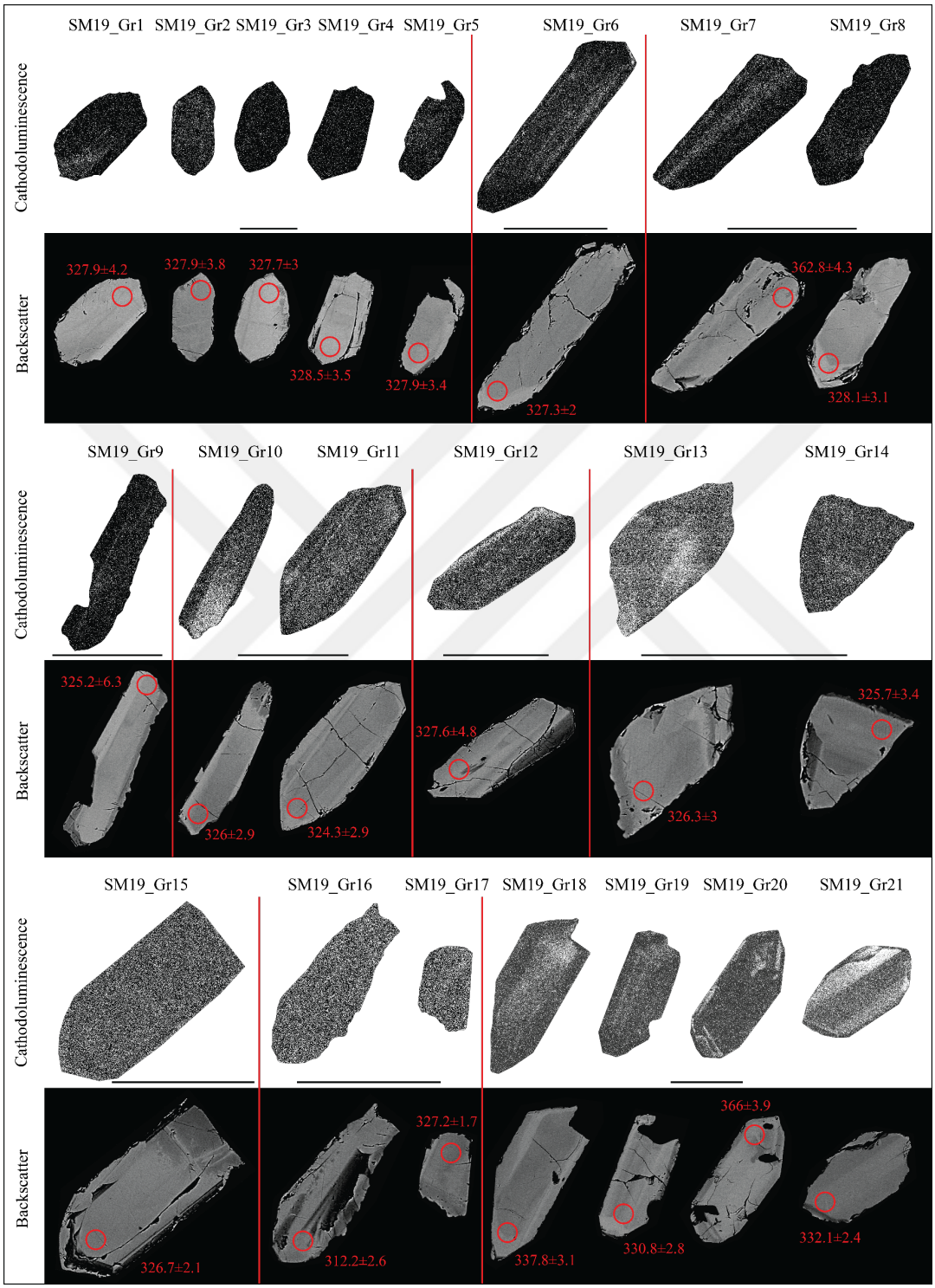
SM12 PLATE I


SM12_Gr1
SM12_Gr2
SM12_Gr3
SM12_Gr4
SM12_Gr5
SM12_Gr6
SM12_Gr7
Cathodoluminescence
Backscatter
446.5±2.4
451.9±3.6
319.7±2.8
450.9±3.1
447.7±4.4
453.5±2
463.5±2.7
SM12_Gr8
SM12_Gr9
SM12_Gr10
SM12_Gr11
SM12_Gr12
SM12_Gr13
SM12_Gr14
Cathodoluminescence
Backscatter
461.9±2.7
460.9±2.8
384±10
460.3±2.3
462.9±7.1
460.8±3.4
399.1±3.5
450.1±3.9
SM12_Gr15
SM12_Gr16
SM12_Gr17
SM12_Gr18
SM12_Gr19
SM12_Gr20
SM12_Gr21
SM12_Gr22
Cathodoluminescence
Backscatter
328.4±2.8
340.6±2.9
329.1±1.9
460.5±2.3
461±3.3
460.8±2.5
318.1±1.8
401.9±2.3
336.8±1.5

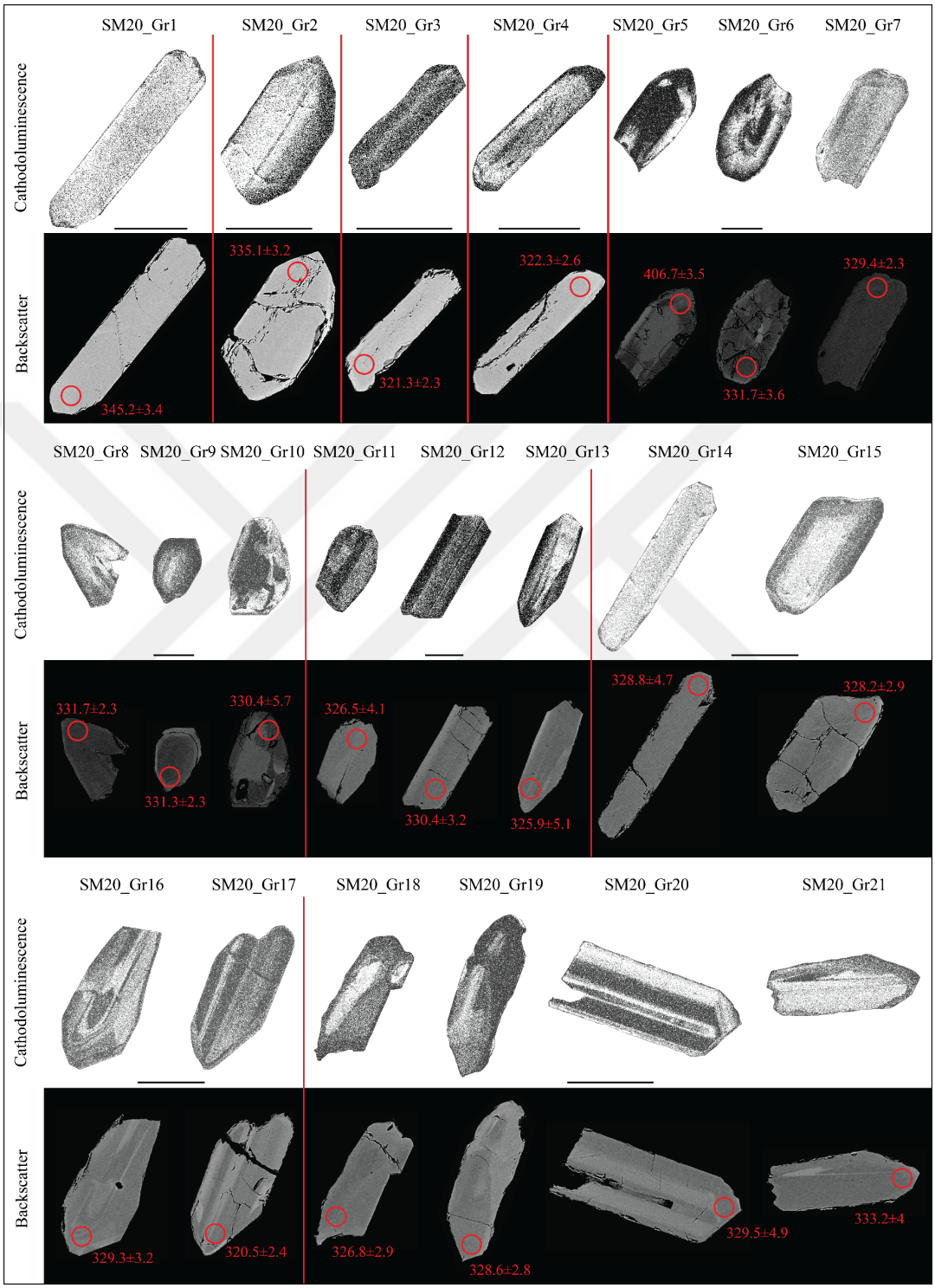
SM12 PLATE II



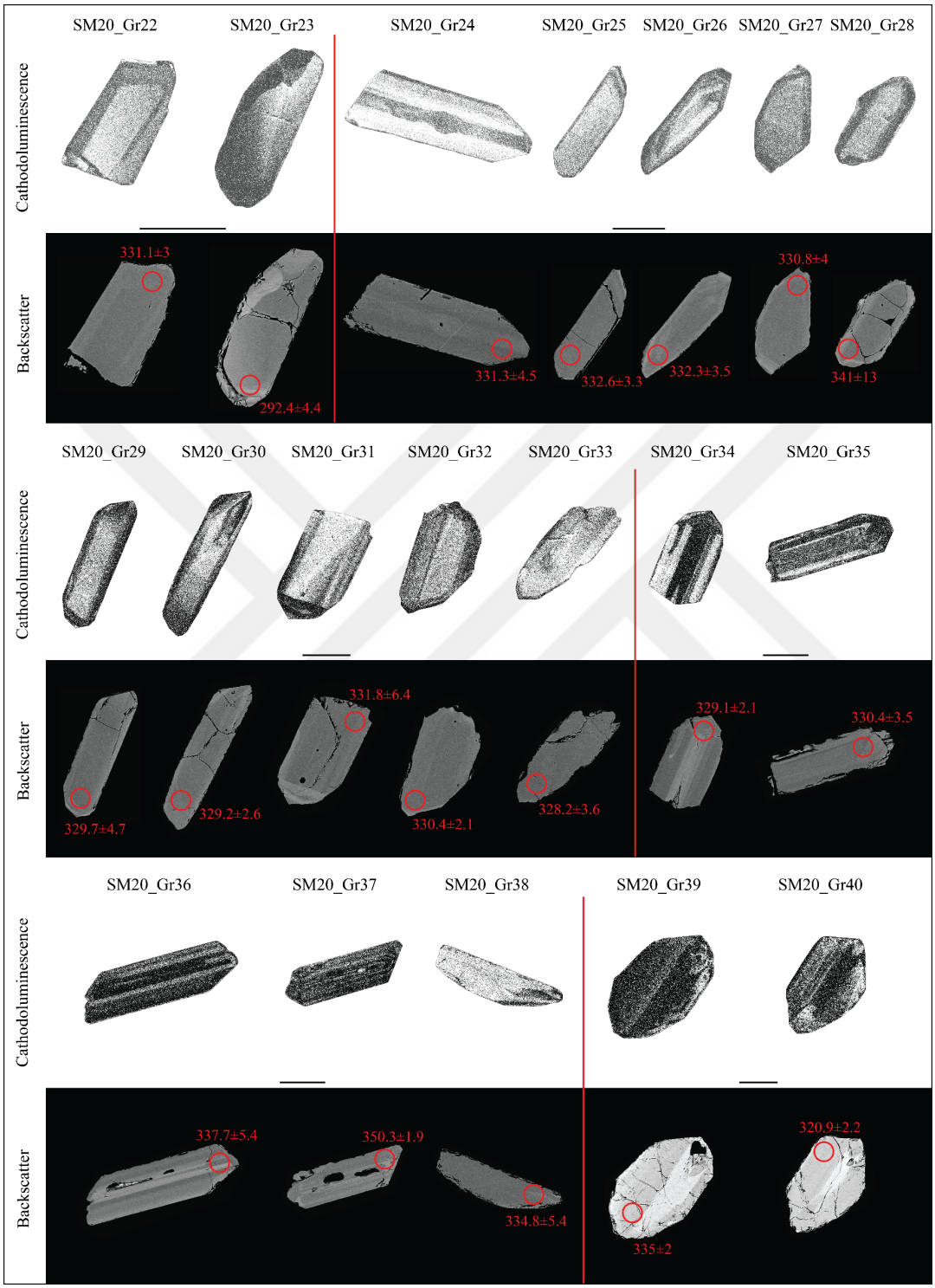
SM19 PLATE


SM19_Gr1
SM19_Gr2
SM19_Gr3
SM19_Gr4
SM19_Gr5
SM19_Gr6
SM19_Gr7
SM19_Gr8
Cathodoluminescence
Backscatter
327.9±4.2
327.9±3.8
327.7±3
328.5±3.5
327.9±3.4
327.3±2
362.8±4.3
328.1±3.1
SM19_Gr9
SM19_Gr10
SM19_Gr11
SM19_Gr12
SM19_Gr13
SM19_Gr14
Cathodoluminescence
Backscatter
325.2±6.3
326±2.9
324.3±2.9
327.6±4.8
326.3±3
325.7±3.4
SM19_Gr15
SM19_Gr16
SM19_Gr17
SM19_Gr18
SM19_Gr19
SM19_Gr20
SM19_Gr21
Cathodoluminescence
Backscatter
326.7±2.1
312.2±2.6
327.2±1.7
337.8±3.1
330.8±2.8
366±3.9
332.1±2.4

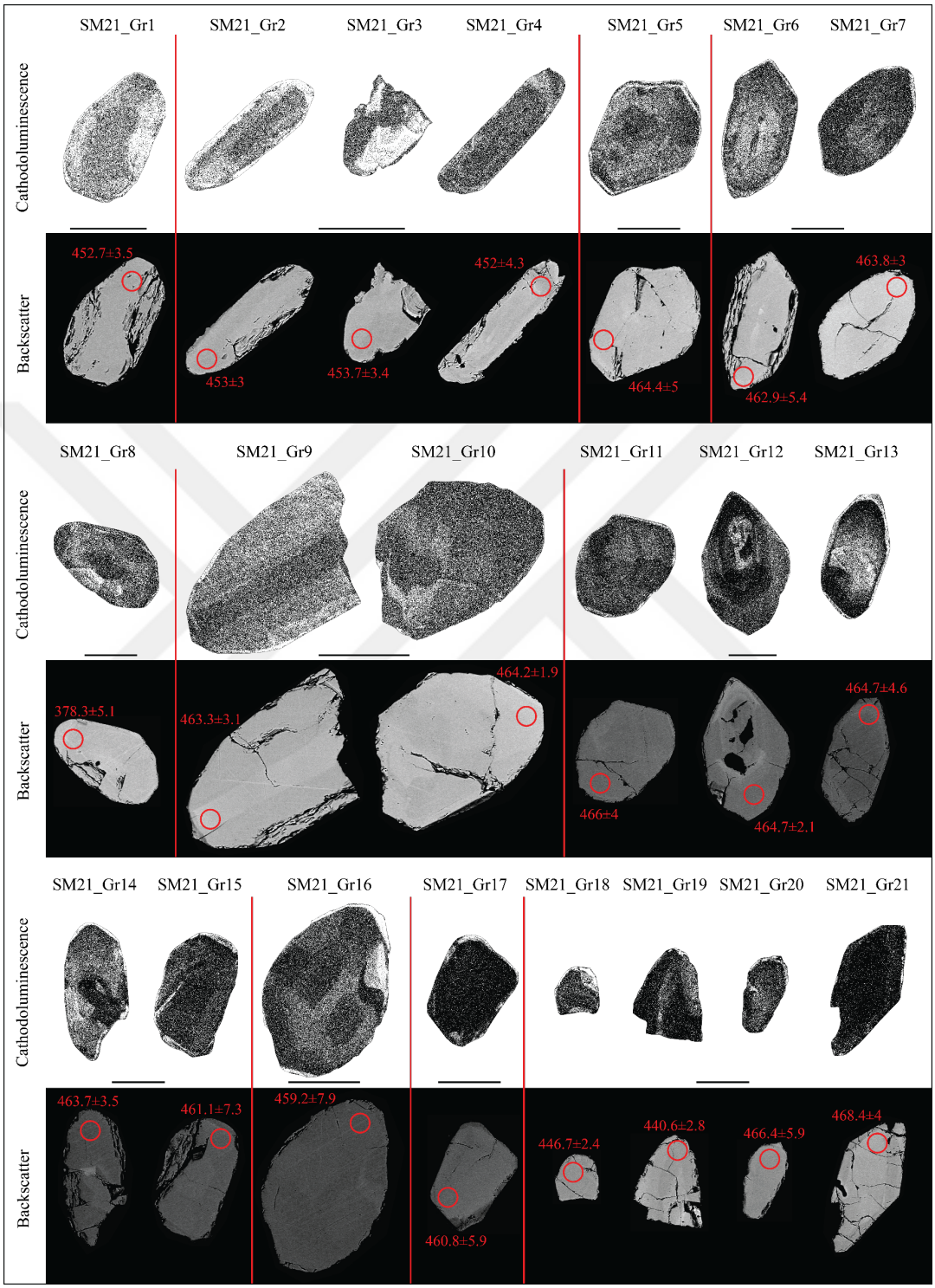
SM20 PLATE I


SM20_Gr1
SM20_Gr2
SM20_Gr3
SM20_Gr4
SM20_Gr5
SM20_Gr6
SM20_Gr7
Cathodoluminescence
Backscatter
345.2±3.4
335.1±3.2
321.3±2.3
322.3±2.6
406.7±3.5
331.7±3.6
329.4±2.3
SM20_Gr8
SM20_Gr9
SM20_Gr10
SM20_Gr11
SM20_Gr12
SM20_Gr13
SM20_Gr14
SM20_Gr15
331.7±2.3
331.3±2.3
330.4±5.7
326.5±4.1
330.4±3.2
325.9±5.1
328.8±4.7
328.2±2.9
SM20_Gr16
SM20_Gr17
SM20_Gr18
SM20_Gr19
SM20_Gr20
SM20_Gr21
329.3±3.2
320.5±2.4
326.8±2.9
328.6±2.8
329.5±4.9
333.2±4

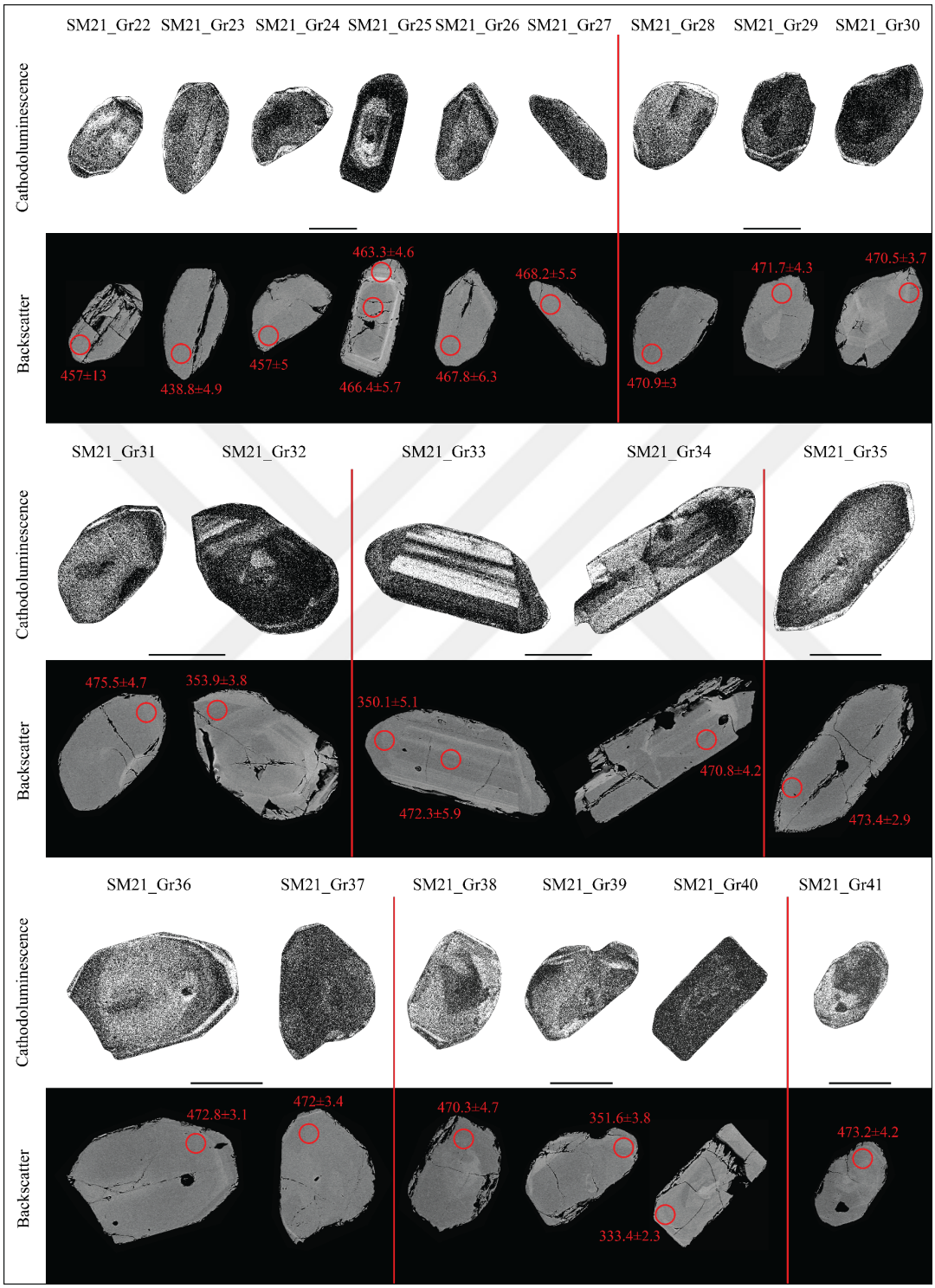
SM20 PLATE II



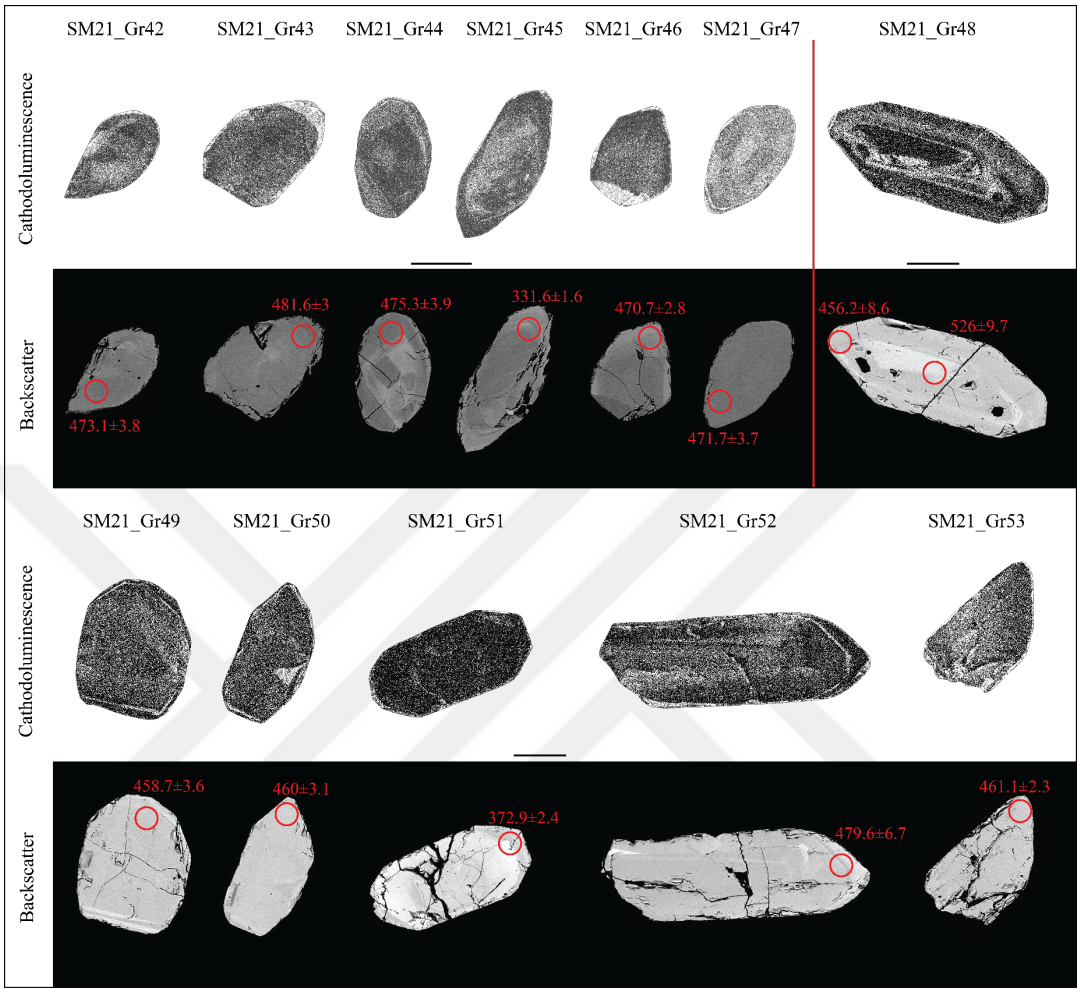
SM21 PLATE I


SM21_Gr1
SM21_Gr2
SM21_Gr3
SM21_Gr4
SM21_Gr5
SM21_Gr6
SM21_Gr7
Cathodoluminescence
Backscatter
452.7±3.5
453±3
453.7±3.4
452±4.3
464.4±5
462.9±5.4
463.8±3
SM21_Gr8
SM21_Gr9
SM21_Gr10
SM21_Gr11
SM21_Gr12
SM21_Gr13
Cathodoluminescence
Backscatter
378.3±5.1
463.3±3.1
464.2±1.9
466±4
464.7±2.1
464.7±4.6
SM21_Gr14
SM21_Gr15
SM21_Gr16
SM21_Gr17
SM21_Gr18
SM21_Gr19
SM21_Gr20
SM21_Gr21
Cathodoluminescence
Backscatter
463.7±3.5
461.1±7.3
459.2±7.9
460.8±5.9
446.7±2.4
440.6±2.8
466.4±5.9
468.4±4

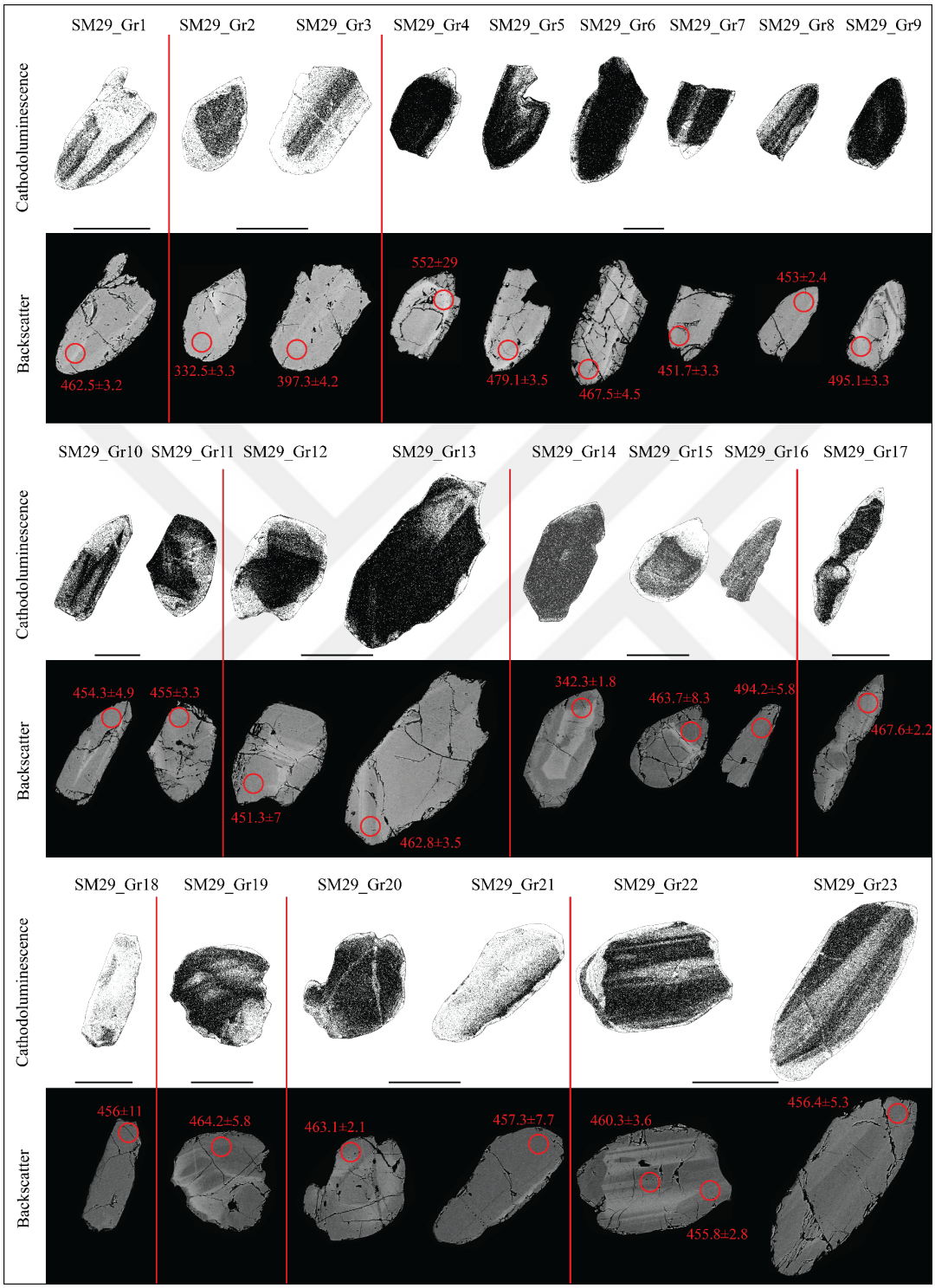
SM21 PLATE II



SM21 PLATE III



SM29 PLATE


SM29_Gr1
SM29_Gr2
SM29_Gr3
SM29_Gr4
SM29_Gr5
SM29_Gr6
SM29_Gr7
SM29_Gr8
SM29_Gr9
Cathodoluminescence
Backscatter
462.5±3.2
332.5±3.3
397.3±4.2
552±29
479.1±3.5
467.5±4.5
451.7±3.3
453±2.4
495.1±3.3
SM29_Gr10
SM29_Gr11
SM29_Gr12
SM29_Gr13
SM29_Gr14
SM29_Gr15
SM29_Gr16
SM29_Gr17
454.3±4.9
455±3.3
451.3±7
462.8±3.5
342.3±1.8
463.7±8.3
494.2±5.8
467.6±2.2
SM29_Gr18
SM29_Gr19
SM29_Gr20
SM29_Gr21
SM29_Gr22
SM29_Gr23
456±11
464.2±5.8
463.1±2.1
457.3±7.7
460.3±3.6
455.8±2.8
456.4±5.3

B. U-Pb LA-MC-ICP-MS RESULTS OF AMPHIBOLITES

In this appendix, the LA-MC-ICP-MS measurement results and the calculated ages from the zircon grains of amphibolite samples are presented. The blue, yellow, grey highlighted rows indicate the extracted; highest age, lowest age, discordant data respectively, from weighted mean age calculations. Furthermore, orange highlighted rows indicate a differentiated group of the measurements from the same sample (i.e. Carboniferous measurements from the rims of the zircons in an Ordovician sample).

ID	U (ppm)	Th (ppm)	Pb (ppm)	Th/U	$^{207}Pb/^{235}U$	2σ	$^{206}Pb/^{238}U$	2σ	$^{207}Pb/^{206}Pb$	2σ	$^{207}Pb/^{235}U$ Age (Ma)	$^{206}Pb/^{238}U$ Age (Ma)	$^{207}Pb/^{206}Pb$ Age (Ma)	Concordance
							SM 6							
~~SM6_Gr1~~	~~441~~	~~137~~	~~28.2~~	~~0.29~~	~~0.5608~~	~~0.0054~~	~~0.07268~~	~~0.0004~~	~~0.05513~~	~~0.00034~~	~~452.3 ± 3.6~~	~~452.2 ± 2.4~~	~~416 ± 15~~	~~100.0~~
SM6_Gr2	1216	985	165.1	0.79	0.3866	0.0043	0.05292	0.00037	0.05261	0.00038	331.8 ± 3.1	332.4 ± 2.3	311 ± 16	100.2
SM6_Gr3	292.3	111	17.68	0.36	0.3864	0.0063	0.05281	0.00037	0.04932	0.00053	332.4 ± 4.6	331.7 ± 2.3	157 ± 25	99.8
SM6_Gr4	440	57.6	10.31	0.13	0.3807	0.0064	0.05312	0.00054	0.05	0.00061	328.9 ± 4.8	333.6 ± 3.3	189 ± 29	101.4
SM6_Gr5	1137	691	96.9	0.60	0.3751	0.0071	0.0515	0.00051	0.05246	0.00046	323.4 ± 5.2	323.7 ± 3.1	305 ± 21	100.1
SM6_Gr6	342	61.7	9.04	0.18	0.384	0.0065	0.05272	0.00044	0.04966	0.00068	329.8 ± 4.8	331.2 ± 2.7	173 ± 32	100.4
SM6_Gr7	599	241	35.1	0.40	0.3765	0.0057	0.05202	0.00058	0.05043	0.00088	324.4 ± 4.2	326.9 ± 3.6	210 ± 42	100.8
SM6_Gr8	405.1	103.8	15.75	0.25	0.404	0.018	0.05374	0.0008	0.0487	0.0016	344 ± 13	337.4 ± 4.9	126 ± 77	98.1
SM6_Gr9	971	711.7	99.7	0.72	0.3889	0.0093	0.05288	0.00073	0.05295	0.00076	333.5 ± 6.8	332.2 ± 4.5	325 ± 33	99.6
SM6_Gr10	1459	466	66.7	0.31	0.3811	0.0057	0.05178	0.00057	0.05254	0.00064	327.8 ± 4.2	325.4 ± 3.5	308 ± 27	99.3
~~SM6_Gr11~~	~~150.5~~	~~104.2~~	~~19.82~~	~~0.68~~	~~0.513~~	~~0.018~~	~~0.06582~~	~~0.00058~~	~~0.0514~~	~~0.0015~~	~~420 ± 12~~	~~410.9 ± 3.5~~	~~247 ± 68~~	~~97.8~~
~~SM6_Gr12~~	~~452~~	~~63.2~~	~~9.28~~	~~0.14~~	~~0.3514~~	~~0.0056~~	~~0.04788~~	~~0.00027~~	~~0.04886~~	~~0.00092~~	~~305.7 ± 4.2~~	~~301.5 ± 1.6~~	~~136 ± 44~~	~~98.6~~
SM6_Gr13	1259	167.4	25.2	0.13	0.3837	0.0059	0.052	0.00072	0.0506	0.0013	329.7 ± 4.3	326.8 ± 4.4	215 ± 59	99.1
SM6_Gr14	668	354	55.2	0.53	0.3865	0.0067	0.05205	0.00045	0.05246	0.00047	331.7 ± 4.9	327.1 ± 2.7	305 ± 21	98.6
SM6_Gr15	431	280	46.7	0.64	0.3819	0.0055	0.05175	0.00046	0.05252	0.00043	328.4 ± 4.1	325.2 ± 2.8	307 ± 19	99.0
SM6_Gr16	249	55.9	8.1	0.22	0.376	0.012	0.05195	0.00058	0.04915	0.00083	324 ± 8.5	326.5 ± 3.6	150 ± 40	100.8
SM6_Gr17a	150.3	44.7	7.02	0.29	0.385	0.011	0.05326	0.00056	0.04893	0.00067	330.3 ± 7.8	335 ± 3.6	139 ± 32	101.4
SM6_Gr17b	1677	214.2	32.75	0.13	0.3924	0.0041	0.05387	0.00055	0.05126	0.00075	336 ± 3	338.2 ± 3.4	247 ± 35	100.7
SM6_Gr18	365	173.8	27.1	0.48	0.3931	0.0088	0.05408	0.00043	0.05014	0.00089	336.5 ± 6.5	339.5 ± 2.6	197 ± 42	100.9
SM6_Gr19	293	82.7	12.95	0.28	0.3968	0.0049	0.05402	0.00026	0.04951	0.00055	339.2 ± 3.6	339.1 ± 1.6	166 ± 26	100.0
SM6_Gr20	508	204.6	31.9	0.40	0.3966	0.0053	0.05413	0.00034	0.05076	0.00059	340 ± 4	339.8 ± 2.1	225 ± 28	99.9
SM6_Gr21	579	243	38.1	0.43	0.3979	0.0035	0.05406	0.00033	0.05061	0.00051	340.1 ± 2.5	339.4 ± 2	218 ± 24	99.8
SM6_Gr22	423	67.3	10.58	0.16	0.4004	0.0043	0.05396	0.00038	0.05016	0.00058	341.8 ± 3.1	338.8 ± 2.3	196 ± 27	99.1
SM6_Gr23	1191	755	119.6	0.65	0.3997	0.0037	0.05422	0.00041	0.05271	0.00022	341.3 ± 2.7	340.4 ± 2.5	318 ± 10	99.7
SM6_Gr24	338	158	26.2	0.42	0.3984	0.0056	0.05396	0.00041	0.05056	0.00052	340.3 ± 4.1	338.8 ± 2.5	216 ± 25	99.6
SM6_Gr25a	1419	1417	215.8	1.08	0.3951	0.0043	0.05394	0.0005	0.05267	0.00018	338.4 ± 3.1	338.7 ± 3.1	316.3 ± 8.6	100.1
SM6_Gr25b	1038.6	189.5	34.04	0.19	0.4222	0.0054	0.0571	0.00059	0.05112	0.00072	358 ± 3.8	358 ± 3.6	239 ± 34	100.0
~~SM6_Gr26~~	~~882~~	~~966~~	~~163.2~~	~~1.15~~	~~0.476~~	~~0.011~~	~~0.05303~~	~~0.00072~~	~~0.05153~~	~~0.00077~~	~~395.3 ± 7.9~~	~~333 ± 4.4~~	~~255 ± 36~~	~~84.2~~
SM6_Gr27	349.4	111.1	17.36	0.33	0.394	0.01	0.05443	0.00068	0.0501	0.0011	337.4 ± 7.4	341.6 ± 4.2	193 ± 51	101.2
SM6_Gr28	428	219	33.2	0.51	0.3908	0.0064	0.05404	0.00068	0.05064	0.00053	334.6 ± 4.6	339.2 ± 4.2	219 ± 25	101.4
SM6_Gr29	277.5	147.2	24.62	0.53	0.3894	0.0073	0.05369	0.00052	0.0505	0.00069	333.7 ± 5.3	337.1 ± 3.2	213 ± 33	101.0
SM6_Gr30	113.7	25.7	4.72	0.23	0.402	0.021	0.0535	0.0012	0.0489	0.0012	343 ± 15	336 ± 7.5	139 ± 59	98.0
SM6_Gr31	79.9	22.5	3.29	0.27	0.384	0.032	0.0531	0.0014	0.0487	0.0014	329 ± 23	333.5 ± 8.4	125 ± 66	101.4
~~SM6_Gr32~~	~~360~~	~~105.2~~	~~22.06~~	~~0.30~~	~~0.5543~~	~~0.0051~~	~~0.07195~~	~~0.00034~~	~~0.05293~~	~~0.00077~~	~~447.6 ± 3.4~~	~~447.9 ± 2.1~~	~~315 ± 35~~	~~100.1~~
SM6_Gr33	280	79.8	13.72	0.28	0.389	0.0073	0.05387	0.00059	0.04999	0.00087	333.5 ± 5.3	338.2 ± 3.6	189 ± 41	101.4

ID	U (ppm)	Th (ppm)	Pb (ppm)	Th/U	$^{207}Pb/^{235}U$	2σ	$^{206}Pb/^{238}U$	2σ	$^{207}Pb/^{206}Pb$	2σ	$^{207}Pb/^{235}U$ Age (Ma)	$^{206}Pb/^{238}U$ Age (Ma)	$^{207}Pb/^{206}Pb$ Age (Ma)	Concordance
SM6_Gr34	496	227	33.7	0.45	0.3963	0.0059	0.05368	0.00046	0.04971	0.00057	339.1 ± 4.4	337 ± 2.8	175 ± 27	99.4
SM6_Gr35	829	257	41.8	0.31	0.4076	0.0053	0.0555	0.00043	0.05042	0.00059	347.4 ± 3.8	348.2 ± 2.6	207 ± 28	100.2
SM6_Gr36	1061	392	60	0.37	0.4057	0.0066	0.05496	0.00047	0.05063	0.00089	345.6 ± 4.8	344.9 ± 2.9	217 ± 42	99.8
SM6_Gr37	612	385	63.2	0.60	0.4095	0.0063	0.05568	0.0003	0.05057	0.0006	348.2 ± 4.5	349.3 ± 1.8	214 ± 28	100.3
SM6_Gr38	658	98.3	16.85	0.15	0.4015	0.0093	0.05451	0.00048	0.0487	0.00088	342.5 ± 6.7	342.2 ± 3	127 ± 42	99.9
SM6_Gr39	965	171.1	30.6	0.18	0.407	0.012	0.05428	0.00054	0.049	0.0013	346.6 ± 8.4	340.7 ± 3.3	139 ± 63	98.3
SM6_Gr40	1790	881	135.1	0.51	0.3987	0.0058	0.05466	0.00055	0.05262	0.00043	340.6 ± 4.2	343.1 ± 3.3	312 ± 18	100.7
SM6_Gr41	744	755	125.8	1.05	0.3874	0.0059	0.05287	0.0004	0.05111	0.00062	332.3 ± 4.3	332.1 ± 2.4	242 ± 29	99.9
SM6_Gr42	878	107.9	16.28	0.13	0.394	0.0081	0.05313	0.00035	0.04953	0.00085	337.1 ± 5.9	337.7 ± 2.1	166 ± 40	99.0
SM6_Gr43	426	269	43.2	0.66	0.3913	0.0076	0.05363	0.00039	0.04973	0.00061	335.7 ± 5.6	336.8 ± 2.4	177 ± 29	100.3
SM6_Gr44	110.3	49	8.61	0.45	0.391	0.03	0.0548	0.0011	0.04779	0.00064	331 ± 22	343.7 ± 6.7	89 ± 31	103.8
~~**SM6_Gr45**~~	~~101.4~~	~~21.9~~	~~4.87~~	~~0.20~~	~~0.541~~	~~0.029~~	~~0.07019~~	~~0.00099~~	~~0.05202~~	~~0.00074~~	~~441 ± 19~~	~~437. 2 ± 5.9~~	~~276 ± 34~~	~~99.1~~
~~**SM6_Gr46a**~~	~~1041~~	~~375~~	~~84.7~~	~~0.35~~	~~0.5566~~	~~0.0092~~	~~0.05295~~	~~0.00037~~	~~0.04902~~	~~0.00064~~	~~448.8 ± 5.9~~	~~332.6 ± 2.3~~	~~140 ± 30~~	~~74.1~~
SM6_Gr46b	337	130	19.94	0.39	0.3761	0.0092	0.05241	0.00038	0.0488	0.0005	324.9 ± 7	329.3 ± 2.3	133 ± 24	101.4
SM6_Gr47a	889	283.2	44.6	0.31	0.3855	0.0048	0.05288	0.00038	0.0499	0.00052	330.9 ± 3.5	332.2 ± 2.3	185 ± 25	100.4
SM6_Gr47b	743	291.1	44.3	0.40	0.4019	0.0088	0.05529	0.00053	0.0508	0.001	342.9 ± 6.4	346.9 ± 3.2	227 ± 48	101.2
SM6_Gr48	401	165.1	23.42	0.41	0.3809	0.0096	0.05161	0.00047	0.04918	0.00063	327.3 ± 7	324.4 ± 2.9	154 ± 31	99.1
SM6_Gr49	593	327	44.8	0.55	0.388	0.014	0.05258	0.00061	0.049	0.0011	332.7 ± 9.9	330.3 ± 3.7	155 ± 57	99.3
SM6_Gr50	749	578	79.7	0.78	0.373	0.01	0.0506	0.00049	0.051	0.00097	321.7 ± 7.6	318.2 ± 3	235 ± 45	98.9
SM6_Gr51	137	35.6	4.83	0.26	0.381	0.023	0.05158	0.00069	0.04812	0.00065	327 ± 18	324.2 ± 4.3	100 ± 31	99.1
SM6_Gr52a	116.4	29.2	4.67	0.26	0.38	0.019	0.05086	0.00072	0.04792	0.00052	327 ± 14	319.7 ± 4.4	89 ± 24	97.8
SM6_Gr52b	3850	1531	244.2	0.42	0.4143	0.006	0.05242	0.00043	0.0503	0.0011	351.9 ± 4.3	329.4 ± 2.6	198 ± 52	93.6
								SM12						
SM12_Gr1	510	227.1	53.09	0.44	0.6086	0.0049	0.07172	0.0004	0.04705	0.00037	482.6 ± 3.1	446.5 ± 2.4	46 ± 17	92.5
SM12_Gr2	296	151.3	32.27	0.51	0.5594	0.0099	0.07261	0.0006	0.0526	0.0012	450.9 ± 6.4	451.9 ± 3.6	303 ± 56	100.2
SM12_Gr3	900	182.3	28.24	0.20	0.3762	0.0041	0.05084	0.00046	0.04957	0.00099	342.2 ± 3	319.7 ± 2.8	168 ± 47	98.6
SM12_Gr4	693	446.5	87.5	0.65	0.5556	0.0058	0.07246	0.00052	0.05555	0.00029	448.6 ± 3.8	450.9 ± 3.1	434 ± 12	100.5
SM12_Gr5	420.7	207.5	44.29	0.50	0.5561	0.0086	0.07192	0.00073	0.05525	0.00065	448.9 ± 5.6	447.7 ± 4.4	429 ± 30	99.7
SM12_Gr6	1044	678	151.8	0.66	0.5678	0.0037	0.07288	0.00033	0.05561	0.00021	456.6 ± 2.4	453.5 ± 2	436.4 ± 8.3	99.3
SM12_Gr7	705.7	305.4	61.45	0.43	0.5791	0.0061	0.07456	0.00046	0.05618	0.00044	463.8 ± 3.9	463.5 ± 2.7	459 ± 17	99.9
SM12_Gr8	780	287	59.63	0.36	0.5802	0.0051	0.07428	0.00044	0.05533	0.00039	464.5 ± 3.3	461.9 ± 2.7	424 ± 17	99.4
SM12_Gr9	3898	3549	752	0.90	0.5843	0.0051	0.07411	0.00047	0.05638	0.00034	467.2 ± 3.2	460.9 ± 2.8	467 ± 13	98.7
~~**SM12_Gr10_rm**~~	~~23.46~~	~~0.03~~	~~3.63~~	~~1.11~~	~~1.301~~	~~0.081~~	~~0.0613~~	~~0.0017~~	~~0.05441~~	~~0.00026~~	~~840 ± 35~~	~~384 ± 10~~	~~390 ± 11~~	~~45.7~~
SM12_Gr10_cr	524	332	72	0.63	0.5767	0.005	0.07401	0.00038	0.05541	0.00025	462.2 ± 3.2	460.3 ± 2.3	431 ± 11	99.6
SM12_Gr11	867	361.8	74.8	0.42	0.5792	0.0092	0.0744	0.0012	0.05592	0.00029	463.8 ± 5.9	462.9 ± 7.1	449 ± 11	99.8
SM12_Gr12	711	322.9	73.3	0.45	0.5748	0.0061	0.0741	0.00056	0.0556	0.0002	461 ± 3.9	460.8 ± 3.4	436.3 ± 7.9	100.0

ID	U (ppm)	Th (ppm)	Pb (ppm)	Th/U	$^{207}Pb/^{235}U$	2σ	$^{206}Pb/^{238}U$	2σ	$^{207}Pb/^{206}Pb$	2σ	$^{207}Pb/^{235}U$ Age (Ma)	$^{206}Pb/^{238}U$ Age (Ma)	$^{207}Pb/^{206}Pb$ Age (Ma)	Concordance
~~SM12_Gr13~~	~~716~~	~~76.6~~	~~15.56~~	~~0.11~~	~~0.4895~~	~~0.0071~~	~~0.06387~~	~~0.00058~~	~~0.051~~	~~0.0013~~	~~404.5 ± 4.9~~	~~399.1 ± 3.5~~	~~232 ± 60~~	~~98.7~~
~~SM12_Gr14~~	~~769~~	~~410~~	~~87~~	~~0.52~~	~~0.69~~	~~0.014~~	~~0.07232~~	~~0.00066~~	~~0.0504~~	~~0.0015~~	~~523.3 ± 8.5~~	~~450.1 ± 3.9~~	~~199 ± 68~~	~~84.6~~
SM12_Gr15	1366	176.2	25.55	0.13	0.3815	0.0065	0.05226	0.00045	0.0505	0.0013	328.1 ± 4.8	328.4 ± 2.8	211 ± 59	100.1
SM12_Gr16	405.3	72.6	10.82	0.18	0.3984	0.0077	0.05426	0.00047	0.05046	0.00082	340.3 ± 5.6	340.6 ± 2.9	210 ± 39	100.1
SM12_Gr17	475.5	40.6	6.37	0.08	0.3827	0.0049	0.05238	0.00031	0.04956	0.00065	328.9 ± 3.6	329.1 ± 1.9	168 ± 31	100.1
SM12_Gr18	780	326.3	69.9	0.42	0.5731	0.0043	0.07406	0.00038	0.0557	0.00022	460.5 ± 2.7	460.5 ± 2.3	441.4 ± 9.3	100.0
SM12_Gr19	510	225.4	47.9	0.44	0.577	0.0053	0.07414	0.00055	0.05521	0.00042	462.4 ± 3.4	461 ± 3.3	422 ± 18	99.7
SM12_Gr20	998	368	79.9	0.36	0.5753	0.0041	0.07409	0.00041	0.05559	0.00038	461.3 ± 2.6	460.8 ± 2.5	438 ± 17	99.9
SM12_Gr21	1245	184.8	27.88	0.15	0.3691	0.0043	0.05058	0.00029	0.0508	0.0012	318.9 ± 3.2	318.1 ± 1.8	224 ± 55	99.7
~~SM12_Gr22_cr~~	~~661~~	~~275.1~~	~~54.74~~	~~0.41~~	~~0.489~~	~~0.0065~~	~~0.06432~~	~~0.00039~~	~~0.053~~	~~0.0013~~	~~404.2 ± 4.5~~	~~401.9 ± 2.3~~	~~321 ± 60~~	~~99.4~~
SM12_Gr22_rm	918	171.9	27.42	0.18	0.3915	0.0032	0.05364	0.00024	0.05235	0.00028	335.4 ± 2.3	336.8 ± 1.5	300 ± 13	100.4
SM12_Gr23	414	178	39.7	0.43	0.571	0.011	0.07512	0.00099	0.0535	0.0011	458.1 ± 7.1	446.9 ± 5.9	341 ± 49	101.9
SM12_Gr24	563	83.7	13.4	0.15	0.3878	0.0087	0.05205	0.00041	0.04794	0.00075	332.5 ± 6.3	327.1 ± 2.5	91 ± 36	98.4
SM12_Gr25	972	121	17	0.11	0.3886	0.0046	0.05322	0.0003	0.04953	0.00054	333.9 ± 3.3	334.3 ± 1.8	167 ± 26	100.1
SM12_Gr26	769	335	69.2	0.45	0.5776	0.0076	0.07443	0.0005	0.05328	0.00081	462.6 ± 4.9	462.8 ± 3	330 ± 36	100.0
SM12_Gr27	690	298	61	0.45	0.5752	0.0048	0.07455	0.00031	0.0531	0.00079	461.6 ± 3.2	463.5 ± 1.9	321 ± 35	100.4
SM12_Gr28	618	264.4	56.52	0.44	0.5732	0.0065	0.07425	0.00033	0.0535	0.00082	459.9 ± 4.2	461.7 ± 2	343 ± 37	100.4
~~SM12_Gr29_cr~~	~~618~~	~~241~~	~~86~~	~~0.40~~	~~0.908~~	~~0.018~~	~~0.07267~~	~~0.00037~~	~~0.05267~~	~~0.00085~~	~~654.5 ± 9.6~~	~~452.2 ± 2.2~~	~~301 ± 38~~	~~69.1~~
SM12_Gr29_rm	2300	333	47.5	0.15	0.3877	0.006	0.05336	0.00042	0.0512	0.0011	332.6 ± 4.4	335.1 ± 2.6	245 ± 54	100.8
SM12_Gr30	941	365	78.1	0.40	0.5819	0.006	0.07555	0.00034	0.05336	0.00084	465.5 ± 3.9	469.5 ± 2.1	339 ± 38	100.9
SM12_Gr31a	894	1184	266.6	1.37	0.576	0.01	0.07586	0.00062	0.05514	0.00035	461.8 ± 6.5	471.4 ± 3.7	417 ± 14	102.1
SM12_Gr31b	472	186	43.1	0.41	0.623	0.01	0.0789	0.00056	0.05273	0.00083	491.1 ± 6.4	489.5 ± 3.3	306 ± 37	99.7
SM12_Gr32	475.2	221.2	51.8	0.48	0.576	0.011	0.07527	0.00062	0.053	0.0013	463 ± 6.6	467.8 ± 3.7	319 ± 61	101.0
SM12_Gr33	853	389	79	0.47	0.577	0.01	0.0748	0.00071	0.0558	0.00069	462.7 ± 6.6	465 ± 4.3	443 ± 27	100.5
SM12_Gr34a	965	172	26.6	0.17	0.4126	0.0063	0.0556	0.00045	0.04915	0.00067	350.6 ± 4.5	349.1 ± 2.7	148 ± 31	99.6
SM12_Gr34b	1997	281	49	0.15	0.4074	0.0076	0.055	0.00066	0.0503	0.0013	346.9 ± 5.5	345.2 ± 4	203 ± 60	99.5
SM12_Gr35	1845	252.1	37.9	0.14	0.3986	0.0075	0.05364	0.00068	0.0504	0.001	340.5 ± 5.4	336.8 ± 4.2	206 ± 48	98.9
SM12_Gr36	524.8	240	53.02	0.47	0.586	0.011	0.07528	0.00058	0.0525	0.0011	468.1 ± 6.8	467.9 ± 3.5	296 ± 48	100.0
SM12_Gr37	629	278.3	59	0.46	0.536	0.0063	0.06956	0.00048	0.0519	0.00069	435.5 ± 4.1	433.5 ± 2.9	276 ± 32	99.5
SM12_Gr38	1401	643	127.6	0.47	0.5719	0.0071	0.07294	0.0006	0.05415	0.00092	459.1 ± 4.6	453.8 ± 3.6	387 ± 38	98.8
SM12_Gr39	530	116.9	22.73	0.23	0.5175	0.0078	0.06869	0.00051	0.05364	0.00039	424 ± 5ç1	428.3 ± 3.1	355 ± 16	101.0
SM12_Gr40	721	58.8	8.67	0.08	0.3971	0.0072	0.05423	0.00049	0.04961	0.00073	339.4 ± 5.2	340.4 ± 3	172 ± 35	100.3
SM12_Gr41	391.5	156.5	37.1	0.41	0.583	0.013	0.07556	0.0006	0.0529	0.0014	466.1 ± 8	469.6 ± 3.6	318 ± 64	100.8
SM12_Gr42	398	203.9	48.39	0.53	0.597	0.013	0.07604	0.00065	0.05446	0.00074	474.6 ± 8.4	472.4 ± 3.9	387 ± 32	99.5
								SM19						
SM19_Gr1	1200	278	41.4	0.23	0.3801	0.0052	0.05218	0.00068	0.0497	0.001	327.1 ± 3.8	327.9 ± 4.2	175 ± 49	100.2

ID	U (ppm)	Th (ppm)	Pb (ppm)	Th/U	$^{207}Pb/^{235}U$	2σ	$^{206}Pb/^{238}U$	2σ	$^{207}Pb/^{206}Pb$	2σ	$^{207}Pb/^{235}U$ Age (Ma)	$^{206}Pb/^{238}U$ Age (Ma)	$^{207}Pb/^{206}Pb$ Age (Ma)	Concordance
SM19_Gr2	452.7	119.6	19.09	0.26	0.3827	0.0061	0.05218	0.00062	0.05052	0.00079	328.9 ± 4.5	327.9 ± 3.8	215 ± 37	99.7
SM19_Gr3	860	172	25.5	0.20	0.3801	0.0041	0.05216	0.00049	0.05011	0.00071	327 ± 3	327.7 ± 3	194 ± 34	100.2
SM19_Gr4	1723	629	97.8	0.37	0.3817	0.0057	0.05228	0.00057	0.0514	0.0011	328.3 ± 4.2	328.5 ± 3.5	256 ± 51	100.1
SM19_Gr5	1689	603.9	91.7	0.35	0.3777	0.0057	0.05218	0.00055	0.05088	0.00097	325.3 ± 4.2	327.9 ± 3.4	230 ± 46	100.8
SM19_Gr6	1119	480	76.9	0.40	0.3803	0.0032	0.05208	0.00033	0.05196	0.0003	327.4 ± 2.4	327.3 ± 2	282 ± 14	100.0
~~**SM19_Gr7**~~	~~426.8~~	~~105.6~~	~~63.3~~	~~0.23~~	~~0.97~~	~~0.067~~	~~0.05789~~	~~0.00071~~	~~0.05391~~	~~0.00013~~	~~675 ± 34~~	~~362.8 ± 4.3~~	~~367.1 ± 5.3~~	~~53.7~~
SM19_Gr8	1121	476	76.6	0.41	0.3819	0.0067	0.05222	0.00051	0.0497	0.001	329.2 ± 4.7	328.1 ± 3.1	173 ± 48	99.7
SM19_Gr9	905	302	47.9	0.33	0.383	0.01	0.0518	0.001	0.0481	0.0014	331.2 ± 8.1	325.2 ± 6.3	99 ± 68	98.2
SM19_Gr10	413.5	151.3	25.58	0.36	0.3799	0.0064	0.05187	0.00047	0.0507	0.0012	326.9 ± 4.7	326 ± 2.9	224 ± 56	99.7
SM19_Gr11	748	438.8	73.6	0.58	0.3837	0.0083	0.05159	0.00047	0.05202	0.00074	329.7 ± 6	324.3 ± 2.9	286 ± 33	98.4
SM19_Gr12	972	414	71.1	0.43	0.3851	0.0082	0.05213	0.00078	0.0522	0.00039	330.7 ± 6	327.6 ± 4.8	294 ± 17	99.1
SM19_Gr13	464	104.1	15.83	0.22	0.3793	0.0055	0.05192	0.00049	0.04932	0.00073	326.4 ± 4.1	326.3 ± 3	158 ± 35	100.0
SM19_Gr14	1140	301	44.3	0.27	0.3761	0.0037	0.05183	0.00055	0.05101	0.00073	324.1 ± 2.7	325.7 ± 3.4	237 ± 35	100.5
SM19_Gr15	698	181	28	0.26	0.3824	0.0036	0.05199	0.00035	0.05039	0.00056	329 ± 2.6	326.7 ± 2.1	207 ± 26	99.3
SM19_Gr16	978	343	60.8	0.35	0.4056	0.0067	0.04962	0.00043	0.04607494	0.00000091	345.6 ± 4.8	312.2 ± 2.6	1542 ± 48	90.3
SM19_Gr17	419	100.9	15.3	0.24	0.3833	0.004	0.05206	0.00027	0.0502	0.00061	329.3 ± 2.9	327.2 ± 1.7	198 ± 29	99.4
SM19_Gr18	936.3	451.3	80.2	0.50	0.3946	0.0063	0.0538	0.00051	0.0518	0.00063	337.7 ± 4.6	337.8 ± 3.1	276 ± 28	100.0
SM19_Gr19	1296	514	85.9	0.41	0.3835	0.0059	0.05266	0.00046	0.05169	0.0004	329.6 ± 4.3	330.8 ± 2.8	271 ± 18	100.4
~~**SM19_Gr20**~~	~~318.3~~	~~78.7~~	~~14.7~~	~~0.25~~	~~0.442~~	~~0.012~~	~~0.05835~~	~~0.00065~~	~~0.04975~~	~~0.00057~~	~~371.3 ± 8.4~~	~~366 ± 3.9~~	~~177 ± 27~~	~~98.6~~
SM19_Gr21	465	110	18.7	0.25	0.394	0.0077	0.05287	0.00039	0.04921	0.00078	337.1 ± 5.6	332.1 ± 2.4	152 ± 37	98.5
								SM20						
SM20_Gr1	200	105	15.3	0.52	0.4095	0.0082	0.05501	0.00055	0.05118	0.00079	348.3 ± 5.9	345.2 ± 3.4	244 ± 37	99.1
~~**SM20_Gr2**~~	~~643.1~~	~~866~~	~~155.1~~	~~1.34~~	~~0.4629~~	~~0.0059~~	~~0.05335~~	~~0.00053~~	~~0.05382~~	~~0.00049~~	~~386.2 ± 4.1~~	~~335.1 ± 3.2~~	~~362 ± 21~~	~~86.8~~
SM20_Gr3	315.1	185.6	28.7	0.58	0.3764	0.0045	0.05111	0.00038	0.04927	0.0006	324.3 ± 3.3	321.3 ± 2.3	155 ± 29	99.1
SM20_Gr4	101.8	19.86	3.04	0.19	0.374	0.0099	0.05126	0.00042	0.04817	0.00061	322.2 ± 7.3	322.3 ± 2.6	103 ± 29	100.0
~~**SM20_Gr5**~~	~~501~~	~~23.2~~	~~7.55~~	~~0.05~~	~~0.496~~	~~0.015~~	~~0.06513~~	~~0.00058~~	~~0.05467~~	~~0.00022~~	~~409 ± 10~~	~~406.7 ± 3.5~~	~~398.7 ± 9.1~~	~~99.4~~
SM20_Gr6	416	144.9	21.33	0.34	0.3901	0.0075	0.05281	0.00059	0.04967	0.00097	334.3 ± 5.5	331.7 ± 3.6	173 ± 46	99.2
SM20_Gr7	257.3	94.7	14.02	0.36	0.39	0.0071	0.05242	0.00037	0.04929	0.00073	334.1 ± 5.2	329.4 ± 2.3	154 ± 34	98.6
SM20_Gr8	185	129.3	20.52	0.69	0.3818	0.009	0.05281	0.00038	0.05029	0.00076	328.1 ± 6.6	331.7 ± 2.3	203 ± 36	101.1
SM20_Gr9	284	214	33.1	0.73	0.3882	0.0054	0.05273	0.00038	0.05125	0.00062	332.9 ± 3.9	331.3 ± 2.3	246 ± 29	99.5
SM20_Gr10	77.4	18.4	3.03	0.24	0.376	0.018	0.05259	0.00093	0.049	0.001	327 ± 15	330.4 ± 5.7	141 ± 49	101.0
~~**SM20_Gr11**~~	~~258~~	~~90.6~~	~~13~~	~~0.34~~	~~0.38~~	~~0.011~~	~~0.05195~~	~~0.00068~~	~~0.0496~~	~~0.0012~~	~~327.1 ± 8.3~~	~~326.5 ± 4.1~~	~~172 ± 60~~	~~100.0~~
SM20_Gr12	169.5	86	13.99	0.50	0.3852	0.0086	0.05251	0.0005	0.04969	0.00072	330.6 ± 6.3	330.4 ± 3.2	179 ± 35	99.9
SM20_Gr13	359.1	394.3	63.9	1.08	0.3759	0.0089	0.05185	0.00083	0.05222	0.00072	323.9 ± 6.6	325.9 ± 5.1	293 ± 31	100.6
SM20_Gr14	167.5	56.9	7.97	0.35	0.388	0.021	0.05233	0.00077	0.04769	0.00061	331 ± 15	328.8 ± 4.7	81 ± 30	99.3
SM20_Gr15	337	151	22.7	0.45	0.3861	0.0097	0.05223	0.00047	0.04892	0.00064	331.1 ± 7.1	328.2 ± 2.9	139 ± 30	99.1

ID	U (ppm)	Th (ppm)	Pb (ppm)	Th/U	$^{207}Pb/^{235}U$	2σ	$^{206}Pb/^{238}U$	2σ	$^{207}Pb/^{206}Pb$	2σ	$^{207}Pb/^{235}U$ Age (Ma)	$^{206}Pb/^{238}U$ Age (Ma)	$^{207}Pb/^{206}Pb$ Age (Ma)	Concordance
~~SM20_Gr16~~	~~409.5~~	~~303~~	~~50.8~~	~~0.78~~	~~0.384~~	~~0.011~~	~~0.05241~~	~~0.00053~~	~~0.04952~~	~~0.00077~~	~~329.9 ± 8~~	~~329.3 ± 3.2~~	~~169 ± 37~~	~~100.0~~
SM20_Gr17	772	782	121.6	1.04	0.3788	0.0072	0.05098	0.00039	0.05101	0.00069	325.9 ± 5.3	320.5 ± 2.4	236 ± 32	98.3
SM20_Gr18	453.4	121.8	17.71	0.28	0.3862	0.0092	0.05201	0.00047	0.04884	0.00083	331.4 ± 6.7	326.8 ± 2.9	135 ± 40	98.6
SM20_Gr19	248	172.4	26.79	0.72	0.382	0.01	0.05229	0.00046	0.04902	0.00049	330.6 ± 7.3	328.6 ± 2.8	144 ± 23	99.4
SM20_Gr20	311.9	104.2	15.85	0.35	0.394	0.018	0.05245	0.0008	0.04883	0.00085	336 ± 13	329.5 ± 4.9	140 ± 41	98.1
SM20_Gr21	283.1	62.7	10.11	0.23	0.392	0.011	0.05305	0.00066	0.04855	0.00065	336.7 ± 7.8	333.2 ± 4	121 ± 31	99.0
SM20_Gr22	328.9	119.6	19.28	0.38	0.383	0.011	0.0527	0.00049	0.04873	0.00059	328.9 ± 8.4	331.1 ± 3	130 ± 28	100.7
~~SM20_Gr23~~	~~2020~~	~~571~~	~~81.2~~	~~0.30~~	~~0.3347~~	~~0.0056~~	~~0.04641~~	~~0.00072~~	~~0.04925~~	~~0.00057~~	~~292.9 ± 4.2~~	~~292.4 ± 4.4~~	~~154 ± 27~~	~~99.8~~
SM20_Gr24	449	317	45.5	0.71	0.382	0.012	0.05275	0.00074	0.0506	0.00083	327.9 ± 8.5	331.3 ± 4.5	225 ± 40	101.0
SM20_Gr25	168.3	39.7	6.35	0.24	0.382	0.012	0.0529	0.00054	0.04847	0.00046	327.2 ± 8.9	332.6 ± 3.3	121 ± 22	101.7
~~SM20_Gr26~~	~~349~~	~~165~~	~~32.8~~	~~0.50~~	~~0.543~~	~~0.018~~	~~0.0529~~	~~0.00057~~	~~0.04628~~	~~0.00025~~	~~441 ± 12~~	~~332.3 ± 3.5~~	~~11 ± 12~~	~~75.4~~
SM20_Gr27	190.5	65.9	9.16	0.35	0.369	0.016	0.05265	0.00066	0.04767	0.00047	319 ± 12	330.8 ± 4	80 ± 23	103.7
SM20_Gr28	62	26.7	4.05	0.41	0.424	0.062	0.0544	0.0021	0.0489	0.0013	352 ± 45	341 ± 13	133 ± 59	96.9
SM20_Gr29	537.2	35.8	6.79	0.07	0.373	0.012	0.05248	0.00076	0.0494	0.001	321.8 ± 9	329.7 ± 4.7	163 ± 48	102.5
SM20_Gr30	323	106	15.4	0.33	0.377	0.011	0.05239	0.00043	0.04891	0.00057	323.6 ± 8.4	329.2 ± 2.6	138 ± 27	101.7
SM20_Gr31	194	71.8	10.85	0.37	0.397	0.037	0.0528	0.0011	0.04762	0.00072	336 ± 27	331.8 ± 6.4	77 ± 35	98.8
SM20_Gr32	249	36.7	5.24	0.14	0.3769	0.0099	0.05258	0.00034	0.04862	0.00049	324.7 ± 7.3	330.4 ± 2.1	124 ± 24	101.8
SM20_Gr33	129.6	52.9	7.79	0.40	0.391	0.017	0.05224	0.00059	0.04794	0.00048	335 ± 13	328.2 ± 3.6	91 ± 23	98.0
SM20_Gr34	457	8.1	1.56	0.02	0.3818	0.007	0.05238	0.00034	0.05085	0.0005	328 ± 5.2	329.1 ± 2.1	230 ± 24	100.3
SM20_Gr35	581	401.9	56.19	0.69	0.3875	0.0095	0.05259	0.00058	0.05016	0.00091	332.2 ± 7	330.4 ± 3.5	195 ± 43	99.5
SM20_Gr36	185.7	43.7	6.2	0.23	0.378	0.019	0.05379	0.00088	0.0499	0.0012	325 ± 14	337.7 ± 5.4	182 ± 55	103.9
~~SM20_Gr37~~	~~463~~	~~149.6~~	~~29.5~~	~~0.32~~	~~0.4552~~	~~0.0074~~	~~0.05584~~	~~0.00031~~	~~0.04692~~	~~0.00038~~	~~380.5 ± 5.2~~	~~350.3 ± 1.9~~	~~42 ± 18~~	~~92.0~~
SM20_Gr38	504	234	33	0.46	0.38	0.011	0.05332	0.00089	0.04934	0.00081	326.9 ± 8.2	334.8 ± 5.4	162 ± 39	102.4
SM20_Gr39	377	137.5	22.03	0.39	0.3951	0.0081	0.05335	0.00032	0.0482	0.00049	337.6 ± 5.9	335 ± 2	104 ± 23	99.2
SM20_Gr40	267	128.4	18.72	0.51	0.366	0.01	0.05104	0.00036	0.04814	0.00047	315.5 ± 7.7	320.9 ± 2.2	104 ± 23	101.7
								SM21						
SM21_Gr1	177.6	81.8	17.83	0.45	0.565	0.0086	0.07276	0.00059	0.05361	0.00091	455.3 ± 5.4	452.7 ± 3.5	345 ± 40	99.43
SM21_Gr2	153.8	69.1	14.66	0.43	0.5606	0.0087	0.07281	0.0005	0.05286	0.00076	451.6 ± 5.6	453 ± 3	314 ± 34	100.31
SM21_Gr3	112.1	49.6	10.88	0.43	0.566	0.0091	0.07292	0.00056	0.0519	0.00081	454.9 ± 5.9	453.7 ± 3.4	270 ± 37	99.74
SM21_Gr4	326.1	100.8	24.4	0.30	0.5699	0.0086	0.07263	0.00071	0.0529	0.0014	457.8 ± 5.5	452 ± 4.3	312 ± 62	98.73
SM21_Gr5	268.3	108.4	22.98	0.40	0.586	0.014	0.0747	0.00083	0.05496	0.00083	468.2 ± 8.8	464.4 ± 5	408 ± 35	99.19
SM21_Gr6	553	116.1	22.4	0.21	0.5832	0.0085	0.07446	0.0009	0.0521	0.0013	466.3 ± 5.4	462.9 ± 5.4	277 ± 57	99.27
SM21_Gr7	778	313.5	65.4	0.40	0.5825	0.0061	0.0746	0.00051	0.05565	0.00047	465.9 ± 3.9	463.8 ± 3	436 ± 19	99.55
SM21_Gr8	355	21.69	4.57	0.06	0.4532	0.0082	0.06045	0.00085	0.05159	0.00059	379 ± 5.7	378.3 ± 5.1	261 ± 28	99.82
SM21_Gr9	1135	772	158.7	0.67	0.5828	0.0055	0.07452	0.00051	0.05613	0.00037	466.1 ± 3.5	463.3 ± 3.1	456 ± 15	99.40
SM21_Gr10	1019	457	96.2	0.45	0.5831	0.0038	0.07467	0.00032	0.05597	0.00024	466.4 ± 2.4	464.2 ± 1.9	452 ± 10	99.53

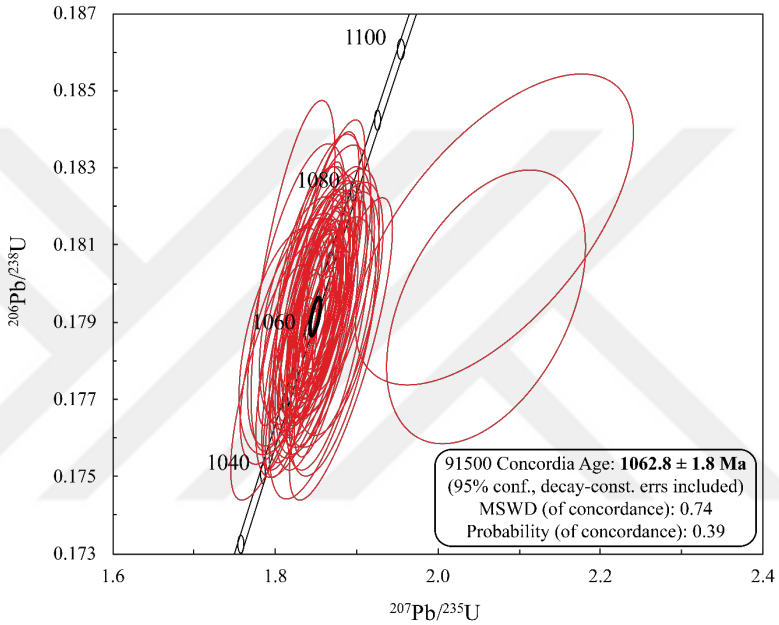
ID	U (ppm)	Th (ppm)	Pb (ppm)	Th/U	$^{207}Pb/^{235}U$	2σ	$^{206}Pb/^{238}U$	2σ	$^{207}Pb/^{206}Pb$	2σ	$^{207}Pb/^{235}U$ Age (Ma)	$^{206}Pb/^{238}U$ Age (Ma)	$^{207}Pb/^{206}Pb$ Age (Ma)	Concordance
SM21_Gr11	477	210.7	43.2	0.44	0.59	0.016	0.07497	0.00067	0.0569	0.0014	470 ± 10	466 ± 4	485 ± 52	99.15
SM21_Gr12	454	188.6	39.2	0.41	0.5841	0.0054	0.07475	0.00035	0.05545	0.00034	467.3 ± 3.5	464.7 ± 2.1	429 ± 14	99.44
SM21_Gr13	904	324.7	64.8	0.36	0.5832	0.0066	0.07475	0.00077	0.05602	0.00046	467 ± 4.3	464.7 ± 4.6	452 ± 19	99.51
SM21_Gr14	179	68	15.49	0.38	0.584	0.01	0.07459	0.00058	0.0517	0.0011	466.6 ± 6.5	463.7 ± 3.5	261 ± 52	99.38
SM21_Gr15	544.1	217.2	44.7	0.40	0.588	0.014	0.0741	0.0012	0.0547	0.0017	471.3 ± 8.8	461.1 ± 7.3	445 ± 55	97.84
SM21_Gr16	479	185.4	38	0.38	0.571	0.013	0.0738	0.0013	0.0537	0.0016	458.2 ± 8	459.2 ± 7.9	351 ± 72	100.22
SM21_Gr17	1625	832	170.1	0.52	0.5801	0.0086	0.0741	0.00098	0.05559	0.0009	464.4 ± 5.5	460.8 ± 5.9	434 ± 38	99.22
SM21_Gr18	398	165.7	33.9	0.42	0.5498	0.0082	0.07175	0.0004	0.0512	0.00074	444.4 ± 5.3	446.7 ± 2.4	245 ± 34	100.52
SM21_Gr19	747	366.5	72.7	0.50	0.5351	0.007	0.07075	0.00047	0.05503	0.00052	435 ± 4.6	440.6 ± 2.8	415 ± 22	101.29
SM21_Gr20	276	121.8	27.9	0.45	0.571	0.017	0.07504	0.00098	0.053	0.0013	460 ± 11	466.4 ± 5.9	317 ± 56	101.39
SM21_Gr21	2160	1332	271.4	0.63	0.5722	0.0079	0.07537	0.00066	0.05566	0.00026	459.4 ± 5.1	468.4 ± 4	439 ± 10	101.96
SM21_Gr22	202	46.1	9.71	0.23	0.568	0.033	0.0736	0.0021	0.0544	0.0013	455 ± 21	457 ± 13	383 ± 55	100.44
SM21_Gr23	210.7	95.6	19.73	0.46	0.54	0.014	0.07044	0.00081	0.05124	0.00088	437.7 ± 9.5	438.8 ± 4.9	241 ± 40	100.25
SM21_Gr24	329	131	26.02	0.41	0.555	0.015	0.07347	0.00084	0.05219	0.00098	448.8 ± 9.9	457 ± 5	286 ± 44	101.83
SM21_Gr25a	744	344	74.1	0.48	0.581	0.01	0.07504	0.00094	0.05332	0.00079	464.9 ± 6.4	466.4 ± 5.7	332 ± 35	100.32
SM21_Gr25b	1748	504	102.7	0.30	0.5689	0.0076	0.07452	0.00077	0.05543	0.0006	457.2 ± 4.9	463.3 ± 4.6	436 ± 29	101.33
SM21_Gr26	277.5	135.9	27.73	0.51	0.588	0.016	0.0753	0.001	0.0528	0.0013	469 ± 10	467.8 ± 6.3	311 ± 58	99.74
SM21_Gr27	469.4	207	50.8	0.46	0.59	0.01	0.07533	0.00092	0.051	0.0022	470.7 ± 6.5	468.2 ± 5.5	220 ± 100	99.47
SM21_Gr28	258	110.3	24.33	0.44	0.579	0.01	0.07578	0.0005	0.05279	0.00073	466.1 ± 6.4	470.9 ± 3	313 ± 33	101.03
SM21_Gr29	537	325	70.5	0.63	0.57	0.015	0.07591	0.00072	0.0549	0.0006	457.9 ± 9.9	471.7 ± 4.3	407 ± 25	103.01
SM21_Gr30	1254	488	102.6	0.41	0.5779	0.0075	0.07571	0.00063	0.05573	0.00035	463 ± 4.8	470.5 ± 3.7	441 ± 14	101.62
SM21_Gr31	180	75.6	17.39	0.44	0.586	0.013	0.07656	0.00078	0.05472	0.00058	467.3 ± 8.6	475.5 ± 4.7	401 ± 26	101.75
SM21_Gr32	258	10.4	1.57	0.05	0.413	0.011	0.05644	0.00063	0.05111	0.00052	350.4 ± 7.9	353.9 ± 3.8	240 ± 24	101.00
SM21_Gr33_cr	265.3	241.6	51.7	0.94	0.573	0.018	0.07602	0.00098	0.05403	0.00088	459 ± 12	472.3 ± 5.9	374 ± 39	102.90
SM21_Gr33_rm	198.4	26.3	4.25	0.12	0.389	0.02	0.05581	0.00084	0.04916	0.00091	333 ± 15	350.1 ± 5.1	149 ± 43	105.14
SM21_Gr34	421	241.3	50.5	0.59	0.5741	0.0095	0.07577	0.0007	0.05315	0.00087	460.3 ± 6.1	470.8 ± 4.2	327 ± 39	102.28
SM21_Gr35	343	154.4	33	0.46	0.583	0.0093	0.0762	0.00049	0.05271	0.00075	466.5 ± 5.9	473.4 ± 2.9	309 ± 34	101.48
SM21_Gr36	279	118.3	24.94	0.43	0.579	0.011	0.0761	0.00051	0.05259	0.00073	463.2 ± 6.9	472.8 ± 3.1	304 ± 33	102.07
SM21_Gr37	590	242.3	49.86	0.42	0.5751	0.0099	0.07596	0.00057	0.05293	0.00096	461 ± 6.4	472 ± 3.4	316 ± 43	102.39
SM21_Gr38	489.3	172.7	34.36	0.36	0.575	0.014	0.07569	0.00078	0.0522	0.0011	460.8 ± 8.8	470.3 ± 4.7	283 ± 51	102.06
SM21_Gr39	245	22.4	3.42	0.08	0.417	0.013	0.05607	0.00062	0.0505	0.00062	353.8 ± 9.4	351.6 ± 3.8	212 ± 29	99.38
SM21_Gr40	804	150.4	23.71	0.19	0.3846	0.0073	0.05308	0.00037	0.04983	0.00089	330.3 ± 5.4	333.4 ± 2.3	182 ± 42	100.94
SM21_Gr41	788	403	78.6	0.52	0.5961	0.0097	0.07617	0.00069	0.0528	0.0016	474.6 ± 6.2	473.2 ± 4.2	307 ± 72	99.71
SM21_Gr42	608.5	373.1	79.1	0.62	0.5787	0.0098	0.07615	0.00064	0.05476	0.00053	463.3 ± 6.3	473.1 ± 3.8	404 ± 23	102.12
~~**SM21_Gr43**~~	~~433~~	~~174.9~~	~~54.6~~	~~0.41~~	~~0.811~~	~~0.025~~	~~0.07758~~	~~0.00051~~	~~0.05138~~	~~0.00095~~	~~603 ± 14~~	~~481.6 ± 3~~	~~241 ± 43~~	~~79.87~~
SM21_Gr44	316	144.3	31.92	0.46	0.582	0.012	0.07652	0.00066	0.05241	0.00086	465.5 ± 7.8	475.3 ± 3.9	294 ± 39	102.11

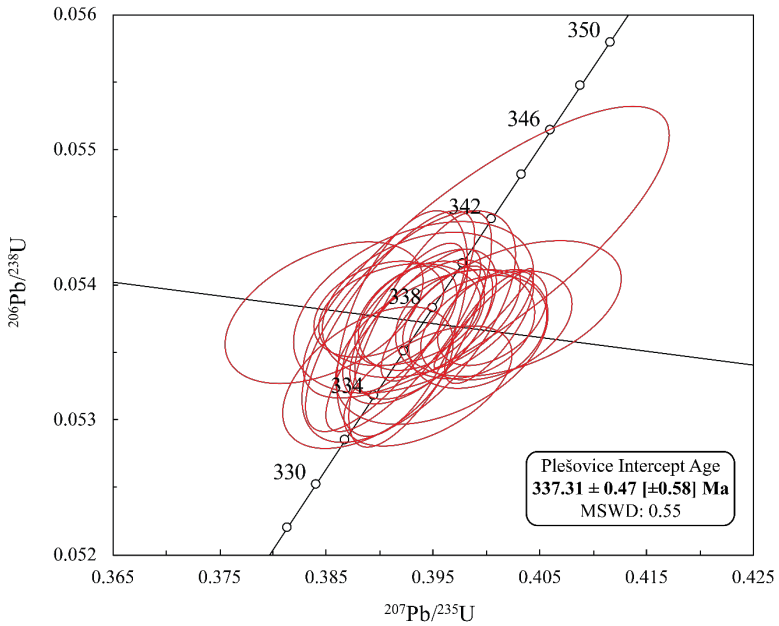
ID	U (ppm)	Th (ppm)	Pb (ppm)	Th/U	$^{207}Pb/^{235}U$	2σ	$^{206}Pb/^{238}U$	2σ	$^{207}Pb/^{206}Pb$	2σ	$^{207}Pb/^{235}U$ Age (Ma)	$^{206}Pb/^{238}U$ Age (Ma)	$^{207}Pb/^{206}Pb$ Age (Ma)	Concordance
SM21_Gr45	1117	156.3	22.64	0.14	0.3862	0.004	0.05279	0.00026	0.04996	0.00058	331.4 ± 2.9	331.6 ± 1.6	187 ± 27	100.06
SM21_Gr46	1314	439	94.3	0.35	0.5958	0.0075	0.07575	0.00046	0.05539	0.00053	475.1 ± 4.9	470.7 ± 2.8	426 ± 22	99.07
SM21_Gr47	256.5	116.4	25.86	0.47	0.588	0.017	0.07592	0.00062	0.05468	0.0006	469 ± 11	471.7 ± 3.7	397 ± 26	100.58
SM21_Gr48a	248.7	160.8	39.4	0.68	0.562	0.021	0.0733	0.0014	0.0514	0.0014	452 ± 13	456.2 ± 8.6	257 ± 64	100.93
~~**SM21_Gr48b**~~	~~193.1~~	~~53.9~~	~~62~~	~~0.30~~	~~2.113~~	~~0.099~~	~~0.085~~	~~0.0016~~	~~0.05791~~	~~0.00026~~	~~1148 ± 32~~	~~526 ± 9.7~~	~~526 ± 9.7~~	~~45.82~~
SM21_Gr49	382	151.4	32.93	0.42	0.56	0.012	0.07375	0.0006	0.05246	0.00098	452.1 ± 7.9	458.7 ± 3.6	296 ± 45	101.46
SM21_Gr50	373	148.9	34.31	0.42	0.559	0.011	0.07397	0.00051	0.05236	0.00085	450.7 ± 6.9	460 ± 3.1	292 ± 39	102.06
~~**SM21_Gr51**~~	~~815.5~~	~~115.8~~	~~52.8~~	~~0.15~~	~~0.635~~	~~0.027~~	~~0.05955~~	~~0.00039~~	~~0.054096~~	~~0.000067~~	~~496 ± 16~~	~~372.9 ± 2.4~~	~~375 ± 2.8~~	~~75.18~~
~~**SM21_Gr52**~~	~~192.2~~	~~47.1~~	~~25.5~~	~~0.22~~	~~0.96~~	~~0.084~~	~~0.0772~~	~~0.0011~~	~~0.05661~~	~~0.00024~~	~~671 ± 43~~	~~479.6 ± 6.7~~	~~475.8 ± 9.3~~	~~71.48~~
SM21_Gr53	406	177.1	38.1	0.45	0.57	0.01	0.07415	0.00039	0.05156	0.0008	457.8 ± 6.6	461.1 ± 2.3	258 ± 37	100.72
							SM29							
SM29_Gr1	402.8	187.5	41.9	0.45	0.5766	0.0059	0.07438	0.00054	0.0551	0.00044	462.9 ± 3.7	462.5 ± 3.2	416 ± 19	99.91
~~**SM29_Gr2**~~	~~76.4~~	~~14.35~~	~~2.384~~	~~0.17~~	~~0.3961~~	~~0.0095~~	~~0.05294~~	~~0.00054~~	~~0.04838~~	~~0.00057~~	~~338.3 ± 6.9~~	~~332.5 ± 3.3~~	~~112 ± 27~~	~~98.29~~
~~**SM29_Gr3**~~	~~465~~	~~604~~	~~123.3~~	~~1.29~~	~~0.4831~~	~~0.0084~~	~~0.06357~~	~~0.00069~~	~~0.05466~~	~~0.00061~~	~~400.1 ± 5.7~~	~~397.3 ± 4.2~~	~~397 ± 25~~	~~99.30~~
~~**SM29_Gr4**~~	~~276~~	~~163~~	~~61~~	~~0.39~~	~~0.73~~	~~0.035~~	~~0.0896~~	~~0.0049~~	~~0.05571~~	~~0.00044~~	~~565 ± 20~~	~~552 ± 29~~	~~439 ± 18~~	~~97.70~~
~~**SM29_Gr5**~~	~~1487~~	~~1569~~	~~394~~	~~1.10~~	~~0.767~~	~~0.0098~~	~~0.07716~~	~~0.00058~~	~~0.05747~~	~~0.00046~~	~~578.1 ± 5.6~~	~~479.1 ± 3.5~~	~~509 ± 18~~	~~82.87~~
SM29_Gr6	656	566	130.3	0.88	0.5863	0.0076	0.07522	0.00076	0.05587	0.0003	468.9 ± 4.9	467.5 ± 4.5	446 ± 12	99.70
SM29_Gr7	532	353	71.8	0.68	0.5606	0.0073	0.07259	0.00055	0.05528	0.0003	451.7 ± 4.8	451.7 ± 3.3	426 ± 14	100.00
SM29_Gr8	445.5	283	60.8	0.63	0.5601	0.0051	0.07276	0.0004	0.05539	0.00028	451.4 ± 3.3	453 ± 2.4	429 ± 12	100.35
~~**SM29_Gr9**~~	~~371~~	~~125~~	~~61.3~~	~~0.34~~	~~1.055~~	~~0.016~~	~~0.07984~~	~~0.00055~~	~~0.057096~~	~~0.000085~~	~~730.6 ± 8~~	~~495.1 ± 3.3~~	~~495.1 ± 3.3~~	~~67.77~~
SM29_Gr10	92.9	26.2	5.69	0.28	0.556	0.016	0.07302	0.00081	0.05265	0.00078	450 ± 10	454.3 ± 4.9	305 ± 35	100.96
SM29_Gr11	237	137.6	29.6	0.59	0.5587	0.008	0.07313	0.00056	0.05487	0.00036	450.3 ± 5.2	455 ± 3.3	405 ± 15	101.04
SM29_Gr12	418	118.6	25.17	0.30	0.5543	0.0099	0.0725	0.0012	0.0526	0.0014	447.6 ± 6.5	451.3 ± 7	301 ± 62	100.83
SM29_Gr13	1007.8	988	220.3	1.01	0.6163	0.0095	0.07444	0.00059	0.05621	0.00056	487 ± 6	462.8 ± 3.5	456 ± 22	95.03
~~**SM29_Gr14**~~	~~1909~~	~~317.7~~	~~50.4~~	~~0.18~~	~~0.4027~~	~~0.0034~~	~~0.05453~~	~~0.0003~~	~~0.05094~~	~~0.00054~~	~~343.5 ± 2.5~~	~~342.3 ± 1.8~~	~~232 ± 25~~	~~99.65~~
SM29_Gr15	77.8	19.9	4.18	0.24	0.591	0.032	0.0746	0.0014	0.05268	0.00082	475 ± 21	463.7 ± 8.3	303 ± 37	97.62
~~**SM29_Gr16**~~	~~580~~	~~279~~	~~75.7~~	~~0.51~~	~~0.79~~	~~0.02~~	~~0.07969~~	~~0.00097~~	~~0.05086~~	~~0.00097~~	~~590 ± 11~~	~~494.2 ± 5.8~~	~~225 ± 44~~	~~83.76~~
SM29_Gr17	1168	726	163.8	0.66	0.5914	0.0051	0.07523	0.00037	0.0532	0.0011	471.7 ± 3.3	467.6 ± 2.2	323 ± 51	99.13
SM29_Gr18	103.5	23.3	4.83	0.23	0.564	0.038	0.0733	0.0018	0.0517	0.0011	454 ± 25	456 ± 11	260 ± 48	100.44
SM29_Gr19	488	125.6	26.09	0.27	0.585	0.014	0.07466	0.00097	0.0525	0.0014	467.1 ± 8.8	464.2 ± 5.8	300 ± 63	99.38
SM29_Gr20	1366	437.2	96.8	0.34	0.5787	0.0043	0.07448	0.00035	0.05556	0.00018	463.8 ± 2.7	463.1 ± 2.1	434.5 ± 7.4	99.85
SM29_Gr21	107.3	39	9.08	0.38	0.564	0.028	0.0735	0.0013	0.05086	0.00099	451 ± 18	457.3 ± 7.7	223 ± 44	101.40
SM29_Gr22a	576	277.8	60.94	0.51	0.577	0.011	0.07401	0.0006	0.05323	0.00099	461.9 ± 7.1	460.3 ± 3.6	330 ± 45	99.65
SM29_Gr22b	1165	443.7	93.2	0.41	0.5665	0.0083	0.07327	0.00047	0.0535	0.0012	456.7 ± 5.6	455.8 ± 2.8	341 ± 56	99.80
SM29_Gr23	511	204.9	48.5	0.43	0.565	0.013	0.07337	0.00088	0.0527	0.0014	454.4 ± 8.4	456.4 ± 5.3	306 ± 62	100.44

C. U-Pb LA-MC-ICP-MS RESULTS OF ZIRCON STANDARDS

In this appendix, the LA-MC-ICP-MS measurement results and the calculated ages from the zircon 91500 and Plešovice standards are presented.

$^{207}Pb/^{235}U$ vs. $^{206}Pb/^{238}U$ diagrams showing the concordia age of 91500 standard sample and intercept age of Plešovice standard sample.





ID	U (ppm)	Th (ppm)	Pb (ppm)	Th/U	$^{207}Pb/^{235}U$	2σ	$^{206}Pb/^{238}U$	2σ	$^{207}Pb/^{206}Pb$	2σ	$^{207}Pb/^{235}U$ Age (Ma)	$^{206}Pb/^{238}U$ Age (Ma)	$^{207}Pb/^{206}Pb$ Age (Ma)
							91500						
Z_91500_1	77.7	29.5	14.63	0.38	1.852	0.025	0.1798	0.0017	0.0738	0.00044	1064.2 ± 8.7	1066.6 ± 9.4	1037 ± 13
Z_91500_2	80.7	30.2	15.02	0.37	1.821	0.03	0.1781	0.0024	0.07373	0.00043	1055 ± 11	1056 ± 13	1033 ± 12
Z_91500_3	80.5	29.7	15.08	0.38	1.843	0.026	0.178	0.0018	0.07379	0.00053	1059.8 ± 9.4	1056 ± 10	1036 ± 16
Z_91500_4	81.9	31	15.43	0.37	1.878	0.027	0.1797	0.002	0.07379	0.00068	1073.2 ± 9.6	1066 ± 11	1034 ± 22
Z_91500_5	79.4	29.9	14.81	0.38	1.854	0.023	0.1801	0.0019	0.074	0.00042	1064.8 ± 8.4	1067 ± 11	1037 ± 13
Z_91500_6	79.9	29.8	14.93	0.37	1.85	0.025	0.1785	0.0017	0.0741	0.00056	1063.4 ± 9	1058.5 ± 9.4	1042 ± 15
Z_91500_7	81	30.2	15.22	0.38	1.853	0.025	0.1807	0.002	0.07334	0.00039	1064.1 ± 9.2	1070 ± 11	1026 ± 12
Z_91500_8	79.2	29.7	14.83	0.38	1.867	0.024	0.1795	0.0016	0.07377	0.00054	1069.4 ± 8.6	1064.8 ± 8.8	1044 ± 20
Z_91500_9	79.7	30.1	14.97	0.37	1.829	0.022	0.1784	0.0016	0.07387	0.00041	1056.9 ± 7.8	1057.9 ± 8.8	1043 ± 14
Z_91500_1	78.8	29.4	14.89	0.37	1.86	0.03	0.1797	0.0022	0.07381	0.00066	1065 ± 10	1065 ± 12	1033 ± 18
Z_91500_2	79.9	30	15.1	0.37	1.841	0.029	0.1791	0.002	0.07384	0.00071	1060 ± 10	1062 ± 11	1037 ± 21
Z_91500_3	81	30.4	15.04	0.38	1.827	0.028	0.1778	0.002	0.07283	0.0009	1055 ± 10	1055 ± 11	1003 ± 28
Z_91500_4	82	31.3	15.08	0.37	1.868	0.029	0.1801	0.0019	0.07378	0.00049	1069 ± 10	1067 ± 11	1034 ± 13
Z_91500_5	79.4	29.3	14.93	0.37	1.863	0.024	0.1799	0.0018	0.07353	0.0006	1067.9 ± 8.5	1066.2 ± 9.8	1032 ± 19
Z_91500_6	79.5	30.1	14.97	0.38	1.856	0.023	0.1791	0.0017	0.07313	0.00069	1064.7 ± 8.2	1061.8 ± 9.5	1017 ± 21
Z_91500_7	79.9	30	15.08	0.37	1.809	0.025	0.1784	0.0017	0.07342	0.00046	1048.5 ± 9.4	1058.9 ± 9.3	1024 ± 13
Z_91500_8	79.4	29.6	14.92	0.37	1.857	0.026	0.1794	0.0016	0.07377	0.00052	1064.7 ± 9.3	1064.5 ± 8.7	1044 ± 18
Z_91500_9	80.7	30.5	15.04	0.38	1.846	0.029	0.1789	0.0021	0.07335	0.00062	1064 ± 10	1061 ± 11	1013 ± 21
Z_91500_10	78.9	29.8	14.9	0.38	1.86	0.021	0.1787	0.0014	0.07376	0.00046	1066.2 ± 7.3	1059.9 ± 7.8	1047 ± 18
Z_91500_11	80.3	29.5	15.06	0.37	1.862	0.025	0.18	0.0016	0.07328	0.00053	1067.4 ± 8.9	1067.8 ± 8.6	1023 ± 16
Z_91500_12	82.2	31.4	15.14	0.38	1.859	0.029	0.1782	0.0022	0.0737	0.00049	1068 ± 11	1058 ± 12	1034 ± 15
Z_91500_13	78.2	29.4	14.9	0.37	1.848	0.027	0.1793	0.0017	0.07362	0.00053	1064 ± 10	1063.1 ± 9.4	1036 ± 17
Z_91500_14	80.7	29.9	14.96	0.38	1.869	0.028	0.1816	0.0019	0.07365	0.00048	1070 ± 10	1075 ± 11	1026 ± 15
Z_91500_15	79.7	30	15.04	0.37	1.819	0.026	0.1773	0.0019	0.07353	0.00061	1051.1 ± 9.4	1052 ± 10	1021 ± 20
Z_91500_1	82.2	31.7	16.25	0.38	1.846	0.026	0.1795	0.0018	0.07333	0.00046	1063.6 ± 8.7	1063.8 ± 9.7	1024 ± 13
Z_91500_2	78.1	29	14.29	0.37	1.854	0.023	0.1788	0.0019	0.07369	0.00043	1065 ± 8.2	1060 ± 10	1031 ± 15
Z_91500_3	80	29.8	14.74	0.37	1.848	0.029	0.1792	0.0023	0.07331	0.00049	1063 ± 10	1062 ± 12	1020 ± 16
Z_91500_4	79.8	29.4	15.05	0.36	1.85	0.027	0.1792	0.002	0.07354	0.00048	1064.2 ± 9.7	1062 ± 11	1027 ± 13
Z_91500_5	80.7	29.7	15.12	0.38	1.85	0.021	0.1791	0.0018	0.0739	0.00048	1063.6 ± 7.5	1063 ± 10	1040 ± 14
Z_91500_6	79.7	30.5	14.99	0.37	1.849	0.024	0.1792	0.0018	0.07363	0.00049	1062.1 ± 8.7	1063 ± 10	1030 ± 14
Z_91500_1	79.3	29.6	15.31	0.37	1.864	0.047	0.1796	0.0025	0.0726	0.001	1068 ± 17	1065 ± 14	1002 ± 31
Z_91500_2	79.7	30	14.27	0.36	1.811	0.046	0.1785	0.0024	0.0724	0.00068	1047 ± 16	1059 ± 13	989 ± 22
Z_91500_3	82.5	30.8	15.67	0.38	1.873	0.049	0.1792	0.0028	0.07281	0.00077	1067 ± 17	1062 ± 15	1007 ± 22
Z_91500_4	80	30	15.23	0.37	1.85	0.04	0.1801	0.0024	0.07224	0.00066	1065 ± 14	1067 ± 13	990 ± 19
Z_91500_5	79.9	29.5	14.94	0.36	1.874	0.04	0.1789	0.0023	0.07316	0.00067	1069 ± 14	1062 ± 13	1012 ± 20

ID	U (ppm)	Th (ppm)	Pb (ppm)	Th/U	$^{207}Pb/^{235}U$	2σ	$^{206}Pb/^{238}U$	2σ	$^{207}Pb/^{206}Pb$	2σ	$^{207}Pb/^{235}U$ Age (Ma)	$^{206}Pb/^{238}U$ Age (Ma)	$^{207}Pb/^{206}Pb$ Age (Ma)
Z_91500_6	78.9	30	14.85	0.38	1.836	0.042	0.179	0.0023	0.07236	0.00076	1057 ± 15	1061 ± 13	995 ± 22
Z_91500_7	80.4	30.1	14.96	0.38	1.836	0.045	0.1793	0.0024	0.07234	0.00063	1055 ± 16	1064 ± 13	997 ± 19
Z_91500_8	79.1	30	14.46	0.39	1.853	0.04	0.1787	0.0024	0.07279	0.00065	1064 ± 14	1059 ± 13	1005 ± 18
Z_91500_9	81.3	29.9	15.63	0.37	1.86	0.043	0.1796	0.0025	0.07291	0.00066	1067 ± 15	1066 ± 13	1011 ± 19
Z_91500_10	79.9	29.8	14.68	0.39	1.844	0.039	0.1791	0.0032	0.07081	0.00089	1060 ± 14	1061 ± 17	956 ± 28
Z_91500_11	79.2	30.6	15.02	0.39	1.826	0.049	0.1797	0.0032	0.07099	0.00084	1053 ± 17	1067 ± 18	955 ± 23
Z_91500_12	79.6	29.6	14.82	0.38	1.844	0.042	0.1789	0.0028	0.0721	0.0007	1063 ± 15	1060 ± 15	989 ± 21
Z_91500_13	81	30	15.16	0.38	1.881	0.052	0.1783	0.0032	0.07387	0.00084	1074 ± 18	1057 ± 17	1033 ± 23
Z_91500_14	80.5	30.4	17.3	0.37	2.07	0.14	0.1814	0.0033	0.0736	0.00072	1114 ± 37	1074 ± 18	1031 ± 21
Z_91500_15	78	29.2	14.33	0.36	1.801	0.046	0.1777	0.0027	0.07244	0.00061	1044 ± 17	1054 ± 15	992 ± 19
Z_91500_16	82.1	30.7	17.21	0.37	2.06	0.1	0.1794	0.0029	0.0741	0.0011	1124 ± 32	1063 ± 16	1037 ± 31
Z_91500_17	79.3	30	14.96	0.38	1.854	0.045	0.1802	0.003	0.07277	0.00071	1061 ± 16	1067 ± 17	1003 ± 22
Z_91500_18	80.3	30	14.94	0.37	1.814	0.047	0.1785	0.0026	0.07239	0.00065	1046 ± 17	1058 ± 14	1000 ± 20
Z_91500_19	79.3	29.9	14.98	0.37	1.857	0.049	0.1798	0.0031	0.07229	0.00082	1066 ± 17	1065 ± 17	989 ± 23
Z_91500_20	80.3	30.3	15.12	0.38	1.873	0.045	0.1787	0.003	0.07351	0.00063	1074 ± 16	1063 ± 17	1025 ± 17
Z_91500_21	79.4	29.2	14.78	0.34	1.84	0.052	0.1789	0.0032	0.07224	0.00075	1060 ± 19	1060 ± 18	992 ± 22
Z_91500_22	80.1	30.3	14.93	0.39	1.822	0.042	0.1802	0.0037	0.07164	0.00067	1053 ± 15	1069 ± 20	977 ± 20
Z_91500_23	80.8	30.5	15.22	0.36	1.866	0.043	0.1791	0.0032	0.073	0.0007	1070 ± 15	1063 ± 17	1011 ± 19
Z_91500_24	79.2	28.9	14.94	0.38	1.86	0.055	0.1787	0.0035	0.07242	0.00067	1066 ± 20	1059 ± 19	994 ± 19
Z_91500_25	80.1	30.9	15	0.39	1.847	0.052	0.1797	0.0037	0.0722	0.00074	1060 ± 18	1061 ± 19	987 ± 21
Z_91500_26	80	29.7	14.98	0.36	1.85	0.041	0.179	0.0028	0.07247	0.00078	1062 ± 14	1061 ± 15	990 ± 25
							Plešovice						
Z_Plesovice_1	1076	124.7	17.87	0.11	0.3926	0.0044	0.05376	0.00045	0.05034	0.00081	336.6 ± 3.3	337.5 ± 2.8	204 ± 38
Z_Plesovice_2	1056	104	15.62	0.10	0.391	0.0065	0.05373	0.00067	0.0503	0.0011	335 ± 4.7	337.4 ± 4.1	204 ± 54
Z_Plesovice_3	1037	103.9	15.63	0.10	0.3938	0.0055	0.05367	0.00071	0.0492	0.0011	337.1 ± 4	337 ± 4.3	149 ± 52
Z_Plesovice_4	977	104.7	15.73	0.10	0.395	0.004	0.05371	0.00035	0.04966	0.00086	338 ± 2.9	337.5 ± 2.1	176 ± 41
Z_Plesovice_1	821	76	12.26	0.09	0.3937	0.0059	0.05369	0.00047	0.0501	0.001	337 ± 4.3	337.1 ± 2.9	195 ± 49
Z_Plesovice_2	520.3	68.3	11.23	0.13	0.3939	0.0076	0.05385	0.00044	0.05196	0.00051	337.2 ± 5.6	338.1 ± 2.7	283 ± 23
Z_Plesovice_3	761	91	14.87	0.12	0.4005	0.0042	0.05376	0.00029	0.05017	0.00084	341.9 ± 3	337.5 ± 1.8	196 ± 39
Z_Plesovice_4	591.6	53.2	10.83	0.09	0.4	0.014	0.05424	0.00088	0.049	0.0028	341.7 ± 9.9	340.5 ± 5.4	140 ± 130
Z_Plesovice_5	2255	227.3	36.3	0.10	0.3922	0.0059	0.05359	0.00055	0.0493	0.0018	336 ± 4.3	336.5 ± 3.4	153 ± 85
Z_Plesovice_6	988	138.1	20.98	0.14	0.3997	0.0038	0.05375	0.0003	0.05017	0.00074	342.3 ± 3.3	337.5 ± 1.9	195 ± 35
Z_Plesovice_7	1448	140.7	22.78	0.10	0.4002	0.0034	0.05368	0.00034	0.05042	0.00073	341.8 ± 2.5	337 ± 2.1	206 ± 34
Z_Plesovice_8	835	91	16.48	0.11	0.3927	0.0082	0.05369	0.0007	0.0496	0.0013	336.2 ± 6	337.1 ± 4.3	169 ± 63
Z_Plesovice_1	801	84.6	14.96	0.10	0.3921	0.005	0.05371	0.00068	0.0504	0.0015	335.9 ± 3.6	337.2 ± 4.2	205 ± 70
Z_Plesovice_2	696	66.6	11.31	0.10	0.3941	0.0053	0.05367	0.00042	0.05	0.001	337.3 ± 3.9	337 ± 2.6	189 ± 49

ID	U (ppm)	Th (ppm)	Pb (ppm)	Th/U	$^{207}Pb/^{235}U$	2σ	$^{206}Pb/^{238}U$	2σ	$^{207}Pb/^{206}Pb$	2σ	$^{207}Pb/^{235}U$ Age (Ma)	$^{206}Pb/^{238}U$ Age (Ma)	$^{207}Pb/^{206}Pb$ Age (Ma)
Z_Plesovice_1	607	75.8	12.99	0.12	0.3932	0.0092	0.05383	0.00052	0.04924	0.00095	336.4 ± 6.7	338 ± 3.2	159 ± 46
Z_Plesovice_2	642	74.9	12.09	0.12	0.398	0.0053	0.05371	0.00033	0.04901	0.00057	340 ± 3.9	337.3 ± 2	142 ± 27
Z_Plesovice_3	579	72.8	11.38	0.13	0.3945	0.0064	0.05325	0.00036	0.04887	0.0007	337.5 ± 4.7	334.5 ± 2.2	139 ± 34
Z_Plesovice_4	647	79.5	12.44	0.13	0.3889	0.0065	0.05331	0.00043	0.04939	0.00061	333.3 ± 4.8	334.8 ± 2.6	160 ± 29
Z_Plesovice_5	780	94.3	14.7	0.13	0.3992	0.0053	0.05365	0.00034	0.04965	0.00062	340.9 ± 3.8	336.9 ± 2.1	173 ± 29
Z_Plesovice_6	766	95.3	15.34	0.13	0.4009	0.0058	0.0537	0.00033	0.04951	0.00065	342.1 ± 4.2	337.2 ± 2	166 ± 31
Z_Plesovice_7	1039	105.6	17.14	0.10	0.3924	0.0039	0.05377	0.0003	0.05022	0.00058	336 ± 2.9	337.6 ± 1.9	199 ± 27
Z_Plesovice_8	686	89.2	14.1	0.13	0.3899	0.005	0.05382	0.00029	0.04902	0.00054	334.1 ± 3.7	337.9 ± 1.8	143 ± 26
Z_Plesovice_9	669	83.4	13.63	0.13	0.3848	0.0076	0.05379	0.00043	0.04985	0.00075	330.4 ± 5.6	337.8 ± 2.6	183 ± 36
Z_Plesovice_10	631	80.7	13.06	0.13	0.3939	0.0048	0.05377	0.00033	0.04916	0.00061	338 ± 3.6	337.6 ± 2	149 ± 29
Z_Plesovice_11	862	105.8	15.29	0.12	0.3919	0.0062	0.05378	0.00031	0.05053	0.00076	335.6 ± 4.6	337.7 ± 1.9	214 ± 36
Z_Plesovice_12	867	99.9	15.52	0.12	0.3958	0.0081	0.05354	0.00047	0.04948	0.00089	338.4 ± 5.9	336.2 ± 2.9	171 ± 43
Z_Plesovice_13	791	97.6	15.05	0.13	0.4024	0.0084	0.05382	0.00041	0.0488	0.0011	343.2 ± 6	337.9 ± 2.5	133 ± 53